Title
The Relationship Between Diamondiferous Kimberlite and Peridotite from the Cullinan Pipe, South Africa

Permalink
https://escholarship.org/uc/item/96x7z5ts

Author
Linzmeyer, Taryn

Publication Date
2021

Peer reviewed|Thesis/dissertation

UNIVERSITY OF CALIFORNIA SAN DIEGO

The Relationship Between Diamondiferous Kimberlite and Peridotite from the Cullinan Pipe,

South Africa

A thesis submitted in partial satisfaction of the requirements

for the degree Master of Science

in

Earth Sciences

by

Taryn Linzmeyer

Committee in charge:

James M.D. Day, Chair
Raquel Alonso-Perez
Geoff Cook
Jeff Gee

2021

The thesis of Taryn Linzmeyer is approved,
and it is acceptable in quality and form for publication on microfilm and
electronically.

University of California San Diego

2021

TABLE OF CONTENTS

LIST OF FIGURES

LIST OF TABLES

ACKNOWLEDGEMENTS

ABSTRACT OF THE THESIS

The Relationship Between Diamondiferous Kimberlite and Peridotite from the Cullinan Pipe,

South Africa

by

Taryn Linzmeyer

Master of Science in Earth Sciences

University of California San Diego, 2021

Professor James M.D. Day, Chair

The ~1.15 billion-year-old (Ga) Cullinan kimberlite pipe is composed of several lithologically

distinct kimberlite facies (Grey, Brown, Pale Piebald, Dark Piebald, Black Coherent, Blue/Brown

Transitional, and Fawn). In this study, I report bulk rock Os isotope data for these facies, as well as a suite

of peridotites, pyroxenites and an amphibolite. Measured $^{187}Os/^{188}Os$ abundances of the different

kimberlite facies range from 0.1223 to 0.1672, and peridotites range from 0.1096 to 0.1244. The pyroxenites have radiogenic measured $^{187}Os/^{188}Os$ ratios of 0.9376 and 0.1796 and the amphibolite 2.861. These data are complemented by bulk rock highly siderophile element abundances (HSE: Re, Pd, Pt, Ru, Ir, Os) and major element and trace element abundances. Kimberlite melt infiltration in the peridotite xenoliths is evident in the presence of melt veins, and enriched rare earth element and Re abundances. Negative La/Yb versus Re/Os correlations indicate that peridotites may have experienced metasomatism prior to kimberlite assimilation. The kimberlites and peridotites plot on a $^{187}Re/^{188}Os$ versus $^{187}Os/^{188}Os$ mixing line (R^2=0.924) indicating that the range in measured $^{187}Os/^{188}Os$ for the kimberlites reflects variable assimilation of cratonic lithospheric mantle (CLM), with the Brown kimberlite being the least affected by this process. The peridotites display a trend between higher Re concentration and lower T_{RD} (Time of Rhenium Depletion) eruption ages. This suggests T_{RD} eruption ages for some Proterozoic age samples are erroneously young, due to additional Re added prior to kimberlite entrainment, possibly linked to the Bushveld Igneous Event.

1. Introduction

Kimberlites are ultramafic, silica-undersaturated, CO_2 and H_2O rich rocks derived from melts generated at depths of at least 150 kilometers. Kimberlites are located on continental cratons worldwide and provide a unique probe of the mantle. They are deeply derived magmas that are unaffected by shallower melting processes, making kimberlites important volcanic rocks for understanding deep Earth processes.

Kimberlites are scientifically important due to their deep origins, but they also hold economic value through their mineral cargoes. As kimberlite magmas rise, they entrain mantle materials which can occasionally contain diamonds. As a result, 70% of natural diamond production by value comes from kimberlites, as well as a majority of the gem-quality diamonds commercially mined (Giuliani and Pearson 2019). One thousand kimberlite deposits have diamonds of economic interest, and 61 are currently or formerly functioning diamond mines (Kjarsgaard et al. 2019).

One of the most famous and scientifically intriguing of these pipes is Cullinan kimberlite pipe, formerly named the Premier kimberlite. Cullinan is located in the Archean Kaapvaal craton of South Africa, 37 km northeast of Pretoria (**Figure 1**). At 32 hectares in size, it is the largest kimberlite pipe by area in South Africa (Bartlett 1994). The pipe was initially discovered along with a cluster of ten other kimberlite pipes by prospectors of heavy minerals who found diamonds in the nearby Pienaars river (Field et al. 2008). Cullinan opened as a mine in 1903 and has functioned between the years 1903 to 1915, 1916 to 1932, and 1950 to present (Field et al. 2008). In 1905, a 3106 ct type IIa diamond was found, named the Cullinan Diamond. To this

day, it remains the largest gem-quality diamond ever discovered and cut fractions of it reside in the crown jewels of Her Majesty the Queen of the United Kingdom.

Cullinan intrudes through the southern end of the ~2.054 Ga Bushveld Complex, the world's largest layered intrusion (Scoates and Friedman 2008). This massive magmatic event had an estimated volume of 1×10^6 km^3, emplaced by successive basaltic magma injections over the course of >75,000 years (Cawthorne and Walraven 1998). Evidence for disturbance of the lithospheric mantle below Cullinan due to the Bushveld event has been well documented. This includes negative P-wave anomalies recorded through seismic imaging (James et al. 2001, Shirey et al. 2002, Fouch 2004).

Cullinan is most notable due to producing valuable type IIa diamonds, and also for being the world's major source of blue type IIb diamonds. Type II diamonds are extremely rare, making up <2% of gem quality diamonds mined (Gaillou et al. 2012). They are defined as having nitrogen levels below detection limit of infrared spectrometry (FTIR), which can vary depending on analytical sensitivity, but is most often defined as <10-20 ppm (Korolev et al. 2018). Type IIb diamonds are Type II diamonds which also contain trace compositions of boron, which can give them a blue color. This is one of the rarest and most valuable diamond hues; for example, at a 2009 auction a Type IIb reached $1.3 M per carat (Gaillou et al. 2012).
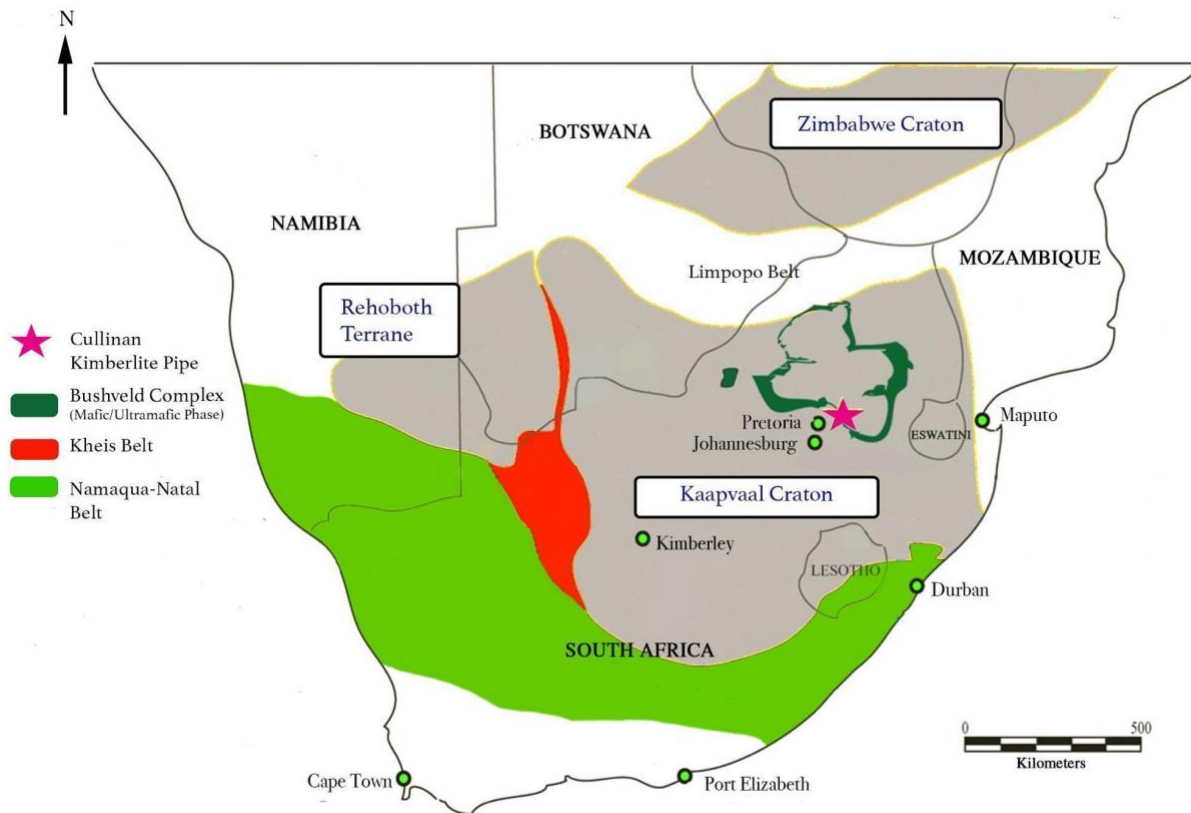
Figure 1: Simplified map of Southern Africa adapted from Tappe et al. 2020. Cullinan is denoted by a pink star, intruding through the southern Bushveld Complex. The Kaapvaal and Zimbabwe Cratons are Archean in age, and the Rehoboth Terrane is Proterozoic in age. The Kaapvaal Craton, Zimbabwe Craton, and Rehoboth Terrane all contain kimberlites, though the kimberlites in the Rehoboth Terrane do not contain diamonds. It also has a slightly lower lithospheric thickness (180 ± 20 km, while the Kaapvaal Craton is about 220 ± 20 km thick in the eastern part) (Muller et al. 2009).

Cullinan is also notable not just for its size and diamond population, but also for being one of the oldest kimberlites in the world. Wu et al. (2013) dated the Brown and Black kimberlite units at 1150 ± 16 Ma, 1151 ± 9 Ma respectively using U-Pb in perovskite. Tappe et al. (2018b) dated the Grey kimberlite unit at 1155.2 ± 5.3 Ma. Previously, Cullinan has also been dated at 1202 ± 72 Ma by Kramers and Smith (1983). Despite discrepancies in attempts to date the Cullinan kimberlite pipe, it is undeniably the oldest of the world's seven largest diamond

mines, with the second oldest being the 528 Ma Venetia mine (Heaman et al. 2019). Eighty-seven percent of kimberlite magmatism has occurred over the course of four-time intervals which correspond with supercontinental breakup and assembly. Significant changes in plate motion are thought to provide pathways for melts to reach the surface. These intervals are 1200 to 1075 Ma (9.4 %), 600 to 500 Ma (7.4%), 400 to 350 Ma (5%), and 250 to 50 Ma (62.5%) (Tappe et al. 2018, Jelsma et al. 2009). Cullinan falls into the oldest known time interval of kimberlite magmatism, which corresponds to the assembly of Rodinia (Tappe et al. 2018, Jelsma et al. 2009).

Despite Cullinan's historical and economic importance, limited geochemical research has been conducted on the specific kimberlite facies of the pipe. The pipe itself is a diatreme composed of multiple kimberlite units with textural and mineralogical variation. These facies can be broken down by emplacement type into massive volcaniclastic kimberlites (MVKs) and hypabyssal kimberlites (**Figure 2**). Though the volcaniclastic kimberlites have historically been referred to as tuffistic kimberlite breccias (TKBs), they will in this thesis be referred to as MVKs, in accordance with terminology established in Sparks et al. (2006). This broader terminology is preferable, as the volcaniclastic kimberlites may not technically fit into the classification of 'breccia' if they do not have clasts above 6.4 cm, and the term 'tuffistic' implies specific genetic origins (Sparks et al. 2006). The main MVK units are the Grey and Brown kimberlites. The hypabyssal units include the Pale Piebald, Dark Piebald, and Black Coherent kimberlites, which make up a 'plug' in the center of the diatreme. The pipe also includes carbonatized dikes and a large gabbro sill, the latter of which is contemporary with the 1112-1108 Ma Umkondo Igneous Event (De Kock et al. 2014)

This study provides the first measured Re-Os isotopic abundances for the Cullinan kimberlite facies and the first highly siderophile element abundances (HSE: Os, Ir, Ru, Pt, Pd, Re) for most of the kimberlite facies (Tappe et al. 2020 published HSE abundances of one Piebald and one Grey sample). Rhenium/Osmium and the HSE are powerful tracers in processes affecting kimberlites and mantle xenoliths entrained in them due to differences in incompatibility. As Os is a compatible element, there is a larger Os concentration in peridotites than kimberlites, meaning that peridotite would have a much larger influence on Os isotope systematics of kimberlite than kimberlite would on peridotite.

A few research questions are addressed in this study. Firstly, what are the chemical differences of the kimberlite facies within Cullinan kimberlite pipe which can be constrained through Re-Os isotope systematics? Next, can studying the different kimberlite facies add insights about diamond grade distribution between the different units? Lastly, how old is the lithosphere beneath Cullinan? How do ages of peridotites calculated from Re-Os isotopic abundances reflect processes in the region since the Archean?

Figure 2: Simplified cross-sectional map of Cullinan kimberlite pipe, edited from a map obtained through personal correspondence with the mine geologists. Levels where samples were collected are indicated in red, and lists of samples collected from each level are listed in Table 1.

6

2. Samples

A suite of thirty-five whole-rock samples were analyzed for major- and trace-element abundances. A summary of samples is given in **Tables 1 and 2.** Kimberlite samples selected for Re-Os isotope analysis and highly siderophile element (HSE) abundances are described here in more detail as determined by microscopic observations and desktop SEM analysis.

Table 1: Kimberlite and calcite dike rock types, emplacement styles, sample identifications, image numbers, levels found in mine, and samples selected for Re-Os isotopic analysis. Kimberlite type classifications are from Bartlett 1994. The term MVK was first defined in Sparks et al. 2006.

Rock Type	MVK or Hypabyssal	Sample ID	Figure # (Appendix)	Level in Mine	Sample analyzed for Re-Os and HSEs
Grey Kimberlite (Type 1)	MVK	C2106, C2108, C2112, C2114	S6, S7, S9, S11	839 L, 763L, 732 L, 732 L	C2114
Brown Kimberlite (Type 2)	MVK	C2101, C2111	S1, S8	824 L +45, 763 L	C2111
Pale Piebald Kimberlite (Type 3A)	Hypabyssal	C2104	S4	839 L	C2104
Dark Piebald Kimberlite (Type 3B)	Hypabyssal	C2103	S3	839 L	C2103
Black Coherent Kimberlite (Type 3C)	Hypabyssal	C2102	S2	839 L	C2102
Blue/Brown Transitional Kimberlite	MVK	C2105	S5	839 L	C2105
Fawn Kimberlite	MVK	C2113	S10	732 L	C2113
C2130 and C2133	N/A	C2130, C2133	S25, S28	N/A	C2133
Calcite Dikes	N/A	C2109, C2110	S30, N/A	763 L, 763 L	N/A
895RAW	N/A	895RAW	S14	839L	N/A

2.1 Grey Kimberlite

Sample C2114 is a volcaniclastic kimberlite with a grey matrix. Magnesium ilmenite, zinc sulfide and chromite are present, as well as opaque oxide mineral phases in the matrix which have unknown composition. Olivine grains are very fractured, and perovskite is widespread.

2.2 Brown Kimberlite

Sample C2111 is an MVK with a brown matrix which is altered to clay. Minerals present include olivine, diopside, apatite and abundant Mg-ilmenite. <2mm long olivine grains are altered to a dark color and display reaction rims. Large, fractured xenoliths are included in the kimberlite, and one large xenolith (8.33 mm in length) has been altered, largely to calcite.

2.3 Pale Piebald Kimberlite

Sample C2104 exhibits an inequigranular texture typical of macrocrystal hypabyssal kimberlites (Mitchell 1986). The matrix is a black color, in many places altered to clay. It has abundant phlogopite microcrysts and includes perovskite, serpentine, and Mg-ilmenite. Many large olivine macrocrysts are between 1.1 and 3.8 mm in length and are heavily altered to serpentine. One large 20.8 mm long xenolith is entrained in this kimberlite, though it is difficult to determine the mineral components of this xenolith due to its pervasive alteration.

2.4 Dark Piebald Kimberlite

Sample C2103 is a hypabyssal kimberlite sample with a brown-orange matrix which includes abundant phlogopite microcrysts and occasional perovskite. Macrocrysts include Mg-ilmenite and olivine. Many olivine macrocrysts are between lengths of 1.2 to 1.7 mm and some have thick, dark alteration rims. Some very large, rounded, black clasts are altered beyond recognition (ranging from 6 mm to 7.9 mm in length). Nickel-sulfides are also present in the matrix.

2.5 Black Coherent Kimberlite

Sample C2102 is a hypabyssal kimberlite exhibiting a classic inequigranular texture. The matrix is a light brown color with minerals including phlogopite microcrystal needles, calcium carbonate, perovskite, apatite, and many small opaques. Massive Mg-ilmenite macrocrysts are also present, and euhedral olivine grains, many of which display zonation. Some subhedral olivine macrocrysts reach 7.3 mm in length.

2.6 Blue/Brown Transitional Kimberlite

Sample C2105 has a volcaniclastic texture. Large angular to subrounded olivine macrocrysts are altered by serpentine, some as large as 3.7 mm in length. Nickel-iron sulfides are found in some olivine grains. The matrix is a dark brown color and includes clinopyroxenes, perovskite, and olivine with alteration rims. Other minerals in the matrix include Mg-ilmenites and zircons. A few angular crustal xenoliths are visible, as well as a round mantle xenolith 4.8 mm in diameter.

2.7 Fawn Kimberlite

Sample C2113 is a kimberlite with visual similarity to the blue/brown transitional kimberlite. This sample has a volcaniclastic texture and includes large olivine and diopside macrocrysts. Its matrix is a dark brown color and contains perovskite and abundant opaques as well as subrounded olivine. Nickel sulfides are plentiful in the macrocrysts.

2.8 C2130 and C2133

These kimberlite samples were collected by mine workers who interpreted them to be xenoliths, therefore their origin in the pipe and unit are unknown. Due to this uncertainty, they will neither be called hypabyssal nor MVK. However, both have an inequigranular texture similar to hypabyssal kimberlites. C2133 contains large olivine macrocrysts and a large garnet with a dark alteration rim (likely kelyphite). The matrix is a light brown-tan color and contains several ilmenite macrocrysts. Minerals in C2130 include olivine macrocrysts of varying size. Serpentinization is apparent. Ilmenite grains are present in the matrix, as well as other small unidentifiable opaque minerals.

Table 2: Mantle xenolith types, sample identifications numbers, image number in appendix, and samples analyzed for Re-Os isotopes and HSE abundances.

Xenolith Type	Sample ID	Thin Section Image # (Appendix)	Samples Analyzed for Re-Os and HSEs
Harzburgite	C2125, C2127, C2128, C2129	20, 22, 23, 24	C2127, C2128, C2129
Harzburgite with Phlogopite Veins	C2116	32	C2116
Garnet Harzburgite	C2131, C2132, C2134	26, 27, 29	C2131, C2132, C2134
Lherzolite	C2117, C2118, C2119	12, 13, 15	C2117, C2118, C2119
Garnet Lherzolite	C2121, C2123, C2124, FRB 1350 (Garnet Spinel Lherzolite)	16, 18, 19, N/A	C2121, C2124, FRB 1350
Garnet Lherzolite or Garnet Harzburgite	FRB 921	N/A	FRB 921
Pyroxenite	C2122, C2126	17, 21	C2122, C2126
Amphibolite	C2115	31	C2115

2.9 Harzburgites

All four Harzburgite samples (C2125, C2127, C2128, C2129) have been altered and so now contain significant regions of serpentinized material. C2128 has dark melt veins, likely resulting from impregnation by the kimberlite melt (**Figure 3**). Modal abundances estimate this melt impregnation constitutes 15% of the sample. Relict olivine and orthopyroxene are preserved, and spinel is present interstitial to the silicate phases.
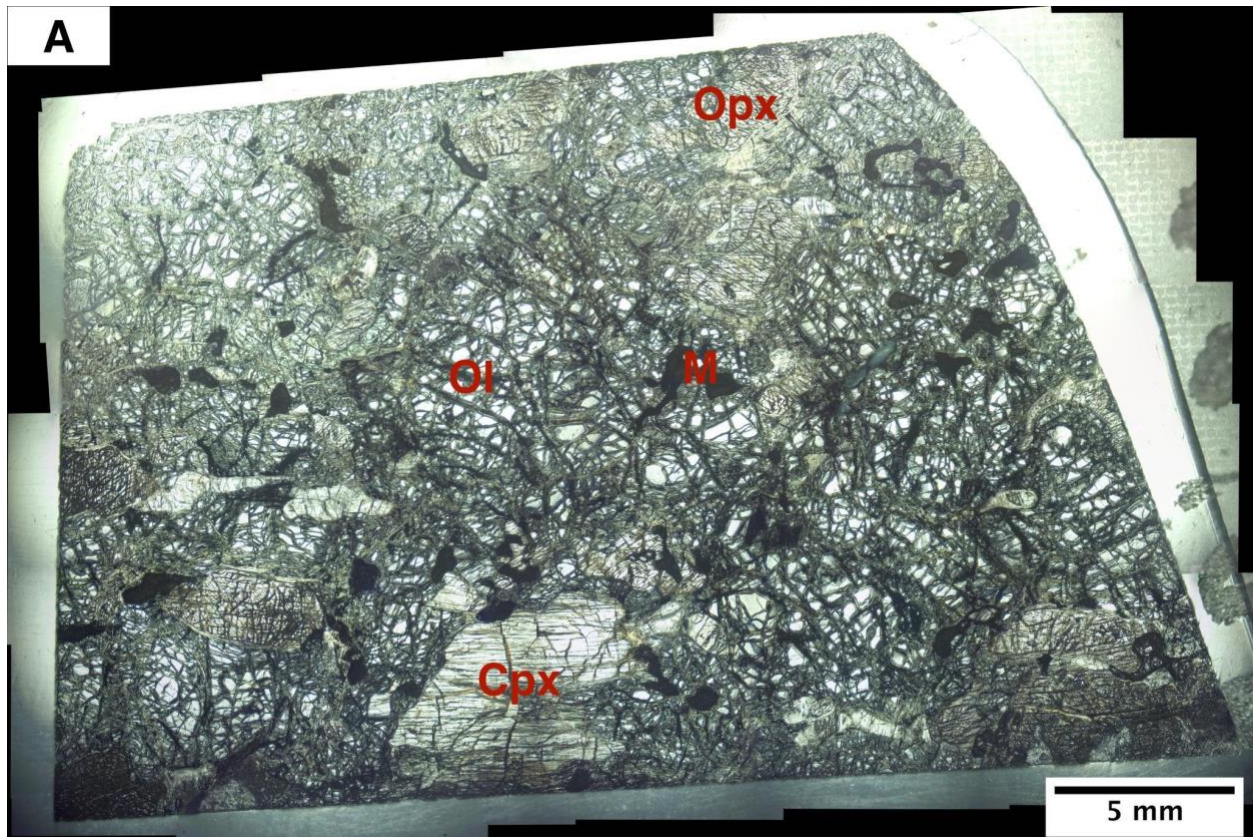
Figure 3: Harzburgite sample C2128 imaged in plane polarized light. Scale bar is 5 mm. Opx=orthopyroxene, Ol=olivine, M=melt impregnation, Cpx=clinopyroxene

2.10 Lherzolites

C2117 is a sheared lherzolite. C2118 and C2119 display serpentinization of olivine, but are otherwise minimally visually altered. C2118 also has several visible spinel grains.

2.11 Garnet Harzburgites and Lherzolites

C2131 has some very large olivine crystals, the largest of which is about 9.6 mm in length. Some black alteration rims are seen around the garnets (possibly kelyphite) and opaque minerals are present. C2132 has an inequigranular texture, with most of the olivine and pyroxene grains <0.5mm in length. Serpentinization is apparent and the garnets have dark alteration rims.

13

C2134 has many large opaque grains, and similarly to C2132, has an inequigranular texture, with many minerals between 0.5 and 1 mm in width.

C2121 has the most minimal alteration of the garnet lherzolites, apart from dark alteration rims on the garnets, which is possibly kelyphite. C2123 also has dark alteration rims, but they are much thicker. Many grains are sheared to small sizes. Some yellow and black minerals are present, which may be phlogopite.

C2124 is very altered and will be referred to as an altered garnet lherzolite. There are plentiful dark oxides, possibly from the spinel group, as well as phlogopite.

FRB 921 is described as a low-temperature garnet lherzolite or harzburgite in Pearson et al. 1995. FRB 1350 is described as a garnet-spinel lherzolite in Pearson and Nowell 2002, where modes are given. The calculated whole-rock trace element composition based on the modes is lower than the measured whole-rock values for almost all of the incompatible trace elements. A likely explanation for this would be the addition of incompatible trace elements by kimberlite melt infiltration. This sample also includes graphite flakes, indicating a relatively shallow origin, and is described in more detail in Pearson et al. 1994.

2.12 Pyroxenites and Amphibolite

The three pyroxenite samples vary greatly visually. C2122 has abundant garnet, and is severely impregnated with melt veins. C2126 has very fine-grained laths, and plentiful opaques. The amphibolite C2115 has abundant amphibole grains, some of which are visibly hexagonal, and many small opaques.

3. Analytical Methods

3.1 Sample Selection and Preparation

At Cullinan Diamond Mine, eighteen xenoliths were sub-sampled out of several hundred (**Figure 4**). Thirteen kimberlites and two calcite dikes were also collected, and thin sections were made. Initially, samples were sent to Harvard University, where the main masses were curated. There, samples were sawed and billeted. Subsequently, at Scripps Institution of Oceanography, the sawn blocks were further subdivided, sawed and cleaned, crushed in an alumina plate jaw crusher, and finely powdered in a SPEX SamplePrep alumina ShatterBox.

Figure 4: Image of mantle xenolith piles at Cullinan Diamond mine. Xenoliths were washed and crudely separated by peridotite type and subsampled out of several hundred.

3.2 Whole-Rock Major Element Abundances

Major element abundances, loss on ignition (LOI), and select trace elements (Rb, Sr, Zr, V, Cr, Ba) were measured by X-Ray fluorescence (XRF) at Franklin and Marshall College on a *PW 2404 Panalytical XRF* vacuum spectrometer using methods previously described in Boyd and Mertzman (1987). LOI was determined by heating a precisely weighed sample of powder (~1g) at 950 °C for 1.5 hours and determining the change in mass before and after. Standard lithium tetraborate fusion techniques were performed with a 0.4: 3.6 ratio of powder: lithium tetraborate. Ferrous iron concentration was determined by potassium dichromate titration. Precision and accuracy are estimated by repeat analyses of standards. Long term reproducibility (in wt % and 2σ absolute standard deviation, n=13) is ±0.13 for SiO_2, ±0.01 for TiO_2, ±0.09 for Al_2O_3, ±0.63 for FeO, ±0.47 for Fe_2O_3, ±0.10 for Fe_2O_3T, ±0.01 for MnO, ±0.04 for MgO, ±0.07 for CaO, ±0.03 for Na_2O, ±0.01 for K_2O, and $\pm<0.01$ for P_2O_5. Accuracy for the average of 13 runs of BHVO-2 relative to USGS values have relative uncertainties better than 0.2% for SiO_2 and TiO_2, <1% for Al_2O_3, MgO, Fe_2O_3T, CaO, Na_2O, P_2O_5, and <3% for K_2O (Day et al. 2017).

3.3 Whole-Rock Trace Element Abundances

Trace element analyses were performed at the Scripps Isotope Geochemistry Lab (*SIGL*) using methods previously described in Day et al. 2017. One hundred milligrams of powder was precisely weighed along with rock standards (BHVO-2, BCR-2, BIR-1, HARZ-01) and total procedural blanks. Powders were digested in a 1:4 mixture of Teflon-distilled HNO_3-HF for 72 hours at 150°C on a hotplate. Dry down and HNO_3 dry-down steps were repeated until solutions

were clear and all fluoride complexes were destroyed. Clear solutions were diluted by a factor of 5000 in 2% HNO_3 and doped with a 1 ppb In solution to monitor instrument drift. Solutions were then measured on a *Thermo Scientific* ICAP Qc ICP-MS. Trace element reproducibility of the standard BHVO-2 (n=8) had an RSD of 6% or better, except for Mo (11%), Te (7%), and Cs (16%).

3.4 Osmium Isotope Analysis and Highly Siderophile Element Abundances

Eight kimberlite and sixteen mantle xenolith samples were selected for osmium isotope and highly siderophile element (HSE) abundance analysis. One sample of each kimberlite type is present in the new dataset (Black Coherent, Dark Piebald, Pale Piebald, Brown, Fawn, Grey, and Blue/Brown Transitional and C2133).

Osmium isotope and highly siderophile element abundance analysis were determined at the *SIGL*. Precisely weighed homogenized powders (0.8 g for xenoliths and C2133, and 0.5 g for kimberlites) were loaded into borosilicate Carius tubes. Appropriate amounts of isotopically enriched multielement spikes were precisely added (^{99}Ru, ^{106}Pd, ^{185}Re, ^{190}Os, ^{191}Ir, ^{194}Pt) along with a 1:2 mixture of Teflon-distilled HCl:HNO_3, purged of Os by treatment with H_2O_2.

Samples were digested in an oven for 72 hours at 270 °C. After digestion, Osmium was triple extracted into CCl_4 and back extracted using HBr (Cohen and Waters 1996) before purification using micro-distillation (Birck et al. 1997). Osmium isotopes were measured using a *Thermo Scientific* Triton thermal ionization mass spectrometer (TIMS). The HSE were extracted from residual CCl_4 solution using standard anion exchange techniques (Day et al. 2016) and measured on a *Thermo Scientific* ICAP Qc ICP-MS.

^{187}Os/^{188}Os ratios were measured in negative ion mode on the Triton at the *SIGL*. The total procedural blanks analyzed (n=2) had ^{187}Os/^{188}Os = 0.151±0.006. Offline Os corrections were done using a ^{190}Os spike subtraction, a blank subtraction, an oxide correction, and a fractionation correction using ^{192}Os/^{188}Os = 3.08271. Rhenium, Pd, Pt, Ru, and Ir were corrected for mass fractionation in the instrument over the course of the run using a natural standard solution mixture with 0.5 ppb of all elements of interest relative to the natural isotopic ratio of the element. All values are blank corrected. Blank HSE values in picograms are 22 to 56 [Re], 8 to 99 [Pd], 12 to 252 [Pt], 146 to 423 [Ru], 0 to 3 [Ir], and 3 [Os]. Blank percentages ranged from <0.5%, to high values in Re and Ru, reaching up to 87 and 91% respectively.

4. Results

4.1 Kimberlite Whole-Rock Major- and Trace Element Abundances

Major element and trace element data are reported in **Table 3** and **Table 4**. The kimberlites are low in Al_2O_3 (2.65 to 5.35 wt. %) and Na_2O (0.10 to 2.10 wt. %) and have a wide variation in SiO_2 content (37.5 to 55.3 wt. %). K_2O ranges from 0.36 to 1.73 wt. % except for C2103, which has much higher values (3.9 wt. %). MgO spans from 21.8 to 34.2 wt. %. Loss on ignition (LOI) ranges from 7 to 13.4%.

Major element variations are apparent between the hypabyssal kimberlites and MVKs (**Figure 5**). MVK Na_2O values for this sample set range from 0.78 to 1.58 wt. %, while the hypabyssal kimberlites have significantly lower values (0.1 to 0.27 wt. %). MVKs also have higher SiO_2 values (47.4 to 55.3) than hypabyssal kimberlites (37.5 to 45.0). CaO values for

MVKs range from 3.13 to 8.38 wt. %, while C2102 (Black Coherent) and C2104 (Pale Piebald) have values of 13.2 and 13.4 wt. % respectively.

C2130 and C2133, originally considered to be xenoliths, have similar Na_2O values to the hypabyssal kimberlites (0.31 and 0.19 wt. % respectively) but are lower than them in CaO (3.10 and 5.27 wt. % respectively). They are also enriched in MnO (0.28 and 0.27 wt. % respectively) whereas the other kimberlites range from 0.10-0.18 wt. %.
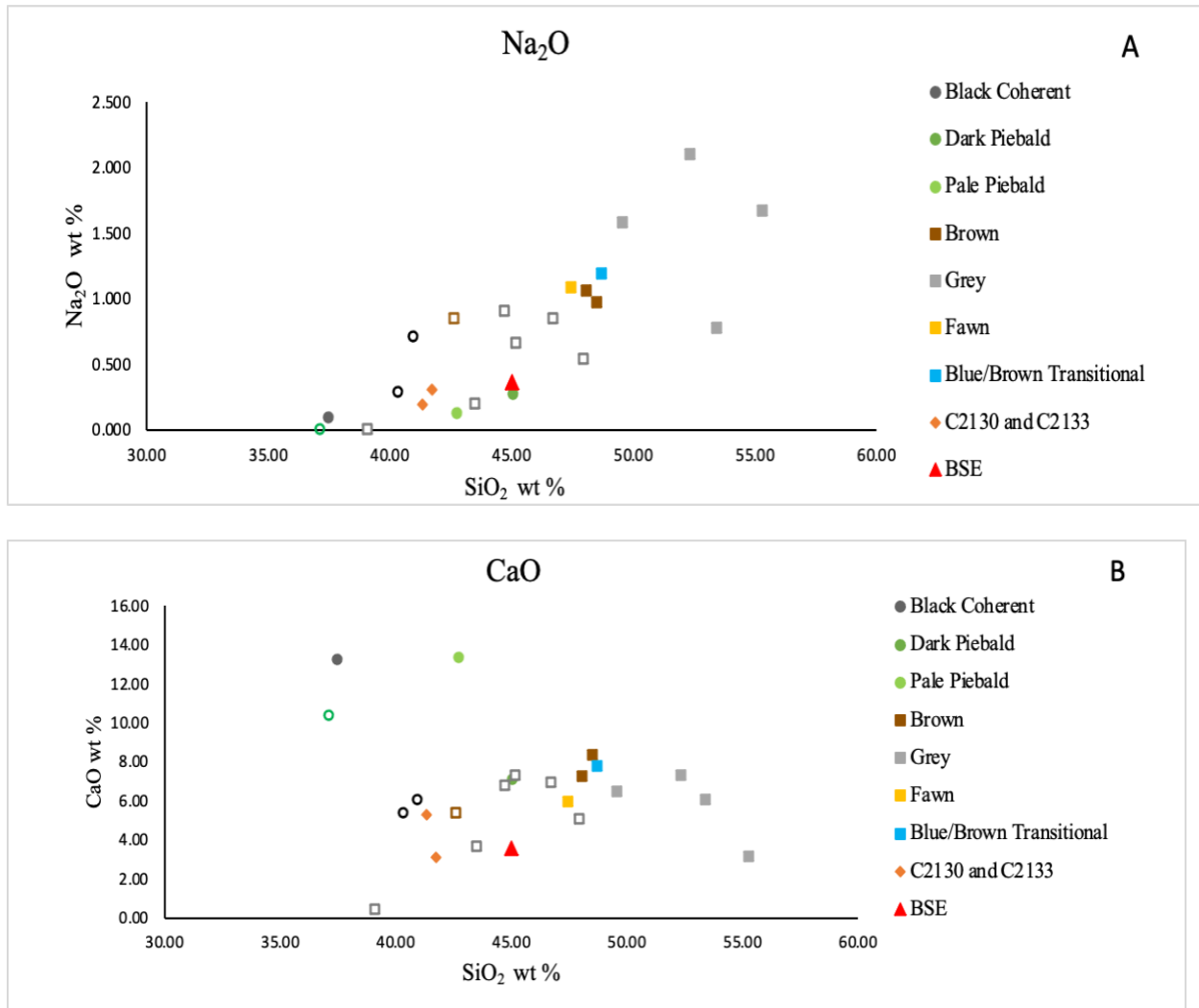
Figure 5: Na$_2$O versus SiO$_2$ (a) and CaO versus SiO$_2$ (b) Harker diagrams. Hypabyssal kimberlites are denoted by circles, MVKs by squares, and C2130 and C2133 by diamonds. Filled-in symbols are from this study, and outlined symbols are previously published data from Robinson 1975, Wu et al. 2013, and Dongre and Tappe 2019. The previously published Piebald sample is from Dongre and Tappe 2019 and does not specify if it is from the Pale Piebald or Dark Piebald unit. Bulk Silicate Earth values are from McDonough and Sun 1995.

Trace element abundances determined by ICP-MS range between <10 × Primitive mantle (PM) values to >500 × PM values (**Figure 6a**). The samples (**Figure 6b**) are enriched in the light rare earth elements (LREE) over heavy rare earth elements (HREE) with La/Yb values ranging from 28.2 to 122 and Sm/Lu ranging from 22 to 98. C2133, C2104 (Pale Piebald) and C2130 have the steepest La/Yb slopes, with values of 122, 106, and 104 respectively. C2106 (Grey), C2112 (Grey), and C2101 (Brown) have the three lowest La/Yb slopes with values of 28, 33, and 41 respectively.

Variations occur in the fluid mobile large ion lithophile elements (LILE), particularly in Ba, Rb, and Sr. Barium enrichments are highest in the hypabyssal kimberlite samples (1263 to 1662 ppm) while the MVKs have values of 92 to 733 ppm. Rubidium values range from 25 to 350 ppm. Strontium varies from strongly negative anomalies to almost positive anomalies, with [Sr/Sr*] values of 0.23 to 0.99 ($Sr/Sr* = Sr_N/\sqrt{Ce_N*Nd_N}$). Lead is consistently relatively depleted in the kimberlites, with Pb anomalies spanning ranges from 2 to 25 ppm.

Variability is also evident in the high field strength elements (HFSE) such as Zr, Hf, Nb and Ta. Zirconium and Hf display negative anomalies in some kimberlites and positive anomalies in others, with Zr*=0.29-1.24 ($Zr/Zr* = Zr_N/(\sqrt{Nd_N*Sm_N})$). Niobium values range from 46 to 140 ppm and Ta values range from 3 to 10.5 ppm.
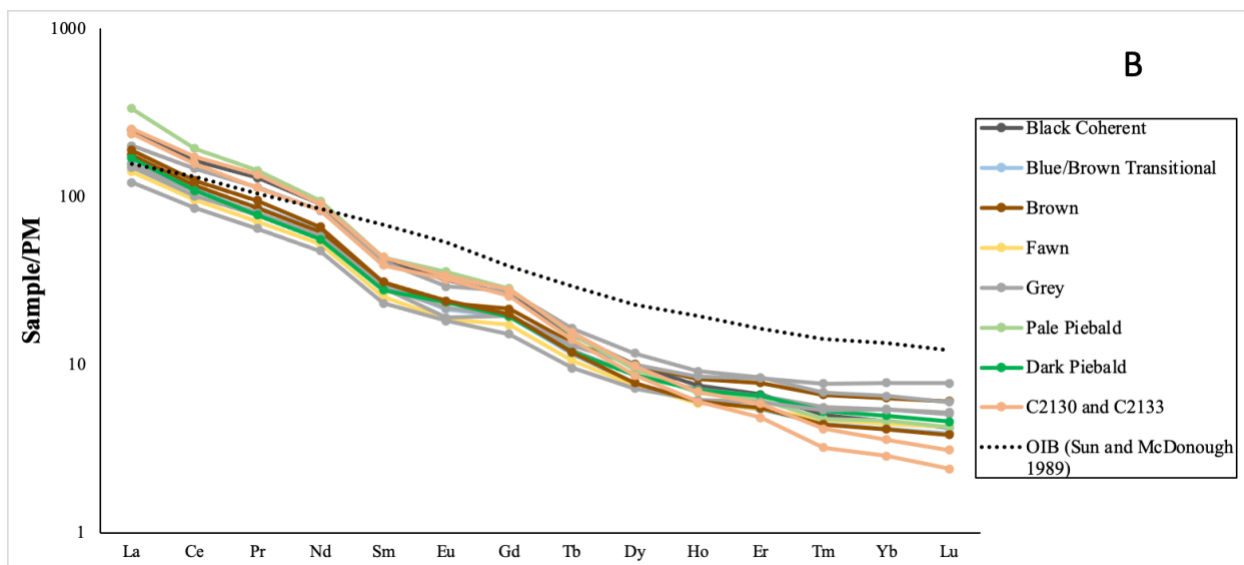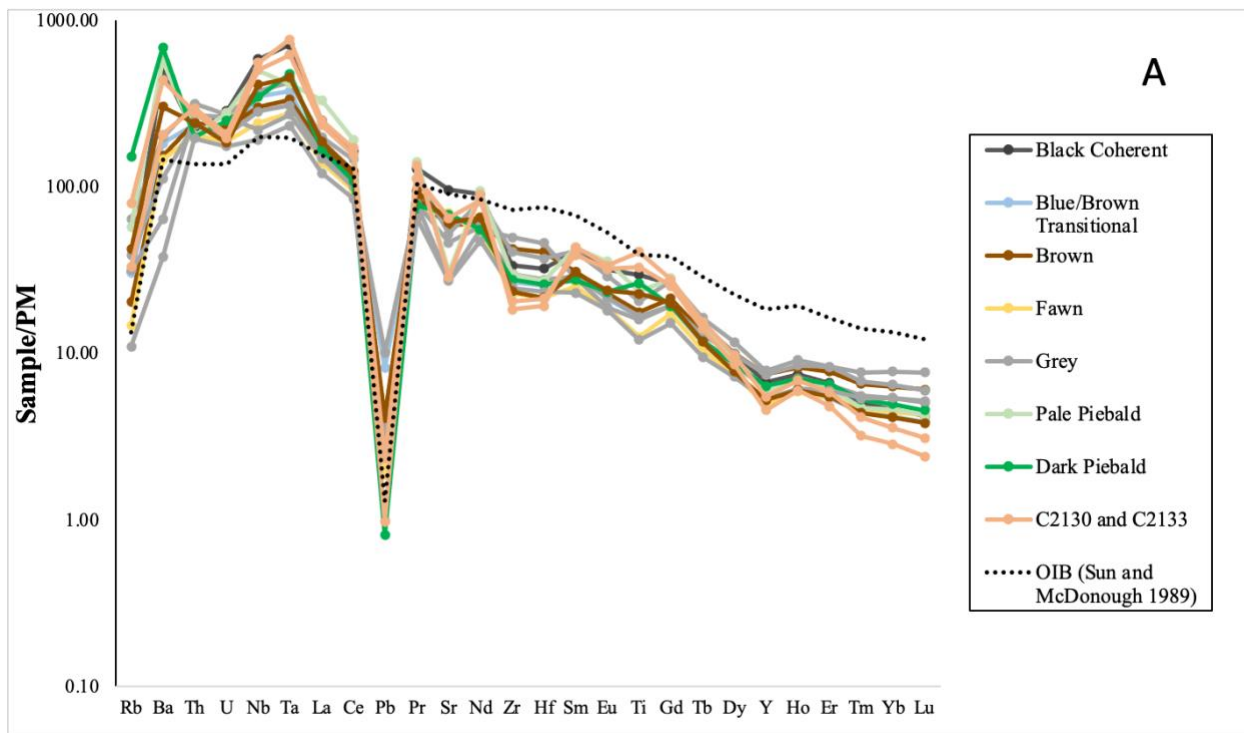
Figure 6: Primitive mantle normalized trace element spider diagram (a) and rare earth element diagram (b). Primitive mantle values are from McDonough and Sun 1995. Ocean island basalt (OIB) values are from Sun and McDonough 1989. OIB are generated by shallower (and typically higher degrees of) partial melting resulting in more subdued slopes in REE patterns.

4.2 Mantle Xenolith Whole-Rock Major- and Trace Element Abundances

The mantle xenoliths can be broadly divided into peridotites, pyroxenites and amphibolites, which are considered separately.

Peridotites range from 33.2 to 47.8 wt. % MgO, <0.05 to 2.0 wt. % K_2O, 0.4 to 2.8 wt. % Al_2O_3 and <0.05 to 0.3 wt. % P_2O_5. TiO_2 spans from <0.05 to 0.6 wt. %, except for the harzburgite with a phlogopite vein (2.3 wt. %). LOI varies from 5.5 to 12.1%. Pyroxenites have lower MgO wt. % than peridotites, with values of 23.7 and 26.0 wt. %, and much higher Al_2O_3 values (6.8 and 13.7 wt. %). The amphibolite C2115 is enriched in Na_2O (3.8 wt. %), CaO (9.4 wt. %), and P_2O_5 (0.6 wt. %) and TiO_2 (4.6 wt. %). Pyroxenite LOI values are 1.7 and 4.3% while the amphibolite's LOI is 1.0%.

One peridotite sample, the altered garnet lherzolite C2124, is significantly enriched in K_2O and P_2O_5, similar to kimberlite values (**Figure 7**).
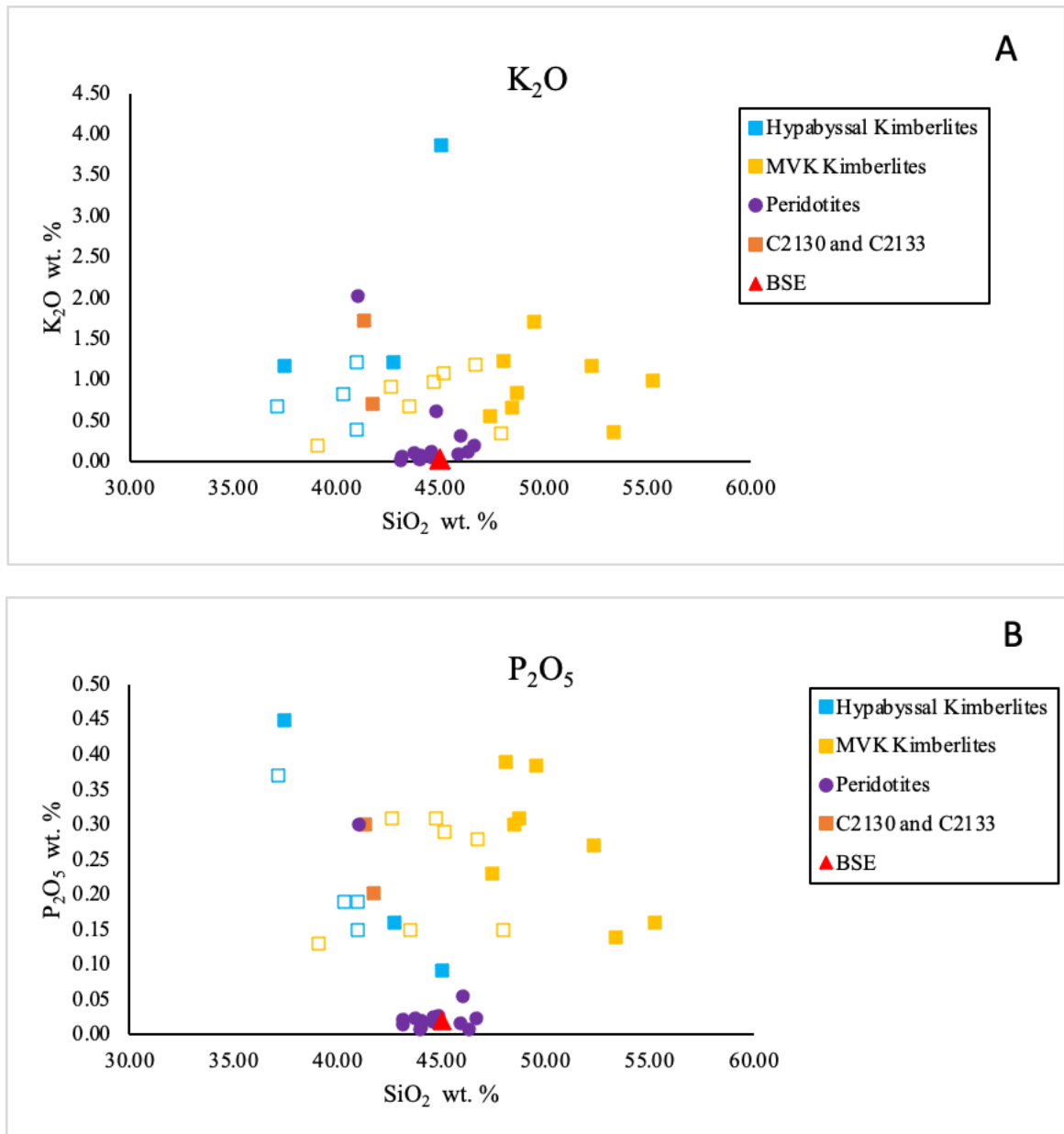
Figure 7: a) K_2O and b) P_2O_5 versus SiO_2 Harker plots. Filled-in symbols are data from this study, and outlined symbols are previously published data from Robinson 1975, Wu et al. 2013, and Dongre and Tappe 2019. The bulk silicate earth value is from McDonough and Sun 1995.

Primitive mantle normalized trace element abundances for the mantle xenoliths are

plotted in **Figure 8**. The peridotites' rare earth elements (**Figure 9**) span concentrations of <1

× PM to >10 × PM. They are enriched in the LREE/HREE, with La/Yb values ranging from 6 to 114. The highest slope by far is the Harzburgite with phlogopite veins (C2116), and the second highest La/Yb value is 89. Three peridotites have very low slopes with La/Yb values <8. These are C2128 (Harzburgite), C2120 (Garnet Lherzolite), and C2134 (Garnet Lherzolite).

The fluid mobile LILE display movement particularly in Sr, Rb, and Ba. Barium concentrations for peridotites vary from 8.5 ppm to 729 ppm, and Rb concentrations vary from 1.25 ppm to 196 ppm. Strontium/Sr* anomalies vary from 0.46 to 7.58, with some samples displaying strong positive anomalies, and others negative anomalies relative to elements on either side.

Sample C2116, the Harzburgite with a phlogopite vein, displays the most notable enrichments in the high field strength elements Nb, Ta, Zr and Hf. Zirconium and Hf values display significant variations between xenoliths, from moderately negative to strongly positive anomalies, with Zr/Zr* ranging from 0.30 to 2.01.

The two pyroxenite samples have very shallow REE slopes, with La/Yb values of 4.4 and 2 respectively. They have positive Sr and Eu anomalies. Sample C2122 has trace element abundances less than 100 x PM, except for a strong Ba enrichment of over 1000 × PM value. Sample C2126 has trace element abundances between 1 and 100 × PM except for Pb. The amphibolite C2115 has trace element abundance patterns similar to kimberlites, with the most incompatible trace elements reaching values of between 100 and 1000 × PM. It has a large lead anomaly, and enrichment in LREE/HREE with La/Yb of 41.
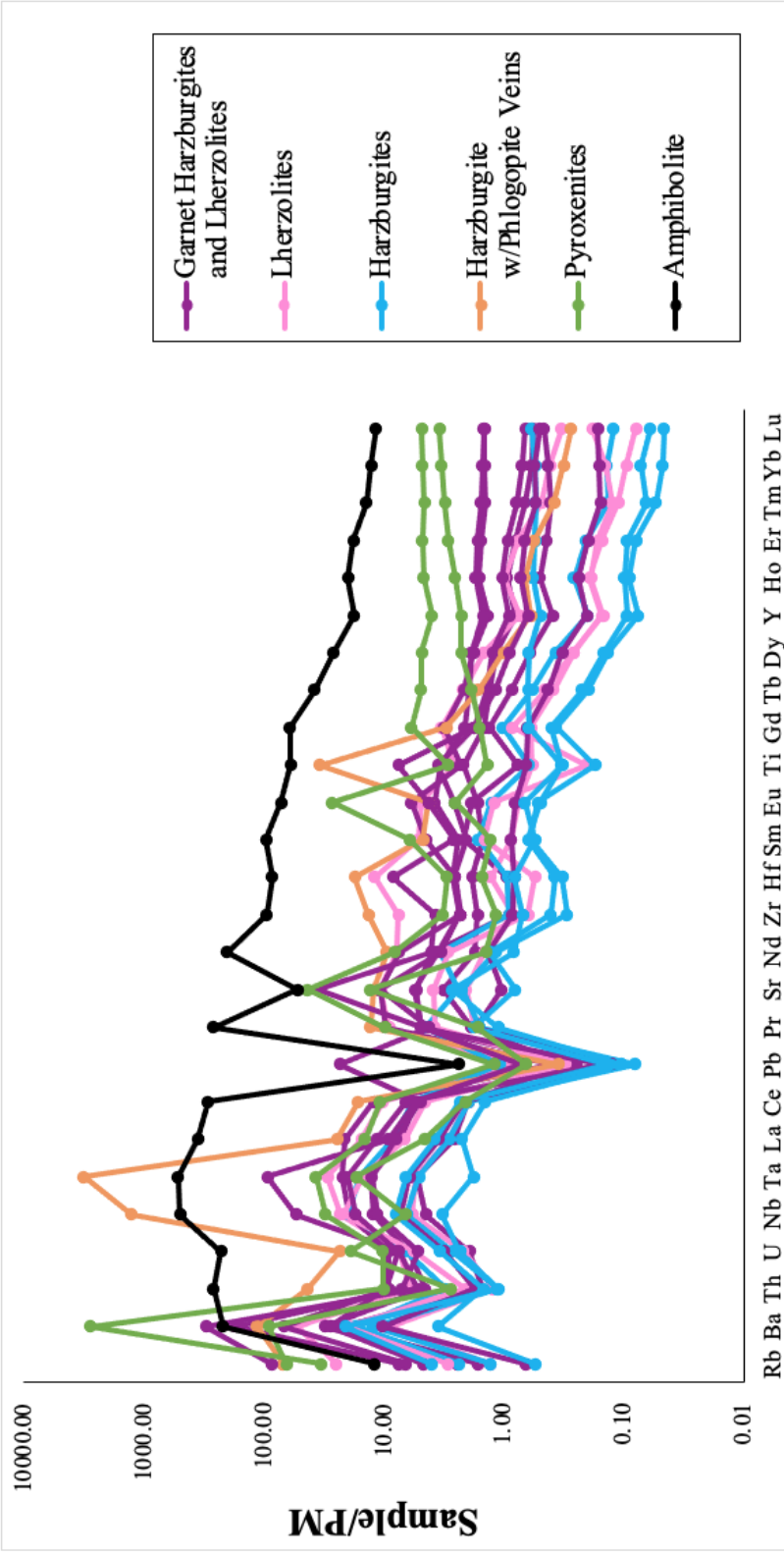
Figure 8: Mantle xenolith primitive mantle normalized trace element spider diagram. Primitive mantle values are from McDonough and Sun 1995

26
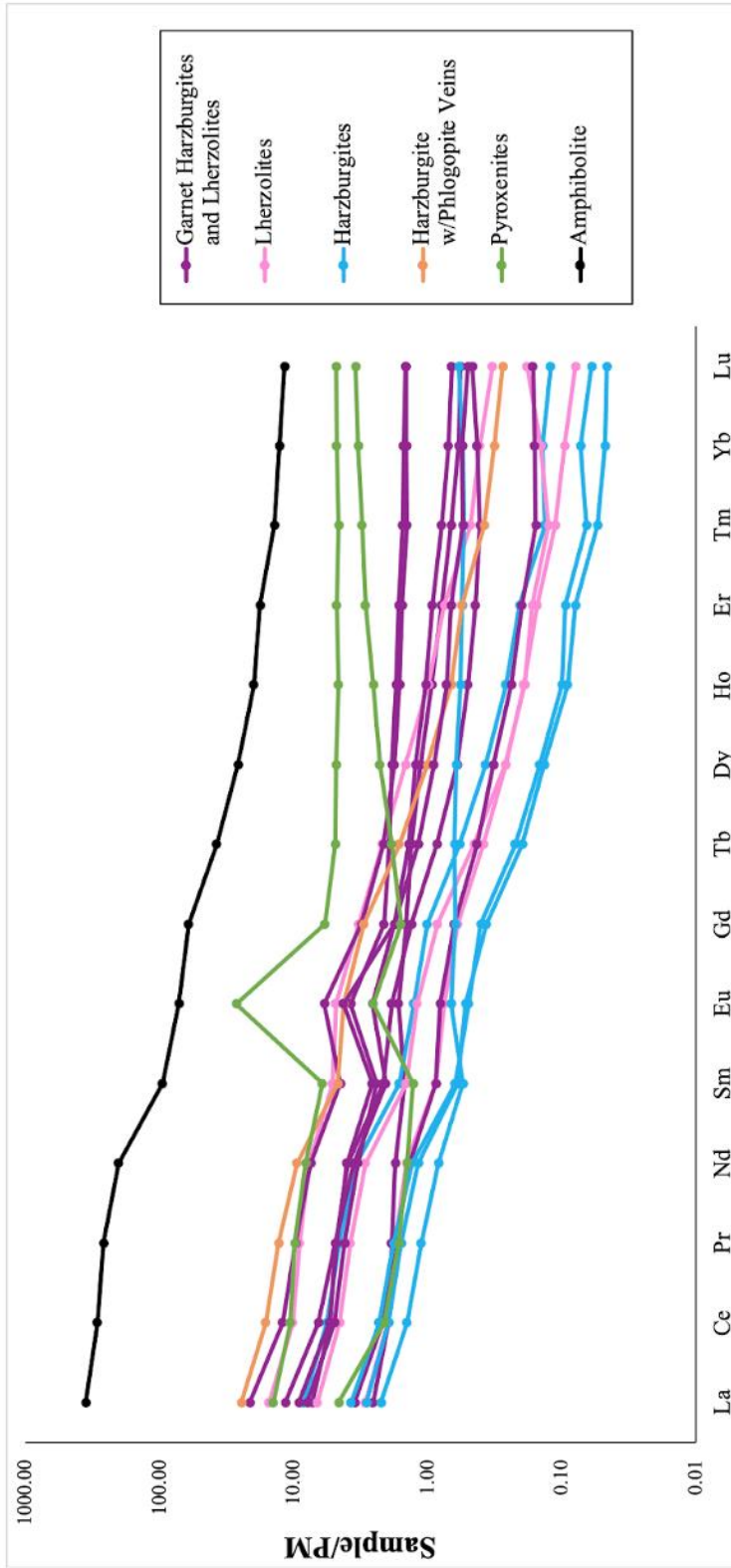
Figure 9: Mantle xenolith primitive mantle normalized rare earth element diagram. Primitive mantle values are from McDonough and Sun 1995

There is a broad correlation of increasing incompatible trace element abundances with increasing modal % melt infiltration **(Figure 10)**. The spread in peridotite rare earth element abundances may partially be explained by varying levels of kimberlite melt infiltration.
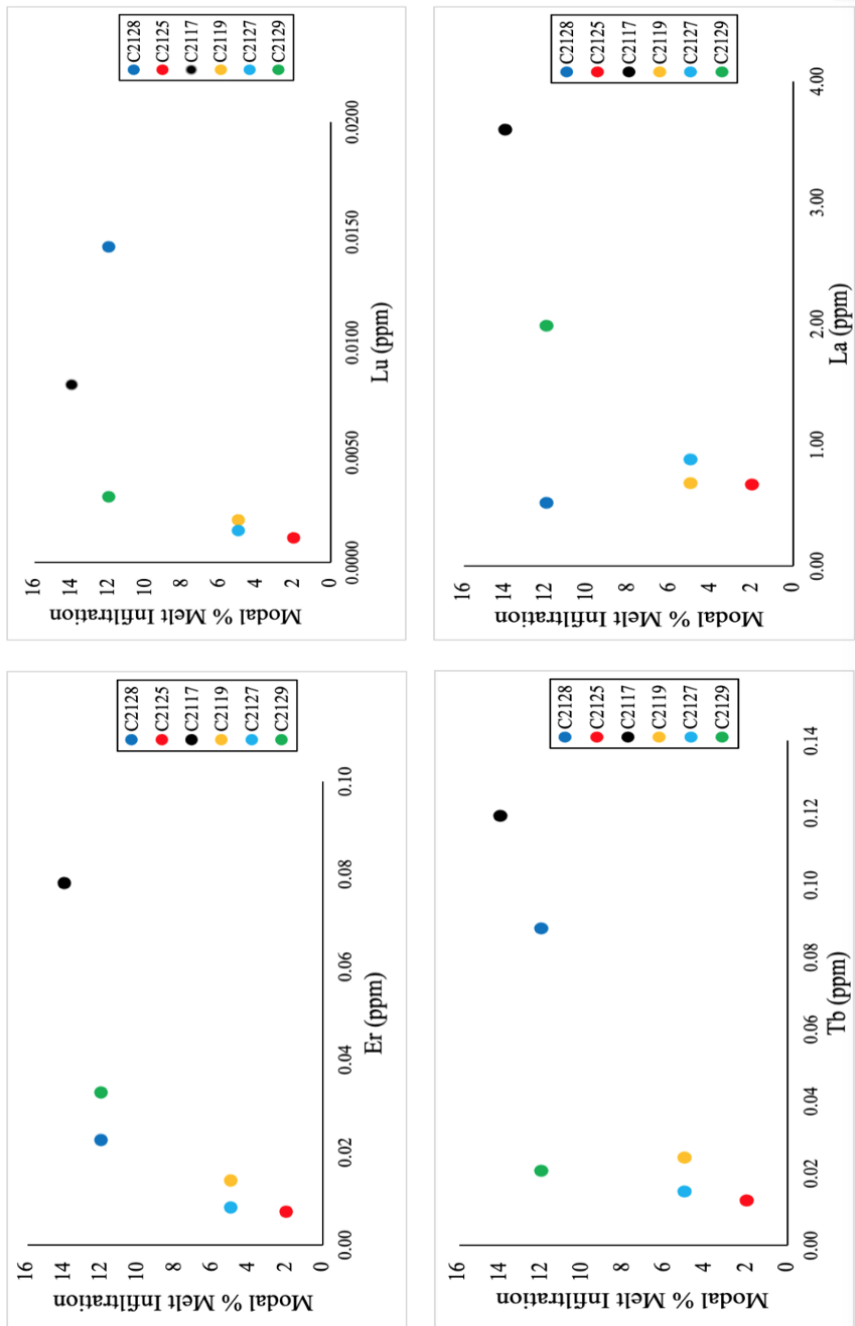
Figure 10: Modal percentages of melt infiltration in select peridotites versus the rare earth elements Er, Lu, Tb, and La. Peridotite samples were selected based on color contrast in the thin sections, allowing the greatest accuracy of estimating modal percentages of melt infiltration.

4.3 Kimberlite Osmium Isotope and Highly Siderophile Element Abundances

Osmium isotope and highly siderophile element abundances are reported in **Table 5** and **Table 6**. Measured $^{187}Os/^{188}Os$ ratios for the various Cullinan kimberlite facies range from 0.1223 to 0.1672. The highest value belongs to the Brown kimberlite (C2111) and the lowest to C2133.

The Dark Piebald sample has a significantly more radiogenic measured $^{187}Os/^{188}Os$ ratio (0.1479) than the other two hypabyssal kimberlites, the Pale Piebald (0.12684) and Black Coherent (0.12251). The latter two, along with C2133 are the only kimberlite samples with relatively unradiogenic values measured, with measured γOs of -0.5, -1.5, and -2.5 respectively ($\gamma Os = ([^{187}Os/^{188}Os_{sample}/^{187}Os/^{188}Os_{BSE}]-1) * 100$).

Kimberlite HSE abundances range from 0.09 to 0.32 ppb [Re], 1.38 to 15.15 ppb [Pd], 1.74 to 3.54 ppb [Pt], 1.1 to 3.3 ppb [Ru], 0.23 to 1.98 ppb [Ir], and 0.52 to 2.45 ppb [Os]. Primitive mantle normalized highly siderophile element abundances are plotted in **Figure 11**. The Pale Piebald and Dark Piebald samples have the flattest primitive mantle normalized HSE patterns, reflected in relatively low Pd/Ir values (2.75 and 4.10). These Pd/Ir values are lower than all other kimberlite samples except for C2133, which has the least depleted compatible HSEs, and has the highest amount of Ir (1.98 ppb). The most fractionated samples are the Brown (Pd/Ir=20.7), Blue/Brown Transitional (Pd/Ir=18.4), and Grey (Pd/Ir=13.4) units.
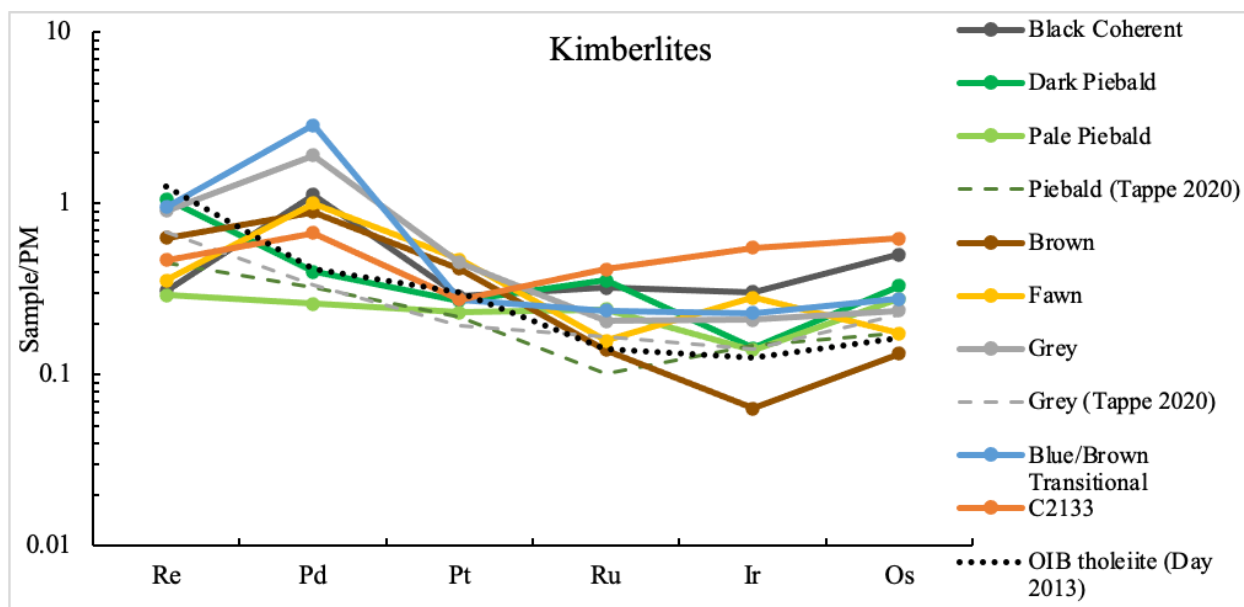
Figure 11: Kimberlite primitive mantle normalized highly siderophile element spider diagram. Previously published HSE data from Tappe et al. 2020 is represented by dashed lines. The grey dashed line represents the Grey kimberlite sample from Tappe et al. 2020 (CIM15-083), and the dark green dashed line represents the Piebald sample (CIM15-085). An OIB tholeiite HSE pattern is plotted for comparison (Day 2013).

4.4 Mantle Xenolith Osmium Isotope and Highly Siderophile Element Abundances

The measured ^{187}Os/^{188}Os abundances of the peridotite samples range from 0.1096 to

0.1244. Measured ^{187}Os/^{188}Os versus ^{187}Re/^{188}Os peridotite and kimberlite values from this study

are plotted in **Figure 12** along with previously published measured ^{187}Os/^{188}Os versus

^{187}Re/^{188}Os peridotite values from Pearson et al. 1995 and Carlson et al. 1999. The peridotite and

kimberlite samples from this study plot in a positive linear trend with R^2=0.9235. The

amphibolite and pyroxenite samples (C2115, C2122, and C2126) have ^{187}Os/^{188}Os values of

2.861, 0.9376, and 0.1796 respectively. Peridotite ^{187}Os/^{188}Os values do not appear to have a

correlation with Al$_2$O$_3$, and have similar values to two of the hypabyssal kimberlites and C2133

(**Figure 9**).
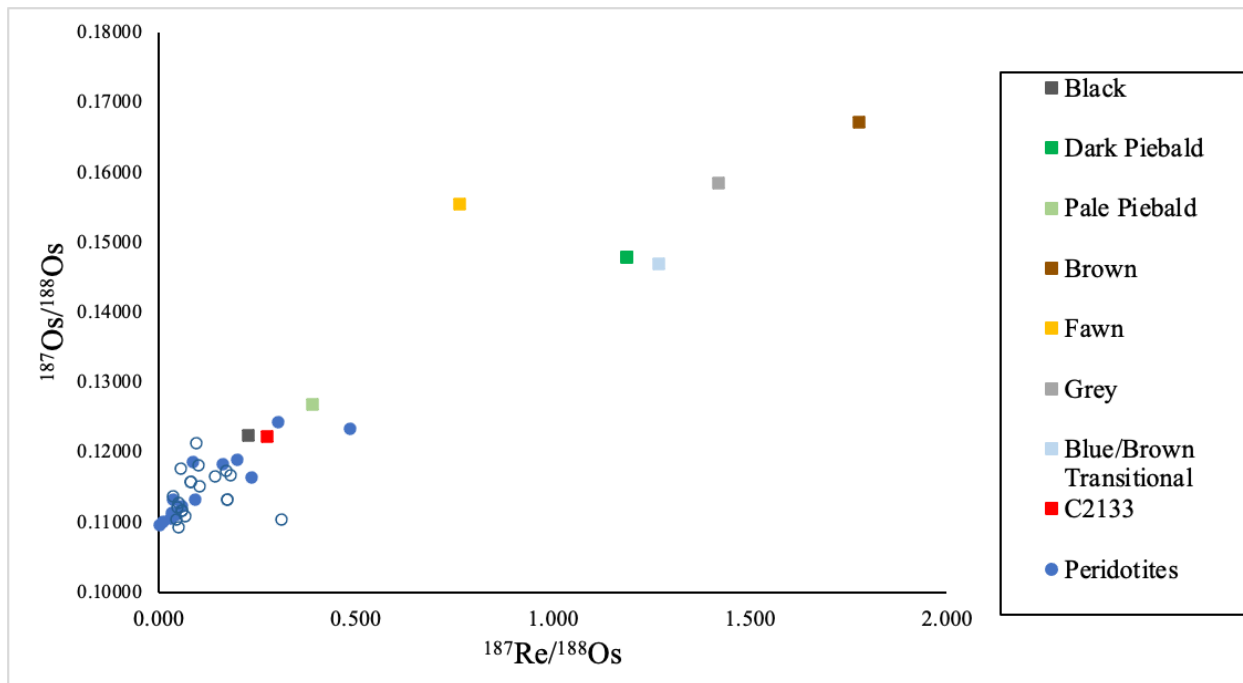
Figure 12: $^{187}Os/^{188}Os$ versus $^{187}Re/^{188}Os$ plot. Peridotites from this study are represented by filled-in circles, and kimberlites are represented by squares. Previously published Re-Os isotope data for Cullinan peridotites are represented by open circles, with data from Pearson et al. 1995 and Carlson et al. 1999.
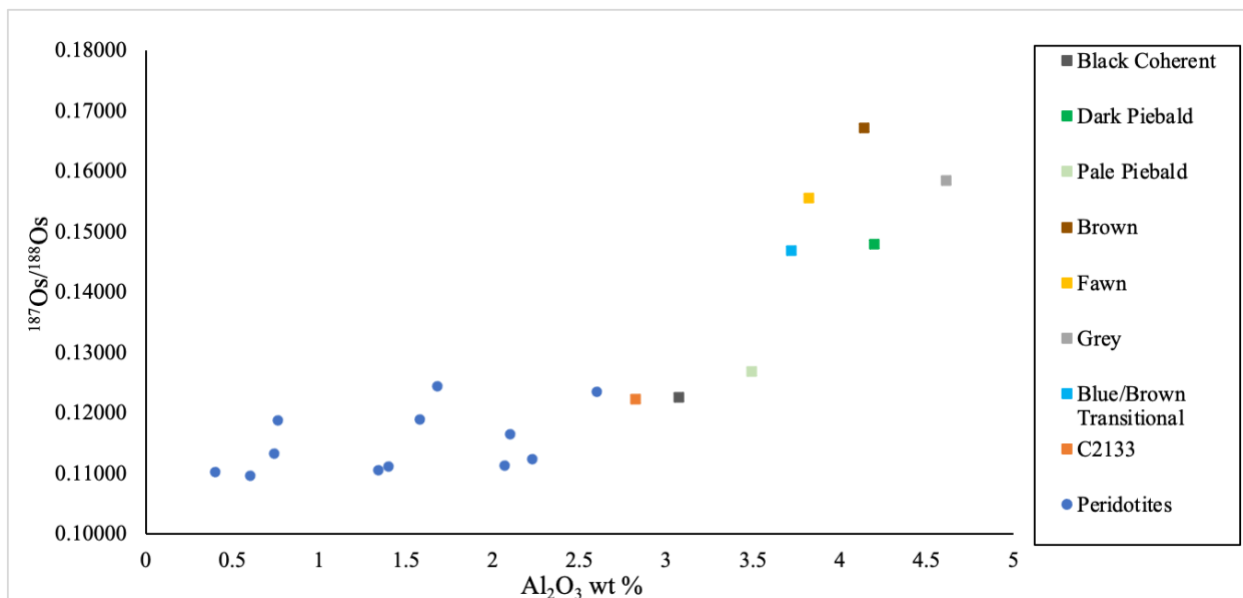
Figure 13: $^{187}Os/^{188}Os$ versus Al_2O_3 for kimberlites and peridotites. Kimberlites are denoted in squares and peridotites in circles.

Peridotite HSE abundances range from 0.01 to 0.43 ppb [Re], 0.04 to 14.3 ppb [Pd], 0.96 to 16.7 ppb [Pt], 3.58 to 13.9 ppb [Ru], 1.30 to 8.9 ppb [Ir], and 1.29 to 11.7 ppb [Os].

Primitive mantle normalized HSE abundances are plotted in **Figure 14** and **Figure 15**. The more incompatible HSEs such as Re, Pt, and Pd have the largest variations. Apart from C2128, which has the lowest Ir and Os values (1.30 and 1.29 respectively), the most compatible elements (Ru, Ir, Os) cluster close to PM values and have relatively little variation. Large variations in the incompatible elements are evident in the large range of Pd/Ir ratios (0.01 to 1.77) and Re/Os ratios (<0.01 to 0.1). C2116, the Harzburgite with the phlogopite veins (Pd/Ir=0.1), and C2127 (Re/Os=<0.1) are the most depleted samples. In the pyroxenite and amphibolite samples, Re, Pt, and Pd cluster close to PM values and are depleted in Pt and Ru. C2126 displays minor depletion in the most compatible HSE, while the amphibolite has the most extreme depletion, with a positive spike in Ir. These patterns are reminiscent of basaltic melts, particularly C2122 and C2126. OIB tholeiite and OIB alkali basalt patterns are plotted for comparison in **Figure 15**.
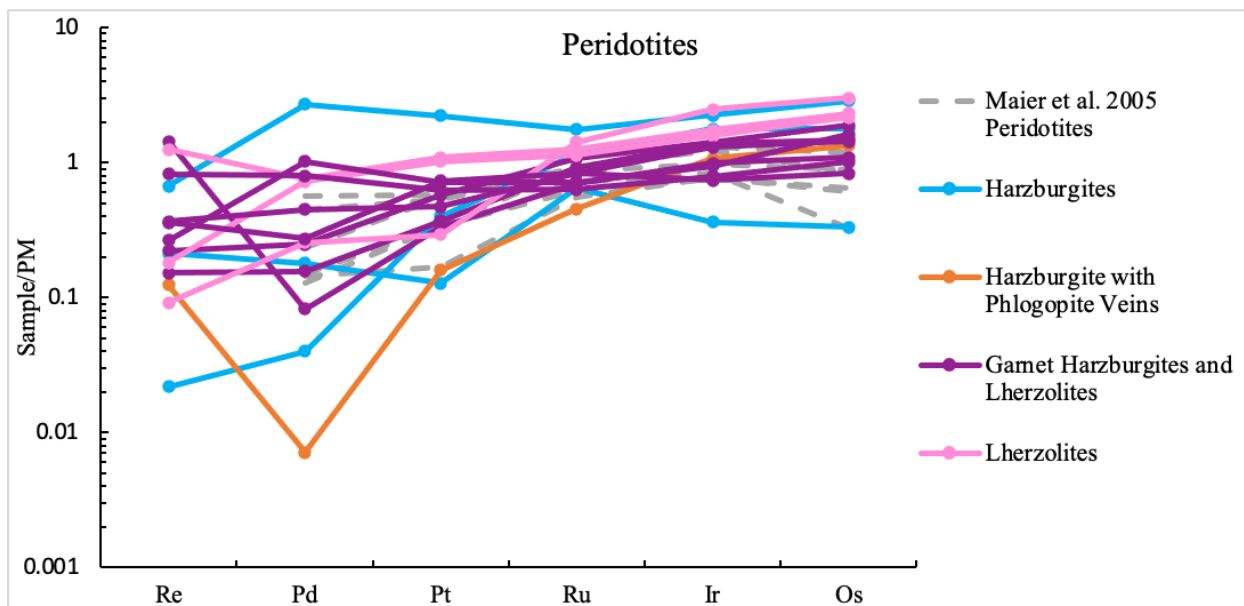
Figure 14: Primitive mantle normalized highly siderophile element spider diagram for peridotites. Previously published HSE data from Maier et al. 2005 is plotted for comparison in dashed grey lines. Samples from Maier et al. 2005 with semiquantitative data (i.e. reported as <0.5, <0.25, etc.) are not included.
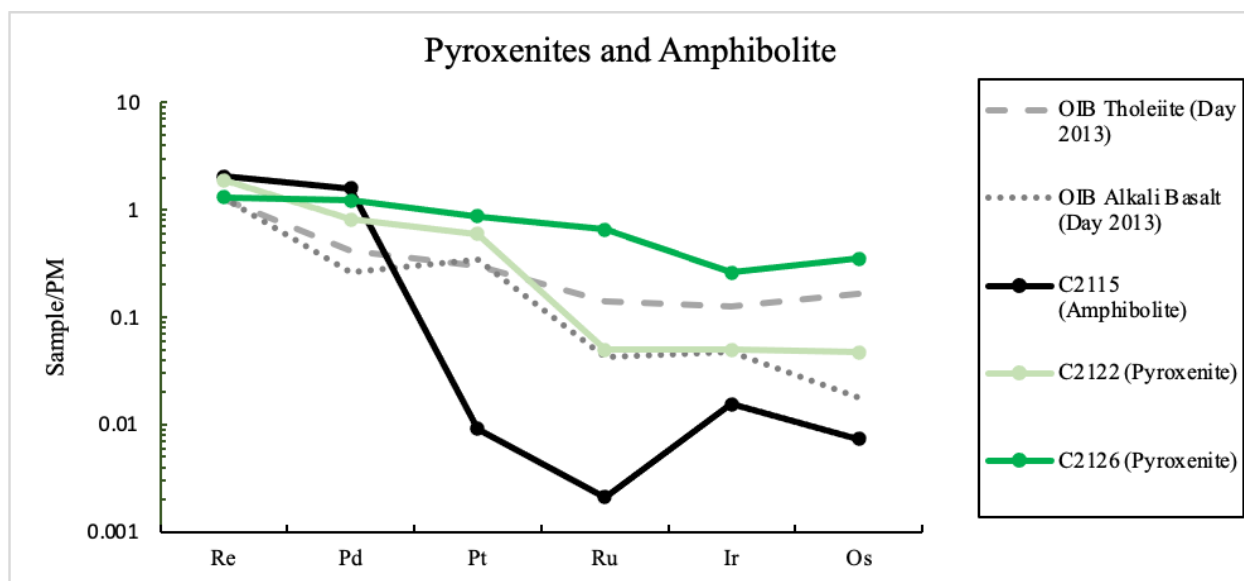
Figure 15: Primitive mantle normalized highly siderophile element spider diagram for the pyroxenites and amphibolite. Example OIB tholeiite and OIB alkali basalt HSE values are from Day 2013.

5. Discussion:

5.1 Peridotite Metasomatism and Kimberlite Melt Infiltration

A key consideration with peridotite xenoliths within kimberlites is the degree of fluid and/or melt modification that they may have experienced. Both can occur due to the great depths from which the xenoliths are entrained and the ubiquitous penetration of kimberlite magma and associated fluids that may take place (i.e., Walker et al. 1989, Pearson et al. 1995, Carlson et al. 1999). Within the samples I have studied this is seen in variations in the fluid-mobile large ion lithophile elements, especially for Sr, Rb, and Ba (**Figure 8**). Mineralogically, the presence of hydrous mineral veins such as phlogopite and serpentine serve as indicators of metasomatism in peridotites (i.e., Jones et al. 1982), most notably seen in sample C2116. The origin of serpentine may come from interaction of the kimberlite with non-magmatic water, though kimberlite melt has also previously been proposed as a serpentinizing fluid, as it may be able to degas significant amounts of water at low pressures similar to carbonatite melts (Sparks et al. 2006). Although this serpentinization is important to note, it does not have a strong effect on the Re-Os isotope systematics of peridotites in either magmatic or non-magmatic water environments (i.e., Carlson et al. 1999, Rudnick and Walker 2009, Day and Brown 2021).

There are some clear chemical indications of kimberlite melt infiltration. Typically, Archean cratonic peridotites are formed as residues of high degrees of partial melting of around 30% to >40% (Walter 1999, Pearson et al. 2004). Such high degrees of partial melting result in significant depletion in the incompatible trace elements, especially the highly incompatible trace elements such as the LREE. However, the peridotites in the sample suite that I studied display high LREE/HREE patterns indicating a secondary enrichment after major melt depletion (**Figure**

16). Though Bushveld magmas are also inferred to be relatively high in the LREE/HREE (Maier et al. 2000) and could have added LREE to the peridotite prior to entrainment, this is less likely, as the LREE/HREE enrichment for kimberlite is much more highly elevated and almost certainly due to kimberlite melt infiltration. Critically, such melt infiltration is observed in black melt veins pervading most kimberlite-borne mantle xenoliths. Kimberlite magmas directly engulfed the peridotites, and due to the large difference in trace element concentrations, a minor amount of melt infiltration can have significant impacts on the trace element patterns of peridotites. Such melt infiltration explains the strong similarity in the slopes of the REE patterns between the two rock types as well. Most peridotites have enrichments corresponding to addition of between 1%

and 10% kimberlite melt (**Figure 16**).
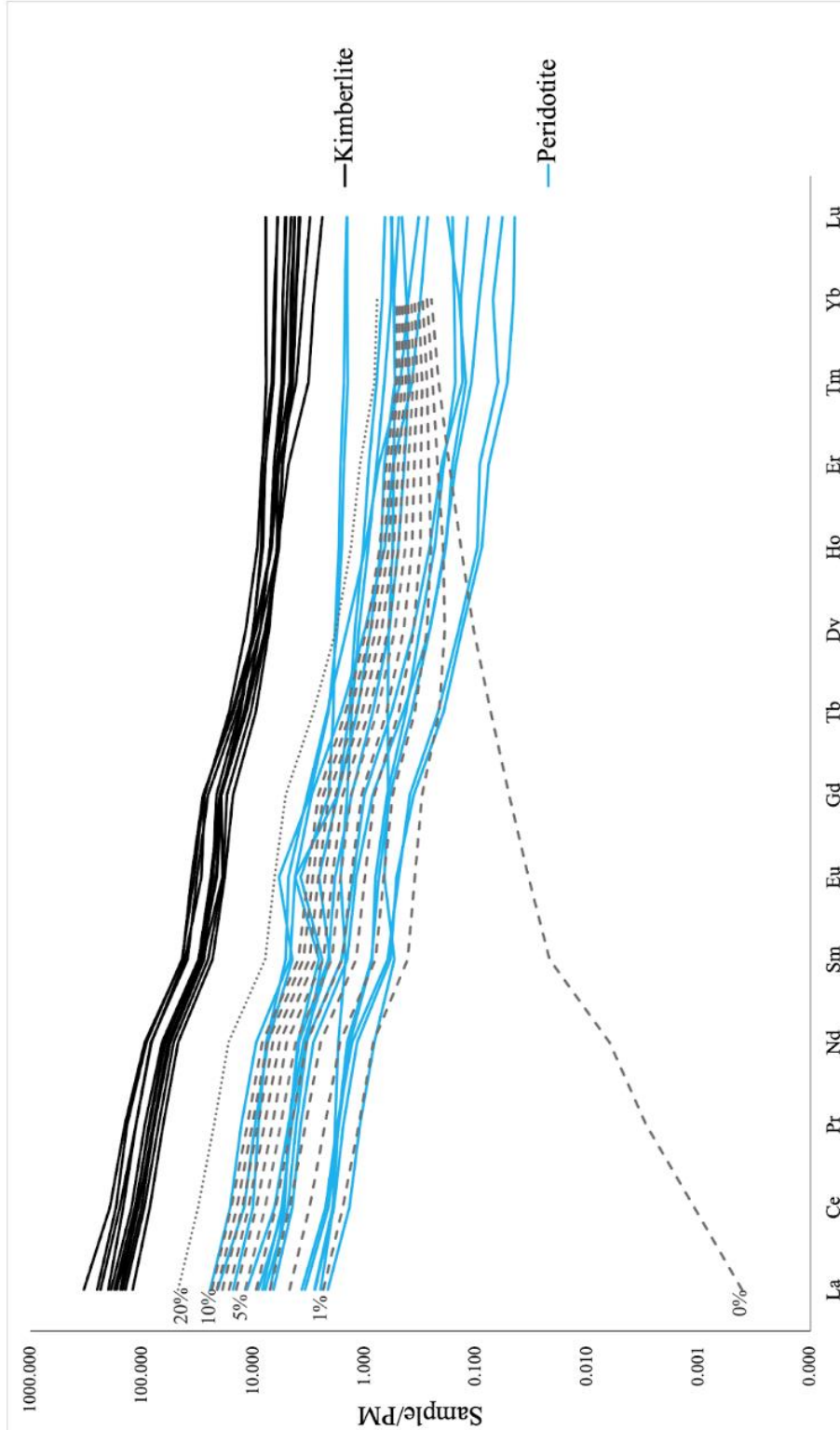
Figure 16: Primitive mantle normalized rare earth element trends of kimberlites and peridotites. Kimberlites are plotted in black, and peridotites are plotted in blue. The model estimating kimberlite melt infiltration is plotted in dashed grey lines of 1% increments based on the end member of 20% melt depleted lithosphere (maximum that can be modeled) and sample C2133, the kimberlite with the steepest La/Yb slope (La/Yb=122). A dotted 20% mixing line is also included for reference. This model is adapted from the REE model in Day et al. 2017.

La/Yb and Re/Os can be useful to plot, as they are REE and HSE ratios of elements with differences in compatibility. The kimberlites' and peridotites' influence on one another is observed in La/Yb versus Re/Os and ^{187}Os/^{188}Os plots (**Figure 17**). Both kimberlites and peridotites display broadly negative correlations in these figures. This is surprising, as La and Re are the more incompatible elements compared to Yb and Os respectively, and as a result one might reasonably expect a positive correlation if kimberlite melt-peridotite interaction alone had taken place.

One explanation of the negative trends in peridotite La/Yb versus Re/Os is that more depleted peridotites (low Re/Os) may be more susceptible to higher degrees of melt infiltration, which would increase La/Yb ratios over long periods of time in the lithosphere and interaction with very low degree partial melts. However, it is unknown why these rocks would have higher melt infiltration, as there is not strong evidence for higher porosity in more depleted peridotites. The negative trend in kimberlites likely is due to higher degrees of assimilation of metasomatized peridotite. Assimilating peridotite decreases Re/Os and ^{187}Os/^{188}Os values of kimberlite, and assimilating metasomatized samples increases La/Yb.
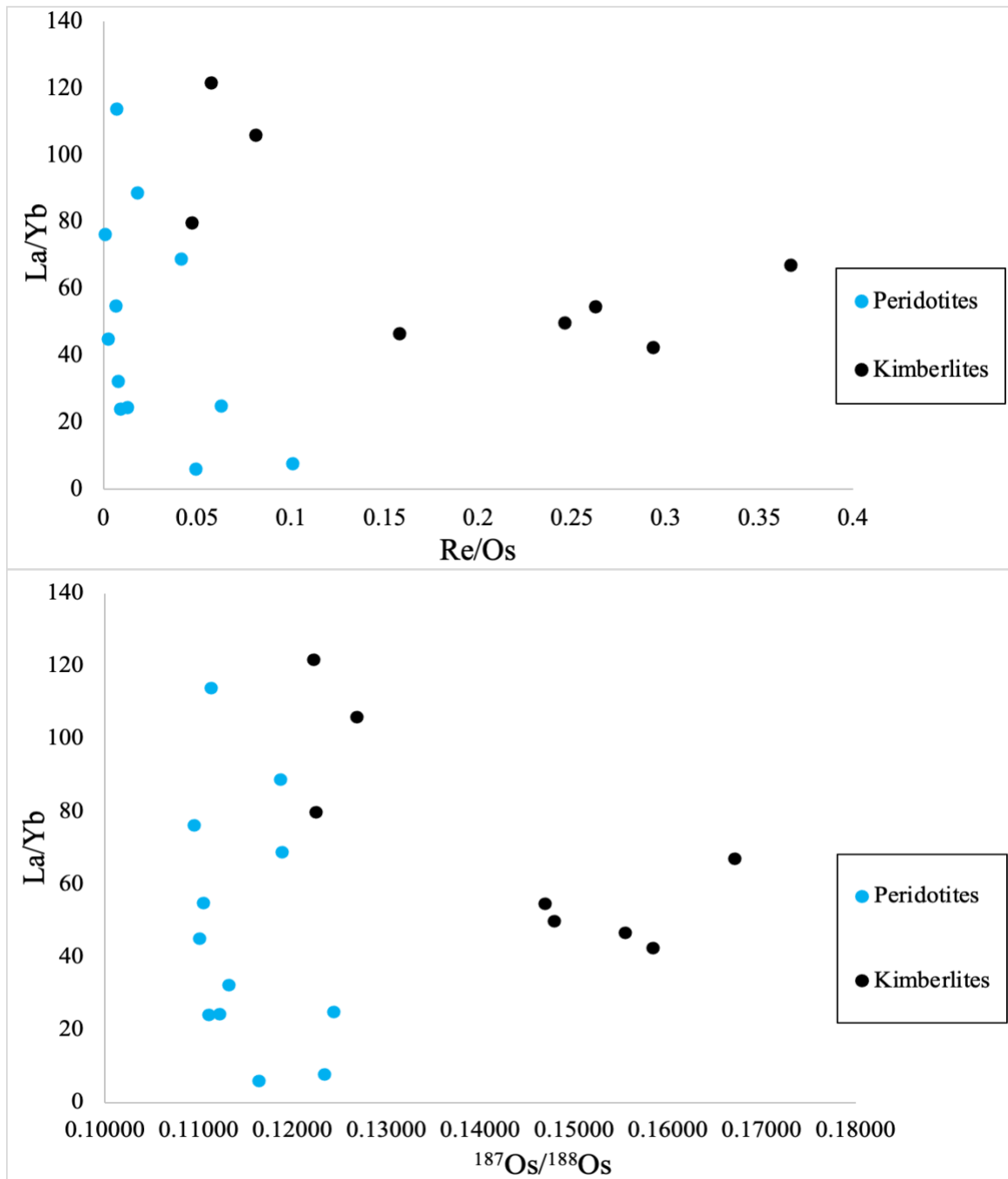
Figure 17: La/Yb versus Re/Os and La/Yb versus $^{187}Os/^{188}Os$ plots for peridotite and kimberlite samples. Peridotites are plotted in blue and kimberlites are plotted in black.

A similar surprising enrichment in incompatible elements is seen in the Re abundances of the peridotite samples. Rhenium concentrations are as high as 0.43 ppb (C2134), 0.27 ppb (C2118), and 0.25 ppb (C2121). Rhenium would not be expected in uncontaminated cratonic peridotites resulting from such high degrees of partial melt, as it is one of the most incompatible HSE (**Figure 14**). The common occurrence of Re in peridotites erupted from cratonic peridotites is often interpreted to reflect kimberlite melt addition. There may be an additional source of this Re as well, which is discussed in Section 5.4.

5.2 Variations in $^{187}Os/^{188}Os$ in Cullinan Kimberlite Facies Reflect Degrees of Cratonic Lithospheric Mantle Assimilation

My study reveals that the different Cullinan kimberlite facies span a wide range in whole-rock measured $^{187}Os/^{188}Os$ values (0.1223 to 0.162). The samples plot in a well correlated $^{187}Re/^{188}Os$ versus $^{187}Os/^{188}Os$ line between peridotites and kimberlites, which has an $R^2=0.9235$ (**Figure 12**). Though this trend is linear, it cannot represent an isochron, as the peridotites are in an open system. The most logical explanation for such a linear relationship in samples which have experienced assimilation and melt infiltration would be a mixing line (Day et al. 2019). This is consistent with the apparent age derived from this linear relationship, 1.9 Ga, which is older than the kimberlite itself.

A model is created to estimate the percentages of mixing of peridotite into the various kimberlite facies relative to the end member Brown Kimberlite and the end member peridotite C2127, which has the lowest $^{187}Re/^{188}Os$ value (0.0045) (**Figure 18**). It is evident that variations in the measured kimberlite whole-rock $^{187}Os/^{188}Os$ isotopic abundances are explained by variable

39

assimilation of peridotite, which can be considered cratonic lithospheric mantle (CLM), by the

kimberlite melt. Larger amounts of CLM assimilation would result in lower $^{187}Os/^{188}Os$ values.

Quantitative estimates of peridotite assimilation into kimberlite relative to the end-member

Brown kimberlite are listed in **Table 9**.
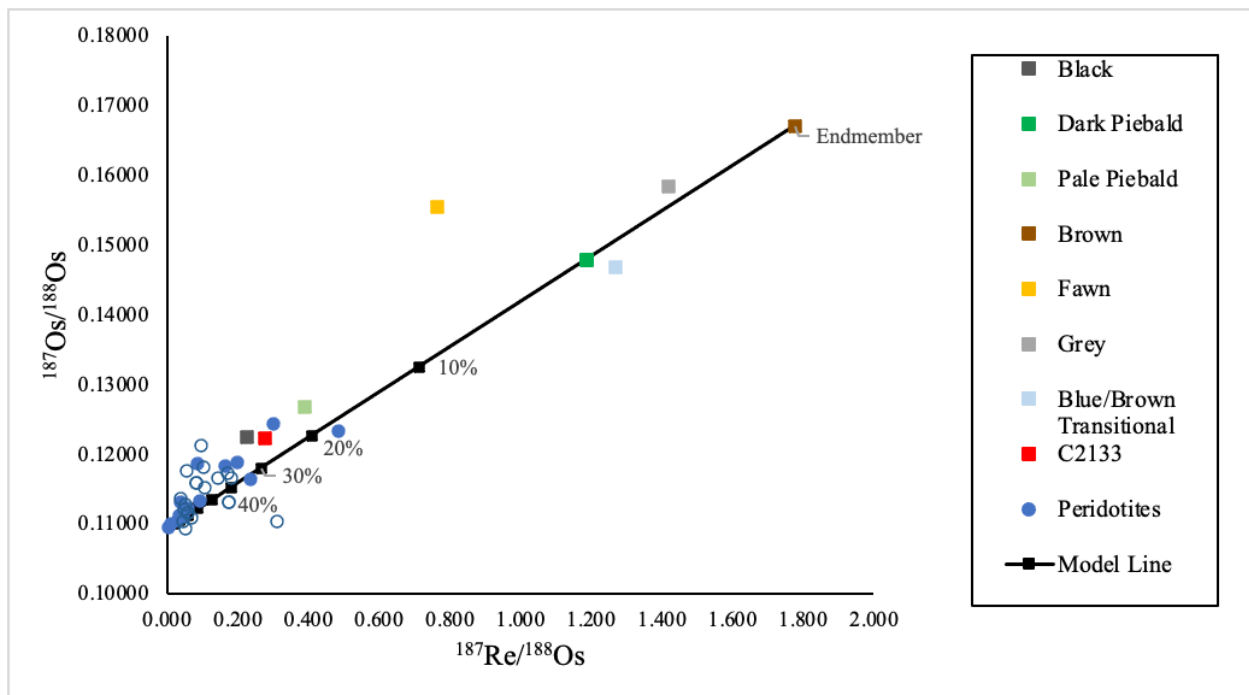
Figure 18: $^{187}Os/^{188}Os$ versus $^{187}Re/^{188}Os$ mixing line. Each black square represents a 10% mixing interval. Percentages are calculated using the measured $^{187}Os/^{188}Os$ and $^{187}Re/^{188}Os$ values, as well as correcting for Os concentrations and atomic weights. Peridotites from this study are represented by filled-in circles, and kimberlites are represented by squares. Previously published Re-Os isotope data for Cullinan peridotites are represented by open circles, with data from Pearson et al. 1995 and Carlson et al. 1999.

Table 9: Assimilation of CLM relative to Brown kimberlite. Kimberlite type classifications are from Bartlett 1994.

Grey Kimberlite (Type 1)	1.5%
Brown Kimberlite (Type 2)	Endmember
Pale Piebald Kimberlite (Type 3A)	20%
Dark Piebald Kimberlite (Type 3B)	3.5%
Black Coherent Kimberlite (Type 3C)	33%
Blue/Brown Transitional Kimberlite	3%
Fawn Kimberlite	7%
C2133	29%

Plotting $^{187}Os/^{188}Os$ versus 1/Os (**Figure 19**) data from this study shows a single positive trend ($R^2=0.8175$) for both kimberlites and peridotites, which also supports mixing between the kimberlites and peridotites, instead of there being distinct trends for each of the two rock types. Likewise, the mixing model is supported by plotting $^{187}Os/^{188}Os$ versus Al_2O_3 (**Figure 13**), which reveals that the kimberlite samples with the highest peridotite addition (Pale Piebald, Black and C2133) plot more similarly to the peridotites than other kimberlites.
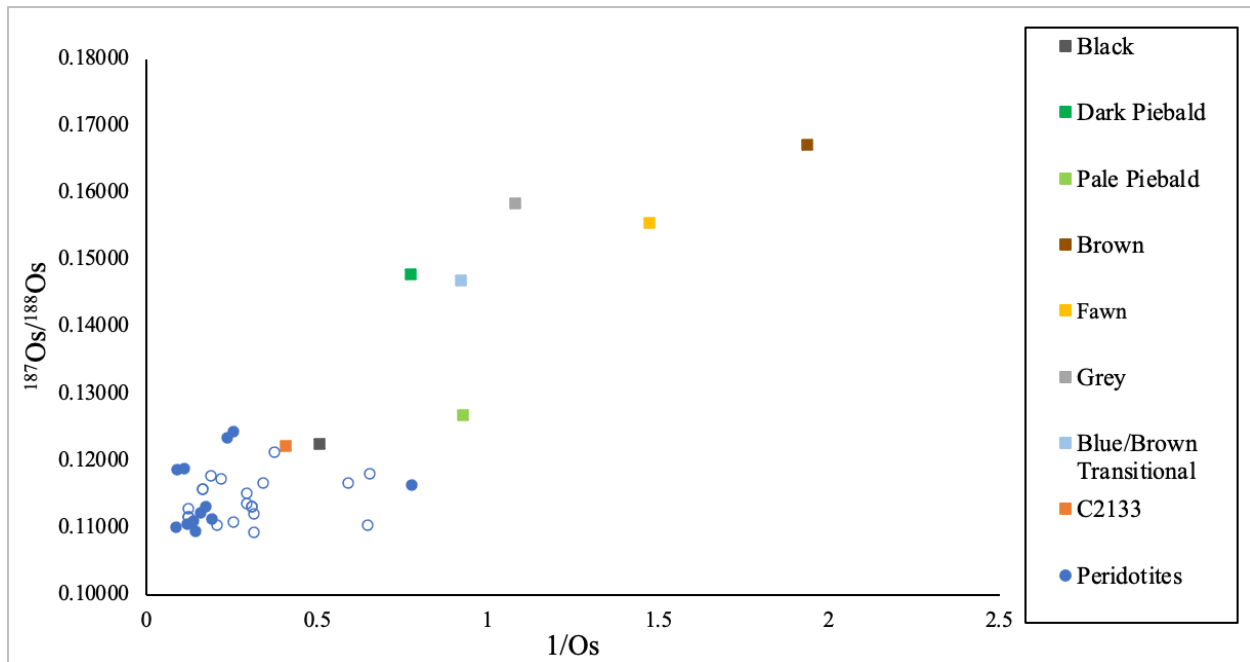
Figure 19: $^{187}Os/^{188}Os$ versus 1/Os. Peridotites from this study are represented by filled-in circles, and kimberlites are represented by squares. Previously published data from Pearson et al. 1995 and Carlson et al. 1999 is represented by open circles.

The clearest variations in peridotite assimilation are seen in thin-sections of the least fractured kimberlites, such as the hypabyssal Pale Piebald and Dark Piebald kimberlites. The Pale Piebald unit (**Figure 20B**) has more visible olivine macrocrysts than the Dark Piebald unit (**Figure 20A**) (33 modal % versus 11 modal %). Higher amounts olivine macrocrysts (which likely came from peridotite) is reflected in the much lower $^{187}Os/^{188}Os$ values for the Pale Piebald kimberlites (0.1268) compared to the Dark Piebald (0.1479).
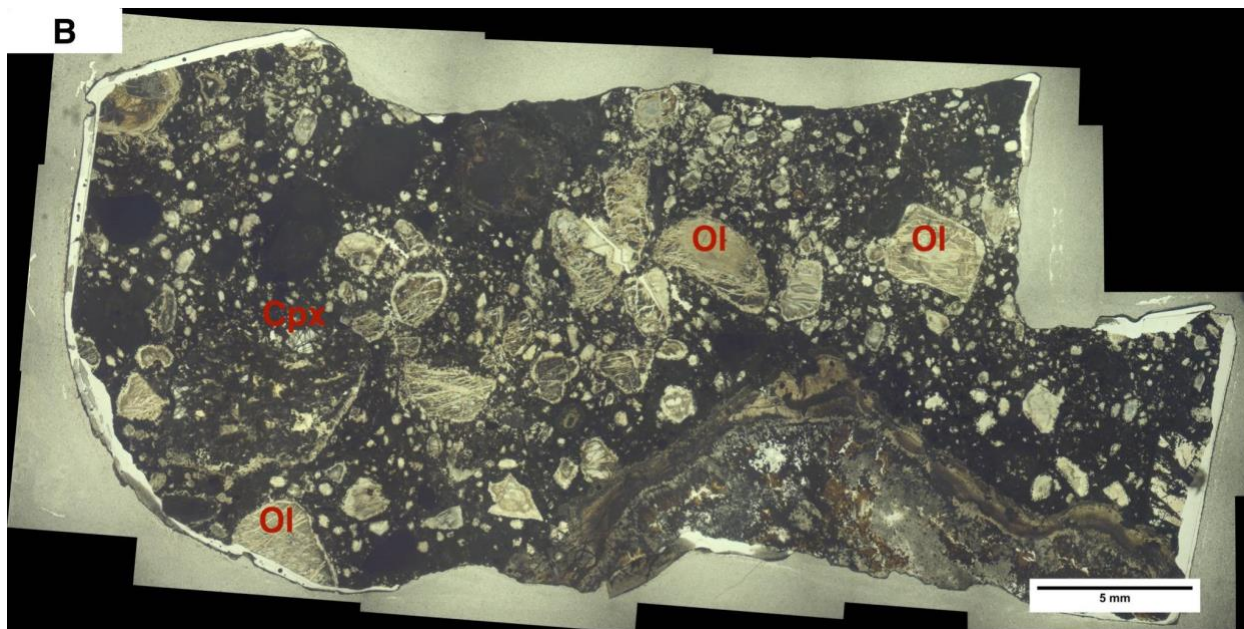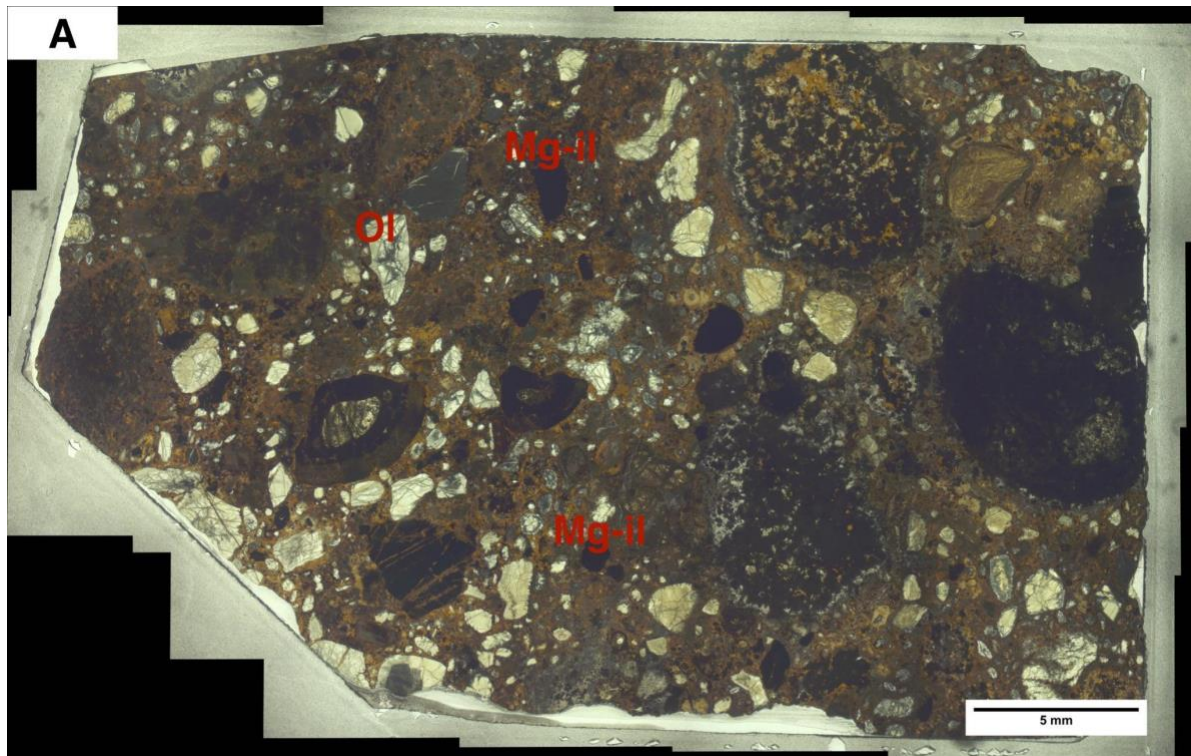
Figure 20: Thin section images of a) C2103, the Dark Piebald kimberlite, and b) C2104, the Pale Piebald kimberlite. Both thin sections are imaged in plane polarized light. Scale bar is 5 mm. Ol=olivine, Mg-il=Magnesium ilmenite, Cpx=clinopyroxene

Peridotite assimilation may not always be visible as xenoliths or macrocrysts, especially in the volcaniclastic samples. Xenolithic material can disaggregate during kimberlite ascent and be incorporated into the matrix, or fracture during explosive emplacement. As a result, instead of attempting to estimate the amount of CLM assimilation in the end member kimberlite with the lowest amount of CLM assimilation, the mixing model estimates the percentages relative to this end member, which is the Brown Kimberlite (**Table 9**).

5.3 Variable CLM Assimilation and its Importance to Diamond Grade Distribution at Cullinan and Elsewhere

The Brown kimberlite has the highest diamond grade (measured in carats per hundred tons) of diamonds in the Cullinan mine, as seen from sampling the 347-meter and 538-meter levels (Bartlett 1994, personal correspondence with the mine geologists). Amounts of 69,000 and 42,931 tons of rock were treated on these respective levels during the sampling process. Diamond grade of the Brown kimberlite was determined to be 55 cpht on the 347-meter level and 78.8 cpht on the 538-meter level (Bartlett 1994).

My evaluation shows that though this unit has the highest diamond grade, it also has the least peridotite assimilation. This may possibly be related to the fact that diamondiferous eclogites rather contain higher diamond concentration than diamondiferous peridotite (personal correspondence with mine geologists). A possible explanation is that peridotites may be 'diluting' the sample from the more diamondiferous eclogites. Sampling eclogite distributions within the mine could be useful in the future.

When determining differences in diamond grade between the units, internal waste dilution is important to consider. The Grey Kimberlite, for example, contains significant dilution

from country rock such as Waterberg quartzite and conglomerates (Bartlett 1994). Another

consideration when considering the diamond distribution is that diamond grades are affected up

to 15 meters of the gabbro sill, as kimberlites up to this distance are metamorphosed..

Furthermore, diamonds within one meter of the sill are typically completely destroyed (Bartlett

1994).

5.4 Cullinan Peridotite Time of Rhenium Depletion ages: A Reflection of Bushveld

Refertilization or New Lithospheric Formation?

Rhenium-Os isotopes are useful to estimate the age of melt depletion events, utilizing the

difference in compatibility between Re and Os (Allègre and Luck 1980). Various models of

applying Re-Os isotopes to estimate the ages of peridotites have been developed. T_{RD} (Total

Rhenium Depletion) is defined as $\frac{1}{\lambda}(\frac{187/188Os_{BSE}-187Os/188Os_{sample}}{187Re/188Os_{BSE}}+1)$ (Walker et al. 1989). This

assumes that the original Re/Os in a rock is zero. Therefore, if there was a later infiltration of a

Re (such as through kimberlite melt infiltration) the model would not account for ingrowth, and

this age estimate would be too low. As a result, T_{RD} may be considered a lower bound, and T_{MA}

$\frac{1}{\lambda}(\frac{187/188Os_{BSE}-187Os/188Os_{sample}}{187Re/188Os_{BSE}-187Re/188Os_{sample}}+1)$ may be considered an upper bound (Luck and Allègre 1984).

A variation of T_{RD} called 'T_{RD} eruption' may also be used to correct for the $^{187}Os/^{188}Os$ ingrowth

of ^{187}Re, but this assumes that all Re was added to the peridotite at the time of kimberlite

eruption (Pearson et al. 1995). T_{RD} eruption ages for the Cullinan peridotites are plotted in

Figure 21.

Previous Re-Os isotopic studies have shown that Cullinan peridotites display lower than

average T_{RD} ages than other on-craton peridotites, such as those from Kimberley, Letlhakane,

Newlands, Finsch, Venetia, and Lesotho (Irvine et al. 2001). In fact, numerous Cullinan peridotites display Proterozoic T_{RD} ages (Carlson et al. 1999, Pearson et al. 1995). Proposed explanations for this include refertilization of the mantle during the Bushveld event (Carlson et al. 1999, Pearson et al. 1995, James et al. 2001) and the formation of new Proterozoic lithosphere through plume-driven recratonization (Liu et al. 2021). Due to limitations of the dating system, T_{RD} ages are best interpreted in conjunction with major element, trace element, and HSE data (Pearson et al. 2002, Pearson et al. 2004, Rudnick and Walker 2009). My new T_{RD} ages and HSE data add to this debate.
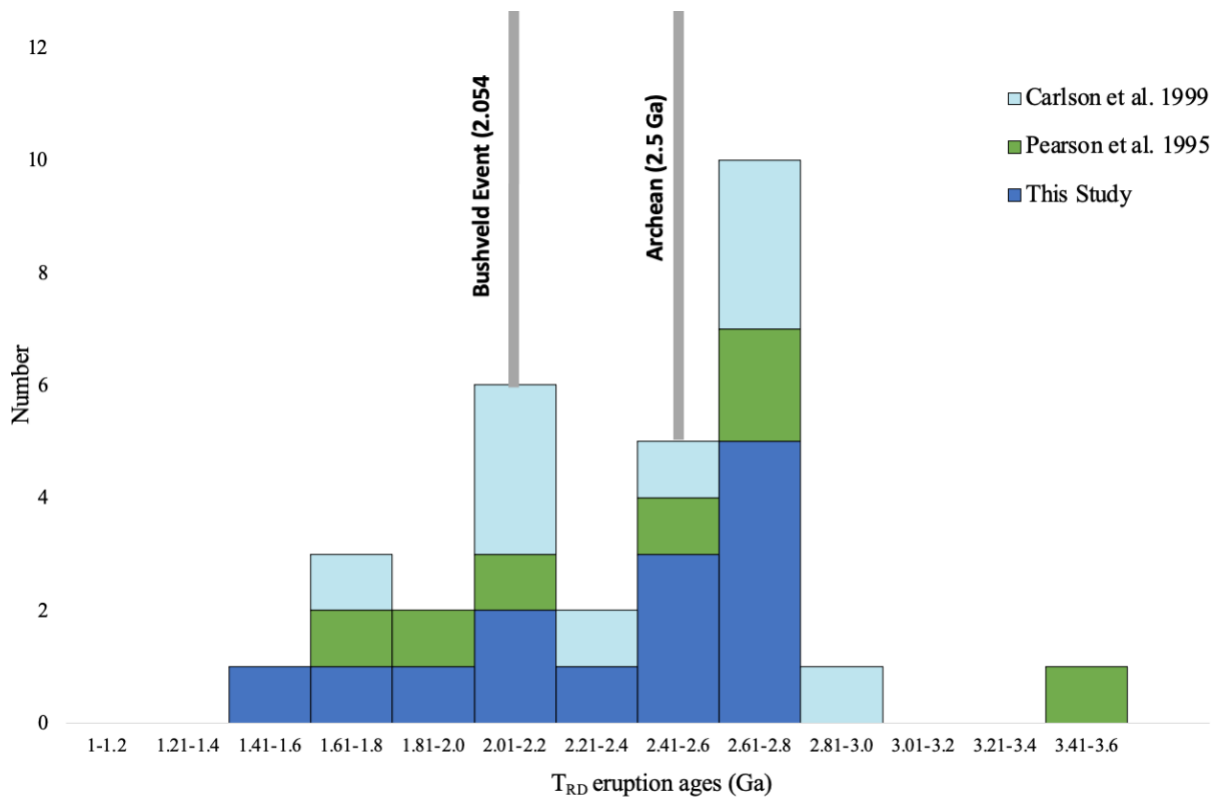
Figure 21: Stacked bar graph of T_{RD} eruption ages for Cullinan kimberlites from this study as well as Carlson et al. 1999 and Pearson et al. 1995. Bulk silicate earth values used in calculations are $^{187}Os/^{188}Os$ $_{BSE}$=0.1296 and $^{187}Re/^{188}Os$ $_{BSE}$=0.4243. The Re-Os decay constant used is λ=1.67 × 10^{-11}, from Smoliar et al. 1996.

Liu et al. 2021 have argued that after lithospheric thinning, continental cratons are healed to their original thicknesses by mantle plumes. This plume driven recratonization model could explain the wide range in T_{RD} ages found in cratonic peridotites at similar locations. A baseline assumption in this argument is that T_{RD} ages in cratonic peridotites reflect their true age, due to the high abundance of Os in peridotites which makes significant alteration to the Os isotopic composition in peridotites difficult (Rudnick and Walker 2009). With our peridotites, T_{RD} eruption ages would be more appropriate to use than T_{RD}, due to the Re addition to the peridotites at the time of kimberlite eruption. The strong influence of Re addition on the model ages of the peridotites is seen in the significant differences between T_{RD} and T_{MA} ages (**Table 7**).

However, even T_{RD} eruption ages may not be accurate, as is best seen in the four samples with the lowest T_{RD} eruption ages. These range from 1538 Ma to 2155 Ma (C2129, C2134, C2118, C2121). These samples do not have Os concentrations notably different from the other peridotites, though they do have significantly higher Re concentrations (0.20 to 0.43 ppm) than the other peridotites (0.01 to 0.11 ppm) (**Figure 22**). Though elevated Re/Al values could be explained by infiltration of kimberlite (Carlson et al. 1999), if this Re was added by the kimberlite it would have already been corrected for in the T_{RD} eruption age. There would be no correlation between higher Re values and younger T_{RD} eruption age. It is therefore possible that the peridotites also experienced Re addition earlier than the kimberlite eruption, which would draw down the $^{187}Os/^{188}Os_i$ value, making the T_{RD} eruption model ages erroneously young. This is corroborated with the La/Yb versus Re/Os indications of metasomatism of the peridotites prior to entrainment (**Figure 17**).
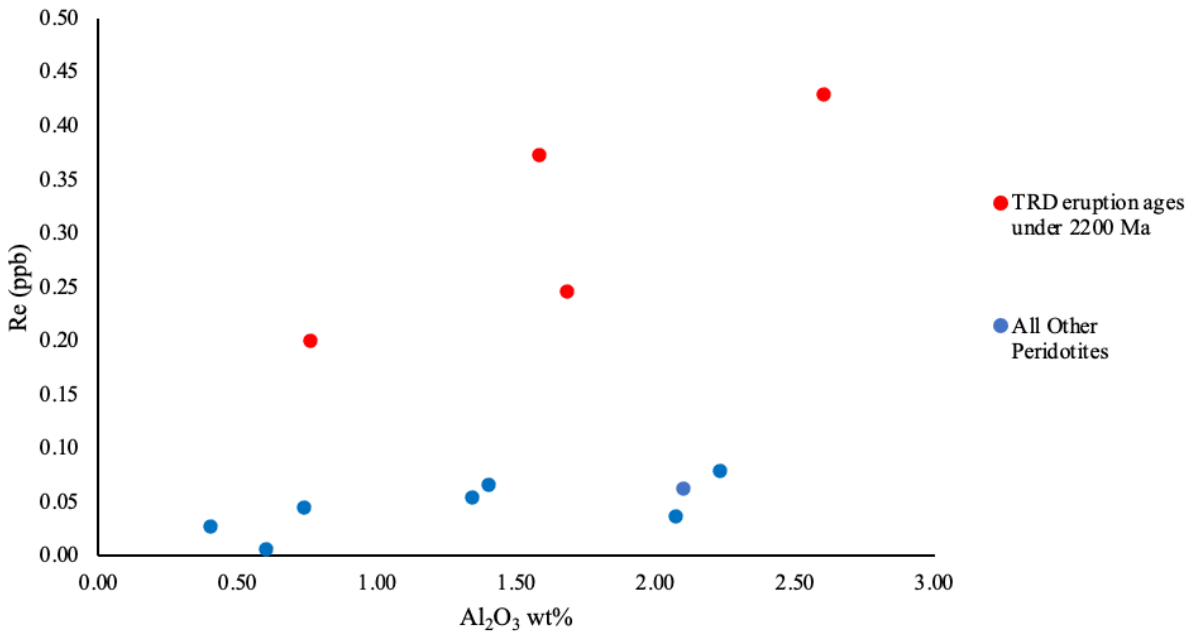
Figure 22: Al_2O_3 wt. % versus Re concentration. The four samples with T_{RD} eruption ages below 2200 Ma are in red (C2129, C2134, C2118, C2121).

Though the plume recratonization model appears to work well with Canadian kimberlites in Liu et al. 2021, applying this model to the Kaapvaal craton requires the assumption that the T_{RD} model ages of whole-rock peridotites are accurate reflections of their age, which is difficult to justify due to multi-stage melt infiltration at Cullinan.

5.5 A Note on Pyroxenite and Amphibolite Samples

The most common xenoliths at Cullinan are harzburgites, garnet harzburgites, and garnet lherzolites, though pyroxenites and eclogites are also found (Bartlett 1994). Due to their relative rarity, few studies on Cullinan pyroxenites have been conducted.

Detailed explanation of the formation conditions of these rocks are outside the scope of this study, though a likely origin for the formation of the pyroxenites is a reaction between a basaltic melt and peridotite. The extremely radiogenic Os isotopic compositions of the

48

pyroxenite and amphibolite samples in this study indicate a unique source (**Figure 23**). As one would expect for a mixture of peridotite and basaltic melt, the pyroxenites' Os isotopic compositions are intermediate between that of the peridotites and the amphibolite. The pyroxenites also have intermediate depletions in the less incompatible HSEs (Pt, Ru, Ir, Os) between peridotites and amphibolite (**Figure 15**).

Magma reaction with peridotite is a common explanation for the formation of pyroxenites and has also been suggested as the formation mechanism for pyroxenites in other South African kimberlites. Examples of this include those at Gansfontein (Doyle et al. 2004).
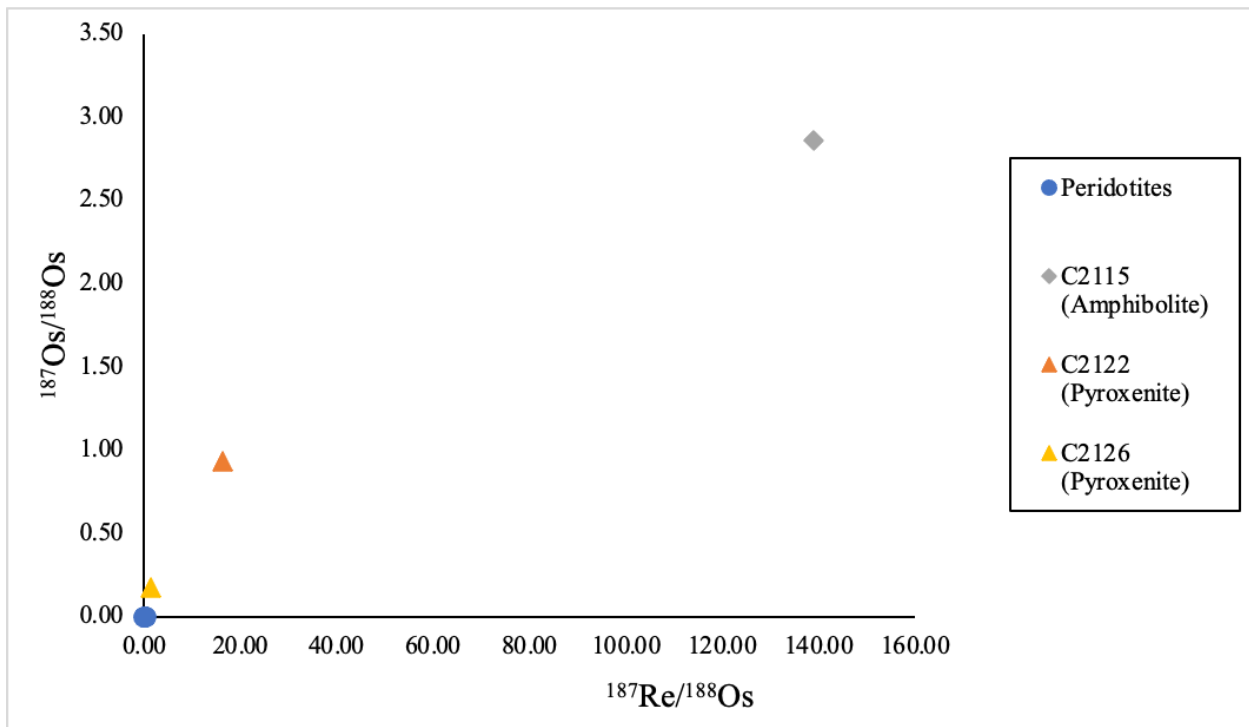
Figure 23: $^{187}Os/^{188}Os$ versus $^{187}Re/^{188}Os$ plot for peridotites, pyroxenites, and an amphibolite. Peridotites are denoted by circles, the amphibolite is denoted by a diamond, and pyroxenites are denoted by triangles.

The two studied pyroxenite samples have very different textures, mineralogies, and Osmium isotopic compositions, and appear to be distinct. As a result, an isochron will not be attempted due to the low probabilities that they are magmatically related. The amphibolite sample appears to be the most influenced by the kimberlite melt, as the trace element patterns are similar to kimberlite.

6. Conclusions

This study provides the first Re-Os isotopic data for the Cullinan kimberlite facies, and the first HSE data for most of the Cullinan kimberlite facies. The large variation in Os isotopic compositions of the different kimberlite types can be explained by variable assimilation of lithospheric peridotite. The initial $^{187}Os/^{188}Os$ composition of the kimberlite melt can be estimated as being around 0.1672, as this is the measured value of the end-member Brown kimberlite, which has the least amount of CLM assimilation. This unit has the highest diamond grade, and may experience peridotite dilution from more diamondiferous eclogite.

Estimates based on REE abundances place kimberlite melt infiltration at around 1 to 10% for most peridotites (**Figure 16**). However, Cullinan peridotites have experienced multi-stage evolution and metasomatism, making it difficult to differentiate secondary alteration by kimberlite melt from refertilization due to the Bushveld event. As a result, T_{RD} ages recording Proterozoic ages may not reflect their true ages, as Re may have been added prior to kimberlite entrainment. This raises some doubt in the validity of applying a plume-driven recratonization model to the Kaapvaal Craton. This is because it assumes that the T_{RD} ages of cratonic

peridotites are true ages, whereas the T_{RD} model ages of Cullinan peridotites may be erroneous due to potential Re addition from before the time of kimberlite entrainment.

7. Future Work

There are a few areas of future work that could be beneficial. Firstly, temperature and pressure conditions of the peridotite samples could be constrained.

Also, SEM analysis was not conducted on any of the xenolith samples. More detailed mineralogical analysis of the pyroxenites in particular would add more context to the samples. For example, the pyroxenite C2122 resembles eclogite. It would be interesting to see if the green pyroxene is omphacite.

Lastly, sampling of eclogite distribution at the Cullinan mine would be useful to confirm whether the Brown kimberlite unit assimilates the largest amount of eclogite. However, finding these xenoliths are rare at the mine in comparison to peridotite. As a result this would be a difficult task (Bartlett 1994).

8. Appendix

Table 3: Major element and trace element data for Cullinan kimberlites and calcite dikes

Specimen	C2101	C2111	C2108	C2114	C2106	C2112	C2105	C2113
Rock Type	Kimberlite	Kimberlite	Kimberlite	Kimberlite	Kimberlite	Kimberlite	Kimberlite	Kimberlite
Kimberlite Type	Brown	Brown	Grey	Grey	Grey	Grey	Blue/Brown	Fawn
Level	824 L +45	763 L	763 L	732 L	839 L	732 L	839 L	732 L
Major elements (wt%, XRF)								
SiO_2	48.5	48.1	49.6	52.3	55.3	53.4	48.7	47.4
TiO_2	1.52	1.88	1.69	1.37	1.26	0.97	1.40	1.04
Al_2O_3	4.62	4.14	5.35	4.61	4.05	3.28	3.72	3.82
Fe_2O_3T	9.76	9.22	9.75	8.62	8.54	8.80	9.16	9.54
MnO	0.14	0.13	0.15	0.18	0.10	0.12	0.14	0.11
MgO	24.9	26.2	23.0	21.8	24.6	25.9	26.2	30.4
CaO	8.38	7.24	6.50	7.32	3.13	6.05	7.80	5.97
Na_2O	0.97	1.06	1.58	2.10	1.67	0.78	1.19	1.09
K_2O	0.66	1.23	1.71	1.17	0.99	0.36	0.84	0.56
P_2O_5	0.30	0.39	0.39	0.27	0.16	0.14	0.31	0.23
Total	99.7	99.6	99.7	99.8	99.8	99.8	99.5	100.1
LOI	**8.6**	**9.1**	**7.7**	**8.0**	**7.6**	**7.1**	**9.3**	**11.4**
Total Alkalis	1.63	2.29	3.29	3.27	2.66	1.14	2.03	1.65
Trace elements (ppm, XRF)								
Rb	32	70	116	63	52	19	48	26
Sr	380	395	344	291	173	173	420	519
Zr	90	79	128	91	217	94	85	68
V	122	122	124	113	97	84	108	88
Cr	934	936	692	776	1038	645	1034	839
Ba	410	737	497	287	180	110	483	399
Trace elements (ppm, ICP-MS)								
Li	29.90	32.74	19.31	7.44	20.19	12.32	30.61	46.30
Be	1.10	1.28	1.45	1.23	0.94	0.86	0.97	1.21
B	8.84	20.71	8.45	7.19	5.80	6.53	25.74	26.69
Sc	11.16	9.00	10.36	9.38	8.76	7.16	7.95	7.06
Ti	7827	10051	9068	7359	7026	5331	7312	5548
V	106	110	112	99	86	73	87	76
Cr	932	958	716	765	1055	674	1110	896
Mn	955	925	1050	1198	766	812	968	765
Co	76	80	65	62	54	65	85	75
Ni	1097	1183	852	971	745	1139	1220	1240
Cu	54	61	49	46	49	30	85	30
Zn	70	73	63	65	77	46	78	47
Ga	6.84	6.98	7.89	6.68	6.98	4.74	6.50	5.22
Ge	1.26	1.27	1.43	1.20	1.16	1.41	1.29	1.12
Se	0.12	0.15	0.17	0.13	0.13	0.10	0.12	0.12
Rb	47	97	148	89	73	25	70	34
Sr	426	444	380	336	206	198	425	505
Y	11.74	8.23	12.38	9.63	11.71	8.42	7.78	7.81
Zr	162.97	90.11	156.27	114.87	190.23	94.83	102.57	87.87
Nb	72.55	98.71	90.39	68.06	52.85	46.34	84.58	58.10
Mo	1.08	0.93	2.93	1.19	0.36	0.42	0.82	0.20
Sn	1.117	1.040	1.311	1.056	1.171	0.953	0.969	0.823
Te	0.015	0.019	0.018	0.016	0.012	0.010	0.020	0.010
Cs	3.12	4.85	7.59	7.24	12.12	2.29	2.94	2.75
Ba	372	733	479	272	155	92	443	353
La	41.92	44.61	47.46	37.04	35.34	28.74	36.74	33.27
Ce	71.08	76.39	89.80	66.12	61.60	52.26	69.03	58.29
Pr	7.90	8.77	10.49	7.40	7.19	6.00	8.03	6.58
Nd	28.17	30.04	37.69	26.57	25.57	21.72	28.90	23.79
Sm	4.58	4.58	6.09	4.27	4.24	3.42	4.43	3.77
Eu	1.30	1.35	1.64	1.22	1.07	1.02	1.20	1.05
Gd	4.26	3.97	5.45	3.87	3.86	3.03	3.85	3.43
Tb	0.49	0.43	0.59	0.44	0.47	0.34	0.42	0.38
Dy	2.47	1.92	2.88	2.14	2.45	1.78	1.91	1.85
Ho	0.45	0.33	0.50	0.39	0.46	0.34	0.33	0.32
Er	1.25	0.88	1.34	1.04	1.33	0.96	0.87	0.88
Tm	0.16	0.11	0.17	0.14	0.19	0.13	0.11	0.12
Yb	1.02	0.67	1.05	0.87	1.25	0.87	0.67	0.71
Lu	0.15	0.09	0.15	0.12	0.19	0.13	0.10	0.11
Hf	4.21	2.23	3.83	2.86	4.75	2.42	2.63	2.22
Ta	4.55	6.18	5.81	4.20	3.71	3.19	5.12	3.78
W	0.87	1.26	2.76	2.37	1.04	1.28	1.45	0.89
Tl	0.57	2.26	0.37	0.22	0.26	0.08	0.08	0.11
Pb	9.98	10.17	6.04	25.08	7.48	5.87	20.21	4.58
Th	7.06	7.04	9.23	6.86	7.89	5.68	6.87	5.94
U	1.67	1.37	2.01	1.51	1.94	1.30	1.49	1.39

Table 3 (cont).

Specimen	C2103	C2104	C2102	C2133	C2130	895RAW	C2110	C2109
Rock Type	Kimberlite	Kimberlite	Kimberlite	Kimberlite	Kimberlite		Calcite Dike	Calcite Dike
Kimberlite	Dark	Pale Piebald	Black			N/A	N/A	N/A
Level	839 L	839 L	839 L			839 L	763 L	763 L
Major elements (wt%, XRF)								
SiO$_2$	45.0	42.7	37.5	41.3	41.74	48.6	36.6	28.0
TiO$_2$	2.03	1.80	2.41	2.66	3.42	4.36	2.68	2.20
Al$_2$O$_3$	4.20	3.49	3.07	2.82	2.65	9.66	7.65	1.30
Fe$_2$O$_3$T	8.98	9.16	10.6	11.8	12.85	10.5	11.5	16.9
MnO	0.15	0.14	0.17	0.27	0.28	0.15	0.83	0.51
MgO	27.9	27.4	30.6	33.2	34.17	10.1	35.2	23.7
CaO	7.13	13.4	13.2	5.27	3.10	8.97	4.06	24.7
Na$_2$O	0.271	0.127	0.095	0.19	0.308	1.50	0.122	0.172
K$_2$O	3.86	1.22	1.17	1.73	0.713	5.38	0.022	0.026
P$_2$O$_5$	0.092	0.16	0.45	0.30	0.202	0.57	1.14	1.15
Total	99.7	99.5	99.2	99.5	99.43	99.7	99.7	98.7
LOI	**7.0**	**8.2**	**13.4**	**10.5**	**10.81**	**2.3**	**13.0**	**22.2**
Total Alkalis	4.13	1.35	1.27	1.92	1.02	6.88	0.14	0.20
Trace elements (ppm, XRF)								
Rb	247	97	57	121	51	194	<2	10
Sr	420	183	615	382	162	535	350	5486
Zr	83	97	105	58	60	257	272	65
V	160	82	121	122	142	360	224	177
Cr	1205	1186	1253	1326	1656	<2	50	55
Ba	1577	1388	1336	1054	505	2522	143	4002
Trace elements (ppm, ICP-MS)								
Li	29.10	6.10	4.39	26.98	17.77	7.51	69.74	28.05
Be	1.37	2.36	1.03	1.59	0.79	1.96	2.76	0.49
B	23.31	31.49	44.30	36.38	32.24	9.34	50.53	66.44
Sc	10.91	10.07	10.38	11.58	10.82	26.94	0.21	32.51
Ti	11657	10293	13109	14510	17958	25991	13578	9866
V	160	75	104	107	116	355	193	129
Cr	1265	1225	1259	1268	1503	1	82	82
Mn	1111	1040	1158	1880	1937	1146	5353	2938
Co	81	76	69	91	95	45	36	58
Ni	1277	1175	1107	1314	1383	42	102	162
Cu	24	40	78	81	79	185	53	104
Zn	69	55	69	91	131	79	51	70
Ga	7.17	6.84	7.11	7.00	6.73	16.12	15.44	6.18
Ge	1.18	1.51	1.43	1.62	1.70	2.46	2.61	2.38
Se	0.15	0.20	0.18	0.18	0.17	0.38	0.40	0.31
Rb	350	133	71	184	77	275	3	3
Sr	497	222	698	473	209	649	406	5736
Y	10.00	9.45	10.51	7.15	8.64	26.38	22.43	16.47
Zr	105.97	114.02	129.32	79.05	70.35	358.06	332.98	331.43
Nb	83.54	120.03	140.41	121.83	134.25	92.81	337.54	195.53
Mo	0.20	0.61	0.45	0.75	2.00	1.86	0.76	0.66
Sn	0.845	0.715	1.404	1.075	1.029	2.409	3.168	3.485
Te	0.017	0.016	0.022	0.021	0.019	0.027	0.044	0.047
Cs	7.83	1.92	1.57	7.42	6.31	11.09	1.43	2.24
Ba	1662	1396	1263	1058	498	2665	130	3329
La	39.97	78.86	59.18	55.88	59.76	75.59	137.54	112.88
Ce	66.53	118.08	100.18	96.22	105.16	161.45	269.45	198.11
Pr	7.20	13.22	11.97	10.48	12.54	21.75	32.34	22.37
Nd	25.48	43.06	41.27	38.00	41.45	83.11	116.47	79.17
Sm	4.10	6.42	6.13	5.78	6.44	13.16	16.60	10.95
Eu	1.32	2.01	1.80	1.81	1.90	4.66	4.47	3.41
Gd	3.84	5.64	5.22	5.08	5.55	11.21	14.41	9.44
Tb	0.43	0.55	0.54	0.51	0.56	1.26	1.43	0.88
Dy	2.13	2.31	2.46	2.13	2.40	5.97	6.21	3.50
Ho	0.38	0.37	0.41	0.33	0.38	1.00	1.01	0.53
Er	1.05	0.99	1.06	0.77	0.94	2.59	2.58	1.30
Tm	0.13	0.12	0.12	0.08	0.10	0.31	0.29	0.14
Yb	0.80	0.74	0.74	0.46	0.58	1.84	1.69	0.85
Lu	0.11	0.10	0.10	0.06	0.08	0.25	0.23	0.12
Hf	2.68	2.82	3.34	2.21	1.99	8.35	7.60	6.82
Ta	6.52	5.66	9.77	8.46	10.51	5.05	10.84	18.11
W	0.94	2.67	1.53	13.02	1.16	2.32	2.53	2.24
Tl	0.11	0.09	0.12	1.02	0.35	0.58	0.03	0.02
Pb	2.00	2.47	5.67	5.78	2.41	3.29	16.04	5.84
Th	5.78	5.86	6.13	8.15	8.65	6.82	11.29	83.70
U	1.86	2.06	2.12	1.45	1.54	1.99	5.09	4.43

Table 4: Major element and trace element data for Cullinan xenoliths

Specimen	C2117	C2118	C2119	C2120	C2121	C2123	C2124	C2125	C2127	C2128
Rock Type	Xenolith	Xenolith	Xenolith	Xenolith	Xenolith	Xenolith	Xenolith	Xenolith	Xenolith	Xenolith
Xenolith Type	Sheared Lherzolite	Lherzolite	Lherzolite	Garnet Lherzolite	Garnet Lherzolite	Garnet Lherzolite	Altered Garnet Lherzolite	Harzburgite	Harzburgite	Harzburgite
Source										
Major elements (wt%, XRF)										
SiO_2	44.83	45.88	44.05	43.76	44.03	46.66	41.01	43.96	44.63	46.32
TiO_2	0.21	0.02	0.05	0.26	0.07	0.17	0.58	0.01	0.16	0.03
Al_2O_3	1.34	1.58	0.40	1.56	1.68	2.80	2.23	0.49	0.60	2.10
Fe_2O_3	7.90	7.24	7.04	8.69	8.17	8.28	11.95	6.89	7.57	7.15
MnO	0.09	0.08	0.06	0.11	0.09	0.13	0.13	0.06	0.08	0.09
MgO	41.75	44.03	47.33	43.58	41.89	37.17	37.31	47.76	45.66	43.36
CaO	2.61	0.75	0.48	1.50	3.13	3.37	3.99	0.07	0.23	0.44
Na_2O	0.231	0.103	0.112	0.177	0.245	0.390	0.11	0.067	0.075	0.100
K_2O	0.610	0.089	0.027	0.103	0.072	0.195	2.02	0.038	0.041	0.120
P_2O_5	0.028	0.016	0.012	0.023	0.021	0.024	0.30	0.008	0.018	0.008
Total	99.60	99.78	99.56	99.75	99.40	99.19	99.63	99.35	99.06	99.72
LOI	9.59	7.02	9.29	7.94	6.68	8.10	5.93	8.66	6.84	5.83
Total Alkalis	0.84	0.19	0.14	0.28	0.32	0.59	2.13	0.11	0.12	0.22
Trace elements (ppm, XRF)										
Rb	38	4	<2	4	<2	9	134	<2	<2	5
Sr	71	25	11	30	34	68	211	12	8	16
Zr	31	9	10	12	9	11	15	8	10	9
V	58	40	27	42	54	72	132	12	28	31
Cr	2438	2705	2726	2372	3560	3343	937	1211	1527	2617
Ba	164	85	49	109	107	194	763	47	49	83
Trace elements (ppm, ICP-MS)										
Li	13.11	0.86	0.63	1.13	0.73	7.82	3.49	0.35	0.25	0.80
Be	0.35	0.05	0.09	0.07	0.06	0.12	0.89	0.03	0.04	0.04
B	52.79	56.49	78.69	25.89	46.04	18.01	7.52	72.38	71.29	37.24
Sc	7.43	4.21	1.76	6.59	7.00	6.96	7.89	1.81	2.07	4.63
Ti	1130	90	255	952	333	998	3309	76	143	145
V	51	34	15	38	52	68	123	13	15	27
Cr	2413	2635	2378	2427	3448	3257	944	1184	1388	2594
Mn	616	515	417	682	568	801	911	384	465	590
Co	91	91	99	106	98	98	100	102	101	89
Ni	2081	2272	2476	2334	2285	2189	974	2541	2349	2134
Cu	15	6	5	7	17	24	74	1	2.8	1
Zn	31	28	21	31	24	41	61	18	20	33
Ga	1.94	0.60	0.32	1.13	1.32	2.95	8.16	0.25	0.37	1.56
Ge	0.82	0.70	0.69	0.83	0.82	0.87	0.99	0.74	0.73	0.70
Se	0.05	0.02	0.03	0.04	0.03	0.04	0.02	0.03	0.04	0.02
Rb	57	7	3	4	5	15	196	3	1	9
Sr	76.13	27.94	14.82	22.96	38.70	77.81	255	16.06	5.81	19.32
Y	1.15	0.23	0.24	1.25	0.61	2.11	0.98	0.12	0.15	0.78
Zr	28.80	2.38	3.16	6.26	3.37	8.73	14.13	1.13	1.54	2.64
Nb	5.47	5.17	1.39	1.06	2.90	4.64	12.79	1.54	1.90	0.78
Mo	0.49	0.23	0.87	0.70	0.48	0.50	0.32	1.51	0.32	0.22
Sn	0.407	0.064	0.102	0.094	0.049	0.225	0.405	0.023	0.021	0.055
Te	0.008	0.002	0.001	0.002	0.002	0.004	0.007	0.002	0.002	0.002
Cs	2.79	0.85	0.15	0.38	0.35	2.74	2.26	0.29	0.12	1.50
Ba	127	48	21	53	74	162	729	29	8	50
La	3.60	1.58	0.69	0.60	1.70	4.99	2.16	0.67	0.88	0.52
Ce	6.18	2.76	1.22	1.20	3.25	7.40	3.29	1.19	1.41	0.87
Pr	0.84	0.35	0.16	0.17	0.44	0.89	0.44	0.15	0.17	0.10
Nd	3.52	1.32	0.66	0.79	1.79	3.39	1.83	0.54	0.60	0.38
Sm	0.76	0.21	0.13	0.22	0.32	0.66	0.38	0.09	0.09	0.08
Eu	0.27	0.07	0.04	0.09	0.10	0.33	0.24	0.03	0.03	0.04
Gd	0.65	0.17	0.12	0.29	0.26	0.62	0.35	0.07	0.08	0.12
Tb	0.08	0.02	0.01	0.05	0.03	0.08	0.04	0.01	0.01	0.02
Dy	0.36	0.06	0.06	0.28	0.15	0.43	0.22	0.03	0.04	0.15
Ho	0.05	0.01	0.01	0.05	0.03	0.09	0.04	0.00	0.01	0.03
Er	0.12	0.03	0.02	0.13	0.07	0.25	0.11	0.01	0.01	0.09
Tm	0.01	0.00	0.00	0.02	0.01	0.04	0.01	0.00	0.00	0.01
Yb	0.07	0.02	0.02	0.09	0.07	0.23	0.09	0.01	0.01	0.09
Lu	0.01	0.00	0.00	0.01	0.01	0.04	0.01	0.00	0.00	0.01
Hf	1.21	0.06	0.13	0.19	0.10	0.26	0.86	0.03	0.04	0.08
Ta	0.40	0.20	0.07	0.07	0.17	0.30	1.26	0.07	0.09	0.02
W	0.53	0.26	0.42	0.67	0.57	0.10	0.32	0.47	0.19	0.14
Tl	0.69	0.75	0.09	0.42	0.62	1.03	0.15	0.05	0.16	0.05
Pb	2.14	0.75	0.28	0.74	0.61	0.96	1.75	0.20	0.34	0.26
Th	0.17	0.06	0.04	0.04	0.13	0.26	0.15	0.03	0.04	0.03
U	0.05	0.04	0.02	0.01	0.05	0.07	0.05	0.02	0.02	0.02

Table 4 (cont.)

Specimen	C2129	C2116	C2131	C2132	C2134	C2115	C2122	C2126	FRB 1350
Rock Type	Xenolith	Xenolith	Xenolith	Xenolith	Xenolith	Xenolith	Xenolith	Xenolith	Xenolith
Xenolith Type	Harzburgite	Harzburgitew/ Phlogopite vein	Garnet Harzburgite	Garnet Harzburgite	Garnet Lherzolite	Amphibolite	Pyroxenite	Pyroxenite	Garnet Spinel Lherzolite
Source									*Pearson and Nowell 2002*
Major elements (wt%, XRF)									
SiO_2	43.17	46.40	44.59	43.12	46.02	45.55	45.89	49.26	
TiO_2	0.05	2.34	0.26	0.06	0.27	4.64	0.21	0.11	
Al_2O_3	0.76	2.07	1.40	0.74	2.60	10.16	13.69	6.79	
Fe_2O_3	7.78	7.40	8.02	8.15	7.79	14.70	7.71	9.65	
MnO	0.06	0.13	0.10	0.05	0.18	0.34	0.24	0.14	
MgO	47.00	37.54	44.33	47.24	38.24	9.59	23.68	25.95	
CaO	0.43	1.63	0.82	0.23	3.56	9.35	5.49	4.85	
Na_2O	0.085	0.274	0.183	0.083	0.310	3.80	0.472	0.67	
K_2O	0.069	1.350	0.116	0.022	0.317	0.87	1.150	2.335	
P_2O_5	0.022	0.040	0.025	0.014	0.056	0.58	0.025	0.014	
Total	99.43	99.17	99.84	99.71	99.34	99.58	98.56	99.77	
LOI	**8.40**	**7.33**	5.47	11.61	12.13	1.01	1.71	4.27	
Total Alkalis	0.15	1.62	0.30	0.11	0.63	4.67	1.62	3.01	
Trace elements (ppm, XRF)									
Rb	<2	90	5	<2	12	18	50	121	
Sr	14	71	33	4	72	284	231	84	
Zr	9	43	15	9	12	251	10	9	
V	38	107	45	26	82	386	135	95	
Cr	3185	3699	2371	2139	2057	<2	3400	4626	
Ba	79	219	103	49	450	473	5939	233	
Trace elements (ppm, ICP-MS)									
Li	0.37	14.59	5.86	0.27	4.77	4.77	15.85	26.99	
Be	0.06	0.26	0.14	0.05	0.23	2.23	0.10	1.22	
B	80.68	26.80	38.87	130.76	94.06	1.75	2.91	7.14	
Sc	1.41	7.93	6.99	2.95	6.34	20.61	52.02	8.80	
Ti	272	14796	1536	284	1463	26193	1276	602	90.0
V	32	97	40	19	68	356	134	92	
Cr	3115	3216	2475	2034	1957	2	3350	4437	
Mn	392	960	685	352	1201	2463	1660	937	
Co	104	76	107	103	98	52	52	92	
Ni	2653	1567	2463	2497	2750	18	622	1396	
Cu	26	14	8	3	7	25	57	123	
Zn	32	41	32	19	221	134	24	79	
Ga	0.79	5.25	1.64	0.51	3.82	16.46	4.78	5.89	
Ge	0.73	0.90	0.79	0.76	0.73	2.52	1.03	0.95	
Se	0.03	0.03	0.03	0.04	0.04	0.38	0.07	0.03	
Rb	5	158	11	2	17	27	76	147	
Sr	17.19	88.08	39.74	7.54	77.74	380	308	94.37	20.3
Y	0.31	0.93	1.41	0.32	2.32	27.71	6.19	3.53	
Zr	3.45	50.80	8.76	3.22	8.85	359.37	12.20	4.39	0.061
Nb	4.72	301.45	4.12	1.70	2.72	119.14	7.26	1.58	1.37
Mo	0.28	0.39	0.16	4.52	0.62	2.18	1.66	0.66	
Sn	0.074	0.487	0.125	0.073	0.208	2.897	0.145	0.304	
Te	0.002	0.037	0.002	0.002	0.002	0.021	0.008	0.036	
Cs	0.23	8.26	1.17	0.11	0.60	1.27	5.87	8.11	
Ba	40	271	67	24	410	522	6606	217	162
La	1.98	5.79	2.71	0.82	1.86	83.71	3.36	1.09	1.17
Ce	3.44	9.90	3.99	1.33	3.02	177.75	6.50	1.28	2.00
Pr	0.42	1.19	0.45	0.16	0.38	24.13	0.90	0.15	
Nd	1.54	4.31	1.62	0.62	1.51	91.96	3.69	0.64	0.890
Sm	0.24	0.69	0.30	0.13	0.36	14.05	0.90	0.19	0.145
Eu	0.07	0.24	0.14	0.05	0.21	4.03	1.49	0.14	
Gd	0.20	0.59	0.35	0.13	0.42	12.02	1.16	0.31	0.129
Tb	0.02	0.06	0.05	0.02	0.07	1.35	0.18	0.07	
Dy	0.09	0.24	0.30	0.08	0.45	6.37	1.18	0.56	0.096
Ho	0.01	0.04	0.06	0.01	0.09	1.08	0.25	0.14	0.017
Er	0.03	0.09	0.15	0.03	0.26	2.83	0.76	0.46	
Tm	0.00	0.01	0.02	0.00	0.04	0.34	0.11	0.08	
Yb	0.02	0.05	0.11	0.03	0.24	2.05	0.77	0.53	0.065
Lu	0.00	0.01	0.02	0.00	0.04	0.29	0.12	0.08	0.012
Hf	0.09	1.79	0.26	0.08	0.27	8.71	0.30	0.16	0
Ta	0.22	42.57	0.27	0.08	0.17	6.99	0.50	0.23	
W	0.15	0.46	0.13	0.95	0.39	2.14	1.09	0.25	
Tl	1.07	1.12	0.14	0.11	0.36	0.13	0.19	0.36	
Pb	2.68	0.86	0.37	0.31	56.76	5.77	2.97	1.60	
Th	0.09	1.24	0.28	0.05	0.20	7.54	0.29	0.08	
U	0.05	0.17	0.06	0.02	0.04	1.67	0.08	0.14	

Table 5: Trace element standards

	TAB (n=2)	BHVO-2 (n=8)	St Dev	RSD	BCR-2 (n=4)	St Dev	RSD	BIR-1a (n=4)	St Dev	RSD	HARZ-01 (n=2)	St Dev	RSD
Li	0.0016	4.80	0.12	2%	10.29	0.15	1%	3.41	0.04	1%	0.20	0.01	3%
Be	0.0056	1.07	0.07	6%	2.30	0.07	3%	0.09	0.00	1%	B.D.L	0.00	N/A
B	0.3893	2.95	0.13	4%	4.94	0.13	3%	0.31	0.04	12%	5.22	0.25	5%
Sc	1.1926	32.00	1.88	6%	37.66	1.03	3%	44.11	2.30	5%	3.14	0.14	4%
Ti	0.6715	16300.00	492.10	3%	13580.85	438.12	3%	5699.21	232.51	4%	11.53	2.50	22%
V	0.5393	317.00	7.10	2%	420.84	9.61	2%	325.07	10.25	3%	29.52	0.50	2%
Cr	1.9649	280.00	11.47	4%	13.58	0.27	2%	367.71	10.82	3%	2917.51	69.47	2%
Mn	0.0560	1270.00	29.60	2%	1519.14	40.45	3%	1304.87	34.95	3%	776.53	22.13	3%
Co	0.0992	45.00	0.86	2%	38.44	1.04	3%	53.38	1.08	2%	113.07	2.98	3%
Ni	1.9539	119.00	2.95	2%	12.46	0.37	3%	173.26	2.77	2%	2653.67	63.35	2%
Cu	0.4105	127.00	4.26	3%	19.06	0.40	2%	118.36	4.32	4%	4.02	0.21	5%
Zn	0.5547	103.00	5.72	6%	132.20	8.12	6%	64.52	0.85	1%	49.42	1.07	2%
Ga	0.0013	22.00	0.27	1%	23.30	0.15	1%	15.60	0.24	2%	0.45	0.01	1%
Ge	0.0023	1.60	0.03	2%	1.79	0.03	2%	1.16	0.00	0%	0.87	0.00	0%
Se	0.0693	0.18	0.01	6%	0.20	0.01	3%	0.05	0.01	23%	0.02	0.02	76%
Rb	0.0022	9.11	0.57	6%	60.64	1.91	3%	0.20	0.04	19%	0.03	0.01	31%
Sr	0.0728	396.00	11.26	3%	370.42	3.75	1%	103.16	1.58	2%	0.16	0.03	18%
Y	0.0006	26.00	0.46	2%	37.05	0.36	1%	14.12	0.01	0%	0.02	0.00	19%
Zr	0.0195	172.00	1.95	1%	190.29	2.15	1%	13.30	0.10	1%	0.99	0.17	17%
Nb	0.0031	18.10	0.79	4%	11.98	0.20	2%	0.53	0.03	5%	0.01	0.00	15%
Mo	0.0192	4.20	0.46	11%	306.46	13.81	5%	0.45	0.01	3%	0.40	0.00	1%
Sn	0.0402	1.70	0.01	0%	2.15	0.03	2%	0.74	0.01	1%	0.07	0.00	3%
Te	0.0002	0.01	0.00	7%	0.01	0.00	20%	0.00	0.00	43%	0.00	0.00	27%
Cs	0.0001	0.10	0.02	16%	1.97	0.04	2%	0.01	0.00	7%	0.09	0.00	4%
Ba	0.3599	131.00	4.39	3%	714.65	4.31	1%	6.39	0.07	1%	0.23	0.23	101%
La	0.0010	15.20	0.51	3%	26.16	0.21	1%	0.59	0.00	0%	0.03	0.01	28%
Ce	0.0021	37.50	0.19	1%	52.88	0.56	1%	1.78	0.02	1%	0.40	0.02	5%
Pr	0.0003	5.35	0.05	1%	6.83	0.07	1%	0.38	0.00	0%	2.61	0.03	1%
Nd	0.0013	24.50	0.18	1%	28.81	0.32	1%	2.38	0.05	2%	0.18	0.01	4%
Sm	0.0004	6.07	0.12	2%	6.63	0.14	2%	1.10	0.01	1%	0.00	0.00	68%
Eu	0.0001	2.07	0.05	2%	2.08	0.03	2%	0.52	0.01	1%	0.00	0.00	119%
Gd	0.0002	6.24	0.11	2%	6.97	0.08	1%	1.73	0.04	2%	0.23	0.00	1%
Tb	0.0000	0.92	0.02	2%	1.05	0.02	2%	0.35	0.00	1%	0.00	0.00	52%
Dy	0.0002	5.31	0.12	2%	6.48	0.15	2%	2.57	0.03	1%	0.00	0.00	77%
Ho	0.0000	0.98	0.02	2%	1.30	0.04	3%	0.57	0.01	1%	0.00	0.00	49%
Er	0.0001	2.54	0.05	2%	3.72	0.07	2%	1.66	0.04	3%	0.19	0.00	2%
Tm	0.0000	0.33	0.01	3%	0.53	0.01	2%	0.25	0.00	1%	0.01	0.00	19%
Yb	0.0001	2.00	0.05	2%	3.40	0.11	3%	1.64	0.07	4%	0.01	0.00	8%
Lu	0.0000	0.27	0.01	3%	0.50	0.02	3%	0.24	0.01	3%	0.00	0.00	3%
Hf	0.0005	4.36	0.10	2%	4.82	0.12	3%	0.58	0.02	3%	0.03	0.00	10%
Ta	0.0006	1.14	0.01	1%	0.77	0.02	2%	0.04	0.00	7%	0.01	0.00	33%
W	0.0093	0.25	0.00	2%	0.54	0.02	3%	0.03	0.00	11%	7.12	0.26	4%
Tl	0.0007	0.02	0.00	3%	0.31	0.01	2%	0.00	0.00	8%	0.00	0.00	5%
Pb	0.0172	1.60	0.04	2%	11.42	0.44	4%	3.19	0.08	3%	226.66	3.98	2%
Th	0.0002	1.22	0.03	2%	6.05	0.22	4%	0.03	0.01	19%	0.00	0.00	72%
U	0.0001	0.40	0.02	4%	1.62	0.06	4%	0.01	0.00	9%	0.00	0.00	9%

Table 6: Highly siderophile element abundances (in ng/g) and Re–Os isotopic ratios for Cullinan kimberlites

Sample	Kimberlite Type	Re	Pd	Pt	Ru	Ir	Os
C2102	Black Coherent	0.09	5.95	2.15	2.54	1.09	1.97
C2103	Dark Piebald	0.32	2.12	2.02	2.81	0.52	1.29
C2104	Pale Piebald	0.09	1.38	1.74	1.91	0.50	1.08
C2111	Brown	0.19	4.72	3.12	1.10	0.23	0.52
C2113	Fawn	0.11	5.29	3.54	1.25	1.02	0.68
C2114	Grey	0.27	10.12	3.38	1.63	0.75	0.92
C2105	Blue/Brown Transitional	0.29	15.15	2.06	1.87	0.83	1.09
C2133		0.14	3.58	2.07	3.25	1.98	2.45

Sample	Kimberlite Type	$^{187}Re/^{188}Os$	2SE	$^{187}Os/^{188}Os$	2SE	γOs
C2102	Black Coherent	0.227	0.003	0.12251	0.00008	-1.5
C2103	Dark Piebald	1.189	0.018	0.14786	0.00013	4.3
C2104	Pale Piebald	0.391	0.006	0.12684	0.00010	-0.5
C2111	Brown	1.777	0.027	0.16715	0.00135	10.9
C2113	Fawn	0.763	0.011	0.15548	0.00015	17.4
C2114	Grey	1.420	0.021	0.15842	0.00015	9.4
C2105	Blue/Brown Transitional	1.269	0.019	0.14689	0.00011	2.2
C2133		0.2763	0.0041	0.12226	0.00008	-2.5

Table 7: Highly siderophile element abundances (in ng/g) and Re-Os isotopic ratios for Cullinan mantle xenoliths

Sample	Xenolith Type	Re	Pd	Pt	Ru	Ir	Os
C2122	Pyroxenite	0.563	4.33	4.46	0.39	0.18	0.18
C2115	Amphibolite	0.612	8.33	0.07	0.02	0.06	0.03
C2126	Pyroxenite	0.395	6.51	6.56	5.18	0.94	1.36
C2116	Harzburgite w/Phlogopite Veins	0.037	0.04	1.19	3.58	3.86	5.21
C2131	Garnet Harzburgite	0.066	1.31	4.30	8.47	5.03	7.34
C2129	Harzburgite	0.201	14.25	16.67	13.92	8.03	11.21
C2127	Harzburgite	0.007	0.21	2.99	9.21	6.39	6.94
C2128	Harzburgite	0.063	0.95	0.96	5.07	1.30	1.29
C2134	Garnet Lherzolite	0.429	0.43	2.48	5.55	3.55	4.25
C2118	Lherzolite	0.373	3.97	8.19	9.94	6.27	9.03
C2132	Garnet Harzburgite	0.046	0.83	2.77	7.25	4.95	5.75
C2119	Lherzolite	0.028	1.35	2.20	11.18	8.88	11.70
C2124	Altered Garnet Lherzolite	0.079	5.38	5.33	5.65	3.40	6.29
C2121	Garnet Lherzolite	0.247	4.23	4.70	5.00	2.85	3.93
C2117	Sheared Lherzolite	0.054	3.84	7.62	8.94	5.70	8.40
FRB 1350	Garnet Spinel Lherzolite	0.107	1.44	5.49	6.60	4.66	5.60
	Pearson et al. 1995	*0.026*	-	-	-	-	*3.39*
FRB 921	Garnet Lherzolite or Harzburgite	0.110	2.39	3.53	6.58	2.66	3.24
	Pearson et al. 1995	*0.053*	-	-	-	-	*2.66*

Table 7 (cont.): Highly siderophile element abundances (in ng/g) and Re-Os isotopic ratios for Cullinan mantle xenoliths

Sample	Xenolith Type	$^{187}Re/^{188}Os$	2SE	$^{187}Os/^{188}Os$	2SE	γOs	T_{RD} erupt (Ma)	T_{RD} (Ma)	T_{MA} (Ma)
C2122	Pyroxenite	16.3	0.2	0.9376	0.0015	421.0	N/A	N/A	N/A
C2115	Amphibolite	139	2	2.861	0.088	62.3	N/A	N/A	N/A
C2126	Pyroxenite	1.4027	0.0210	0.17959	0.00013	27.3	N/A	N/A	N/A
C2116	Harzburgite w/Phlogopite Veins	0.0344	0.0005	0.11132	0.00006	-7.7	2621	2532	2750
C2131	Garnet Harzburgite	0.0436	0.0007	0.11112	0.00008	-8.1	2672	2559	2845
C2129	Harzburgite	0.0862	0.0013	0.11873	0.00008	-2.4	1746	1519	1900
C2127	Harzburgite	0.0045	0.0001	0.10956	0.00008	-8.7	2781	2770	2799
C2128	Harzburgite	0.2369	0.0036	0.11644	0.00012	-6.7	2453	1833	4073
C2134	Garnet Lherzolite	0.4864	0.0073	0.12342	0.00006	-4.9	2155	868	-6291
C2118	Lherzolite	0.1990	0.0030	0.11893	0.00010	-4.0	2016	1491	2778
C2132	Garnet Harzburgite	0.0382	0.0006	0.11325	0.00009	-6.2	2370	2270	2490
C2119	Lherzolite	0.0113	0.0002	0.11014	0.00007	-8.4	2721	2691	2763
C2124	Altered Garnet Lherzolite	0.0604	0.0009	0.11226	0.00010	-7.4	2562	2405	2795
C2121	Garnet Lherzolite	0.3025	0.0045	0.12439	0.00010	-1.1	1538	733	2516
C2117	Sheared Lherzolite	0.0310	0.0005	0.11055	0.00006	-8.3	2717	2637	2840
FRB 1350	Garnet Spinel Lherzolite	0.0919	0.0014	0.11332	0.00014	-7.0	2500	2261	2871
	Pearson et al. 1995	*0.0380*		*0.11370*	*0.00007*	*-5.7*	*2200*	*-*	*2300*
FRB 921	Garnet Lherzolite or Harzburgite	0.1632	0.0024	0.11838	0.00021	-3.9	1996	1567	2526
	Pearson et al. 1995	*0.0950*		*0.12139*	*0.00020*	*-0.3*	*1200*	*-*	*1200*

Table 8: Total analytical blanks

Sample	Re	Pd	Pt	Ru	Ir	Os	^{187}Os/^{188}Os	2SE
TAB 1	0.056	0.099	0.252	0.423	0.000	0.003	0.15061	0.00600
TAB 2	0.022	0.008	0.012	0.146	0.003	0.003	0.05114	0.00284
	Re blk%	Pd blk%	Pt blk%	Ru blk%	Ir blk%	Os blk %		
C2102	42.7%	0.2%	1.1%	10.2%	0.7%	0.2%		
C2103	17.8%	0.7%	1.2%	9.3%	1.4%	0.3%		
C2104	43.9%	1.0%	1.4%	13.1%	1.5%	0.4%		
C2111	26.7%	0.3%	0.8%	20.9%	3.2%	0.8%		
C2113	39.2%	0.3%	0.7%	18.9%	0.7%	0.6%		
C2114	20.2%	0.1%	0.7%	15.0%	1.0%	0.4%		
C2105	19.6%	0.1%	1.2%	13.5%	0.9%	0.4%		
C2133	23.2%	0.2%	0.7%	5.2%	0.2%	0.10%		
C2122	6.1%	0.2%	0.3%	28.1%	2.1%	1.02%		
C2115	65.8%	0.1%	18.3%	91.5%	7.6%	7.87%		
C2126	9.4%	0.1%	0.2%	3.2%	0.5%	0.17%		
C2116	53.6%	18.8%	1.3%	4.8%	0.1%	0.05%		
C2131	39.0%	0.6%	0.4%	2.1%	0.1%	0.03%		
C2129	17.4%	0.1%	0.1%	1.3%	0.1%	0.02%		
C2127	86.8%	3.9%	0.5%	1.9%	0.1%	0.04%		
C2128	40.3%	0.9%	1.6%	3.4%	0.4%	0.19%		
C2134	9.0%	1.9%	0.6%	3.1%	0.1%	0.06%		
C2118	10.2%	0.2%	0.2%	1.8%	0.1%	0.03%		
C2132	48.0%	1.0%	0.5%	2.4%	0.1%	0.04%		
C2119	61.0%	0.6%	0.7%	1.6%	0.1%	0.02%		
C2124	34.8%	0.2%	0.3%	3.0%	0.1%	0.04%		
C2121	14.2%	0.2%	0.3%	3.3%	0.2%	0.06%		
C2117	43.9%	0.2%	0.2%	2.0%	0.1%	0.03%		
FRB 1350	10.0%	0.2%	0.5%	1.0%	0.7%	0.10%		
FRB 921	10.0%	0.2%	0.5%	1.0%	0.7%	0.10%		
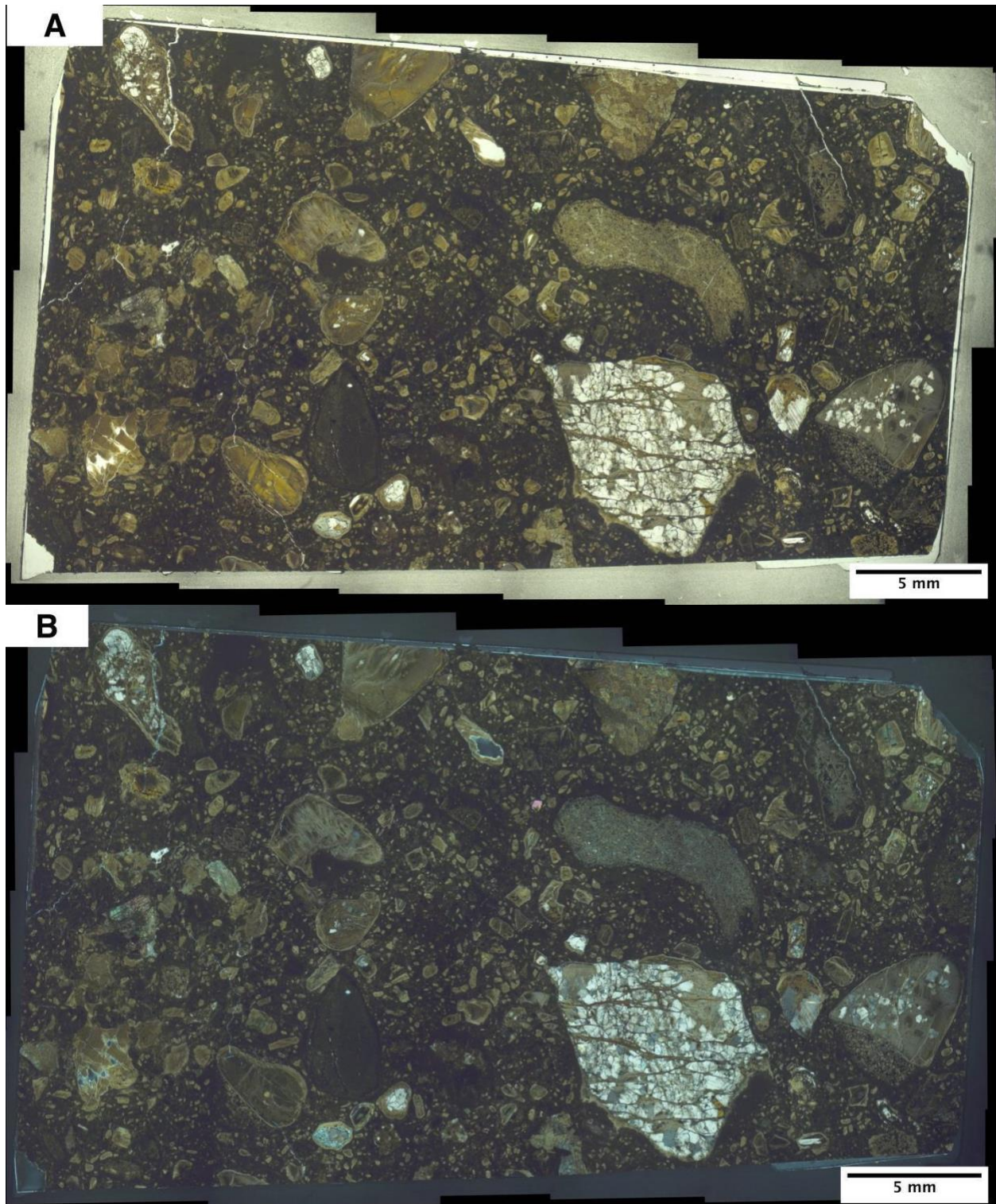
Figure S1: C2101 Brown Kimberlite imaged in a) plane polarized light and b) cross polarized light
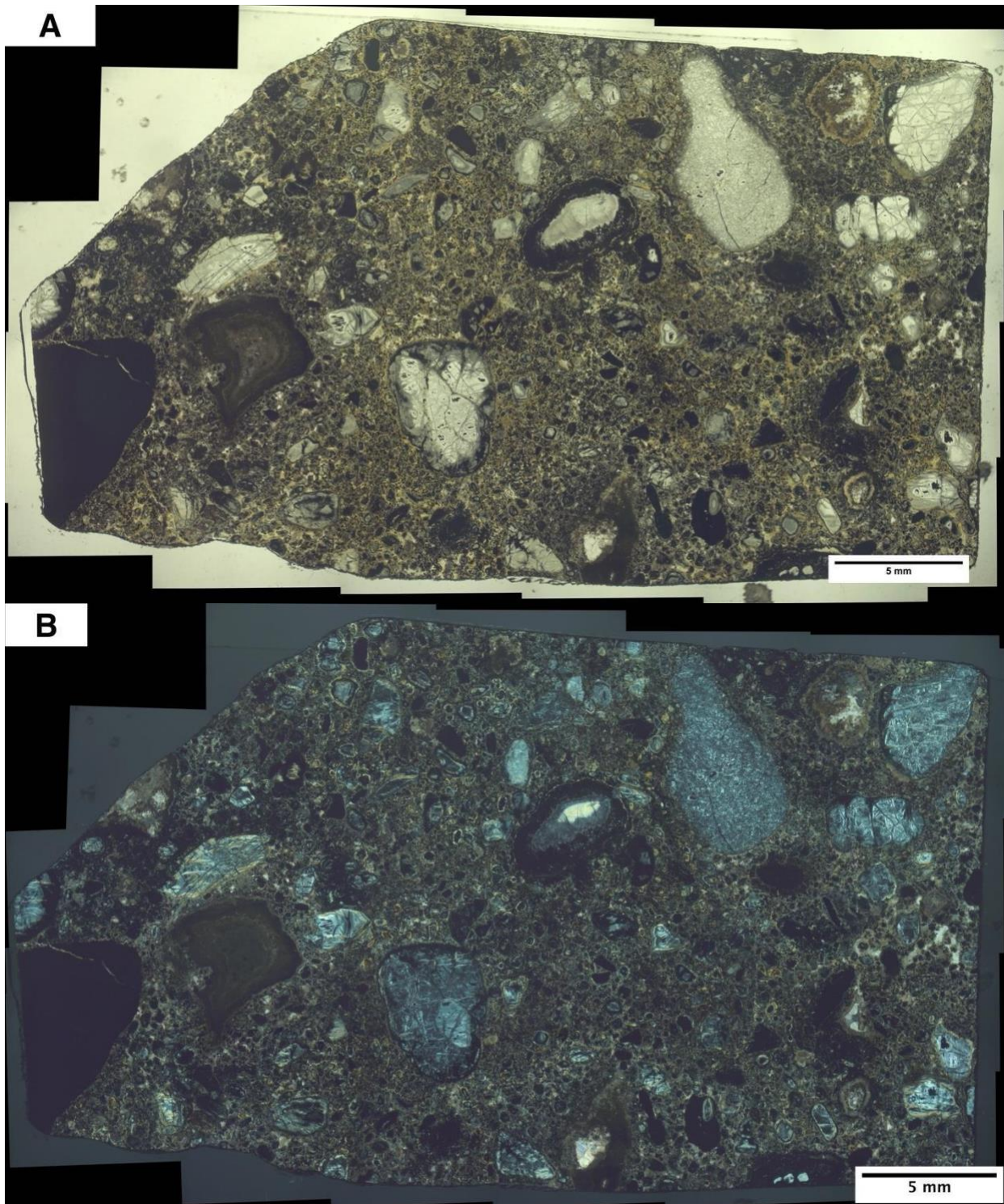
Figure S2: C2102 Black Coherent Kimberlite imaged in a) plane polarized light and b) cross polarized light
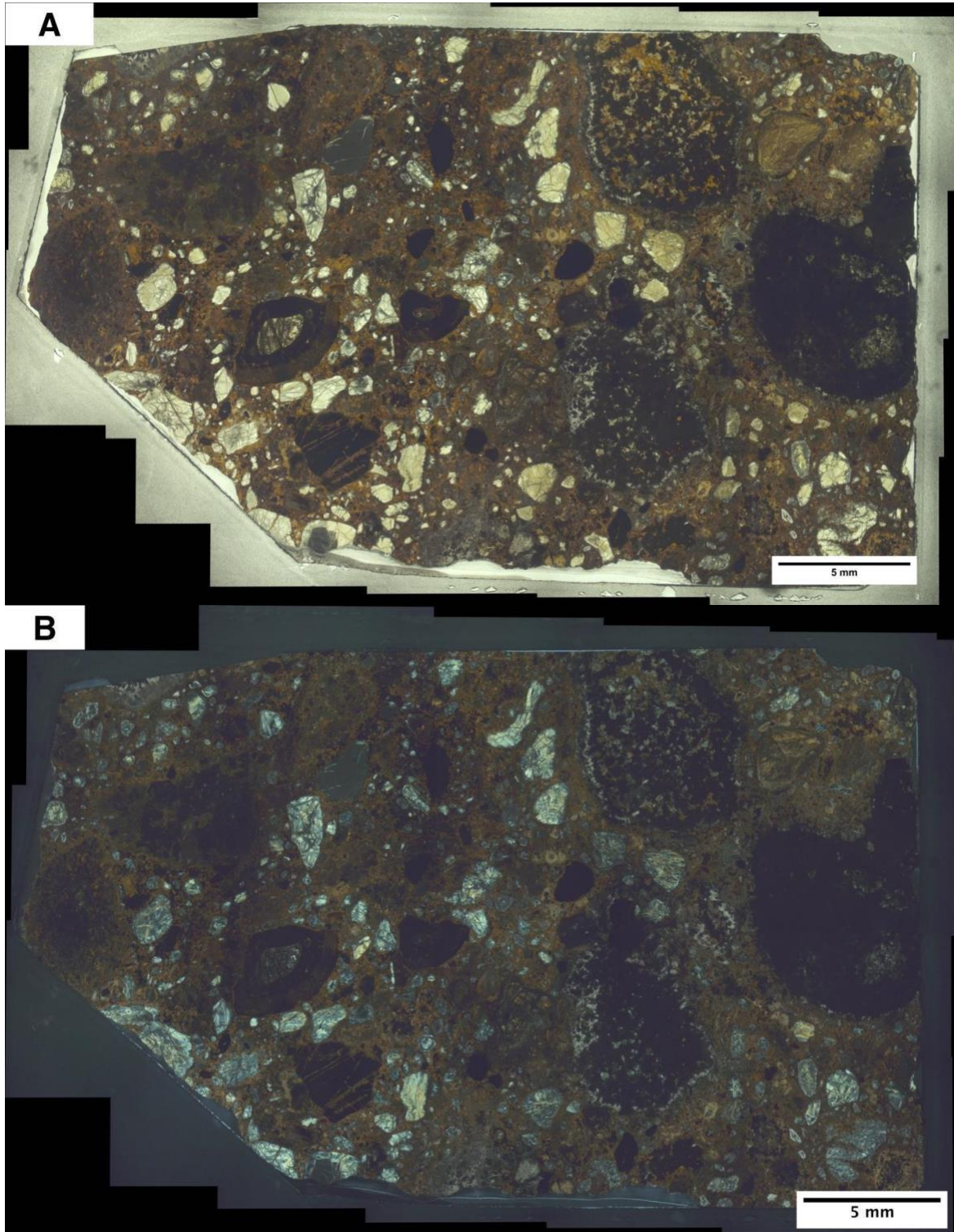
Figure S3: C2103 Dark Piebald Kimberlite imaged in a) plane polarized light and b) cross polarized light
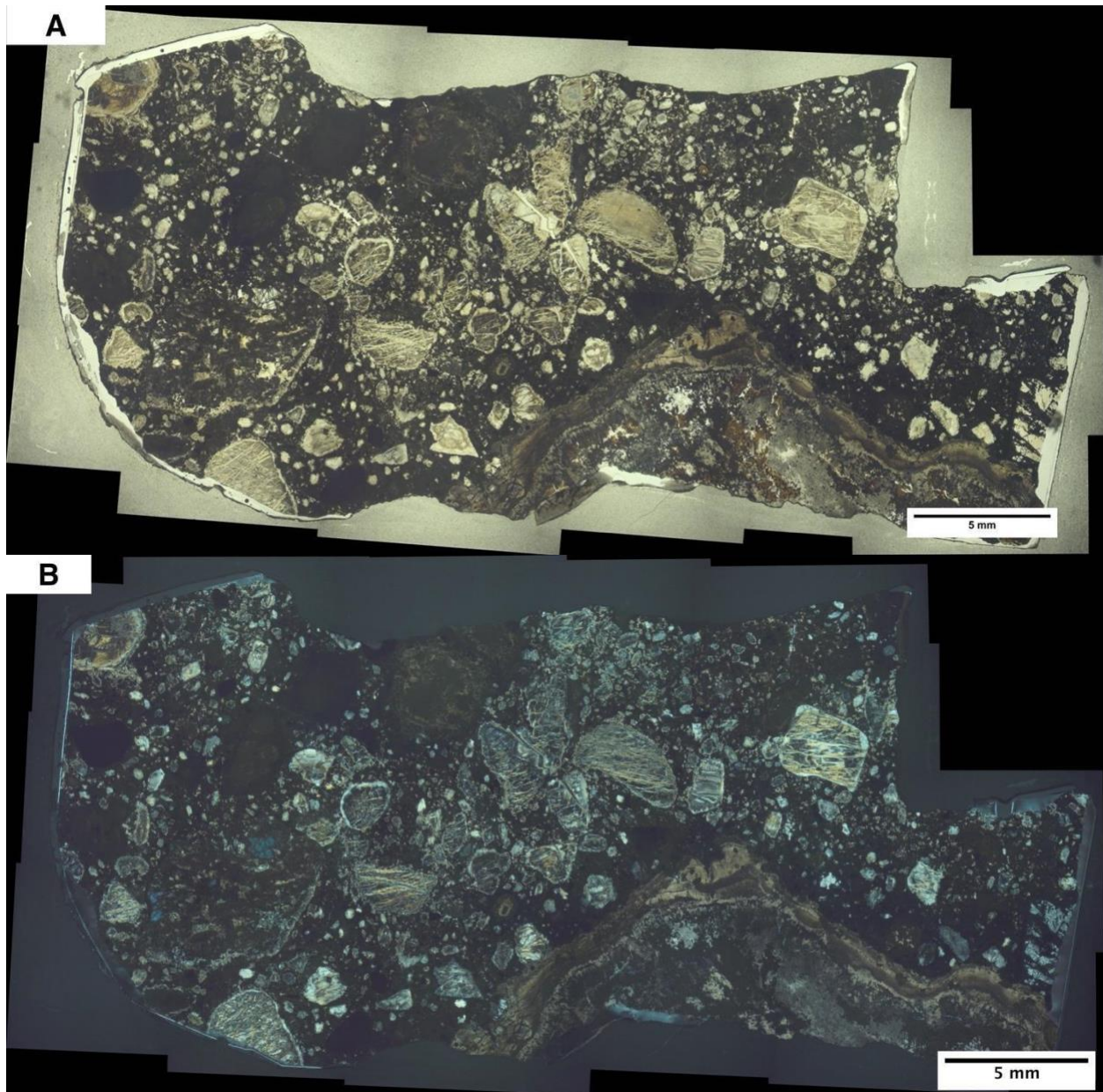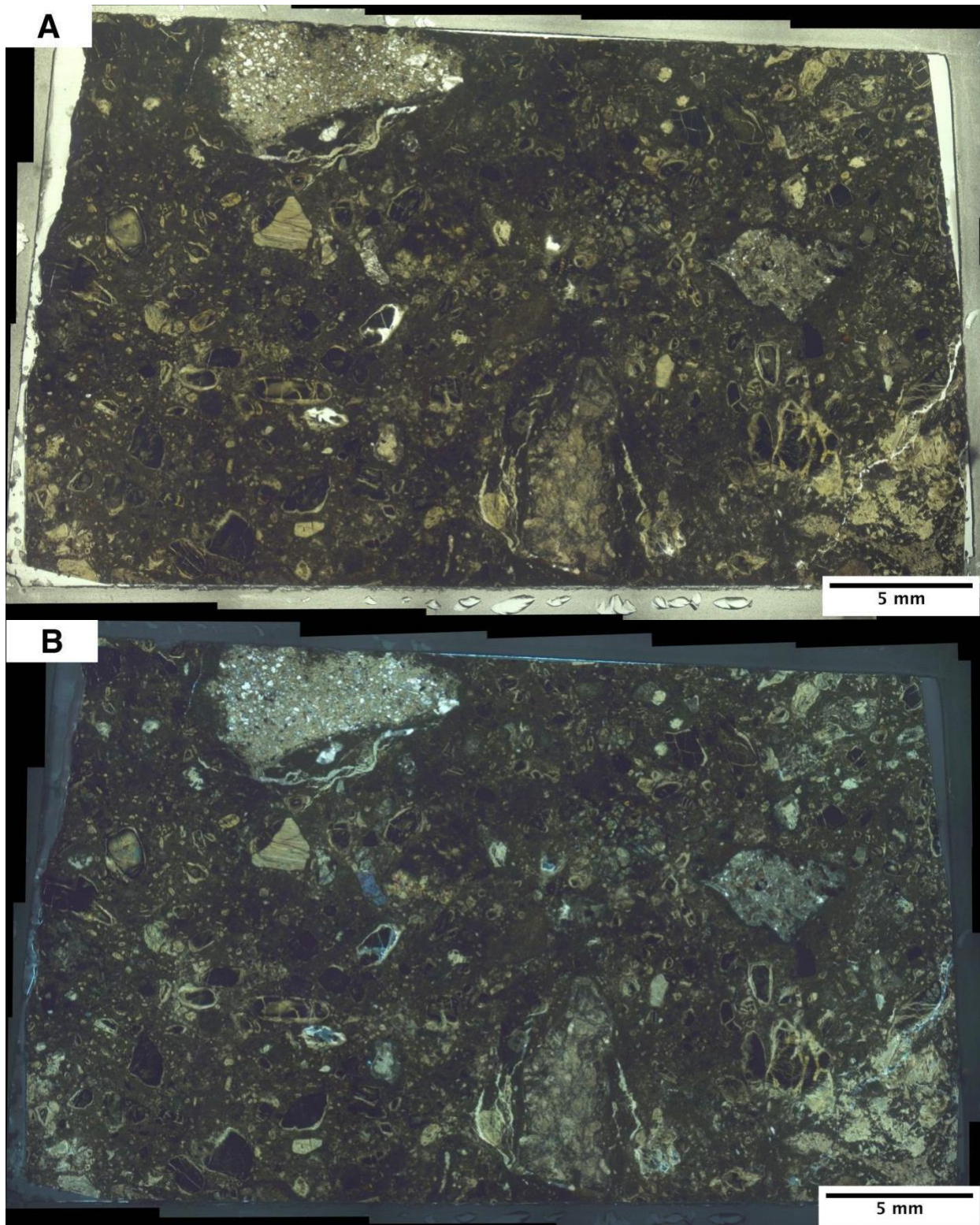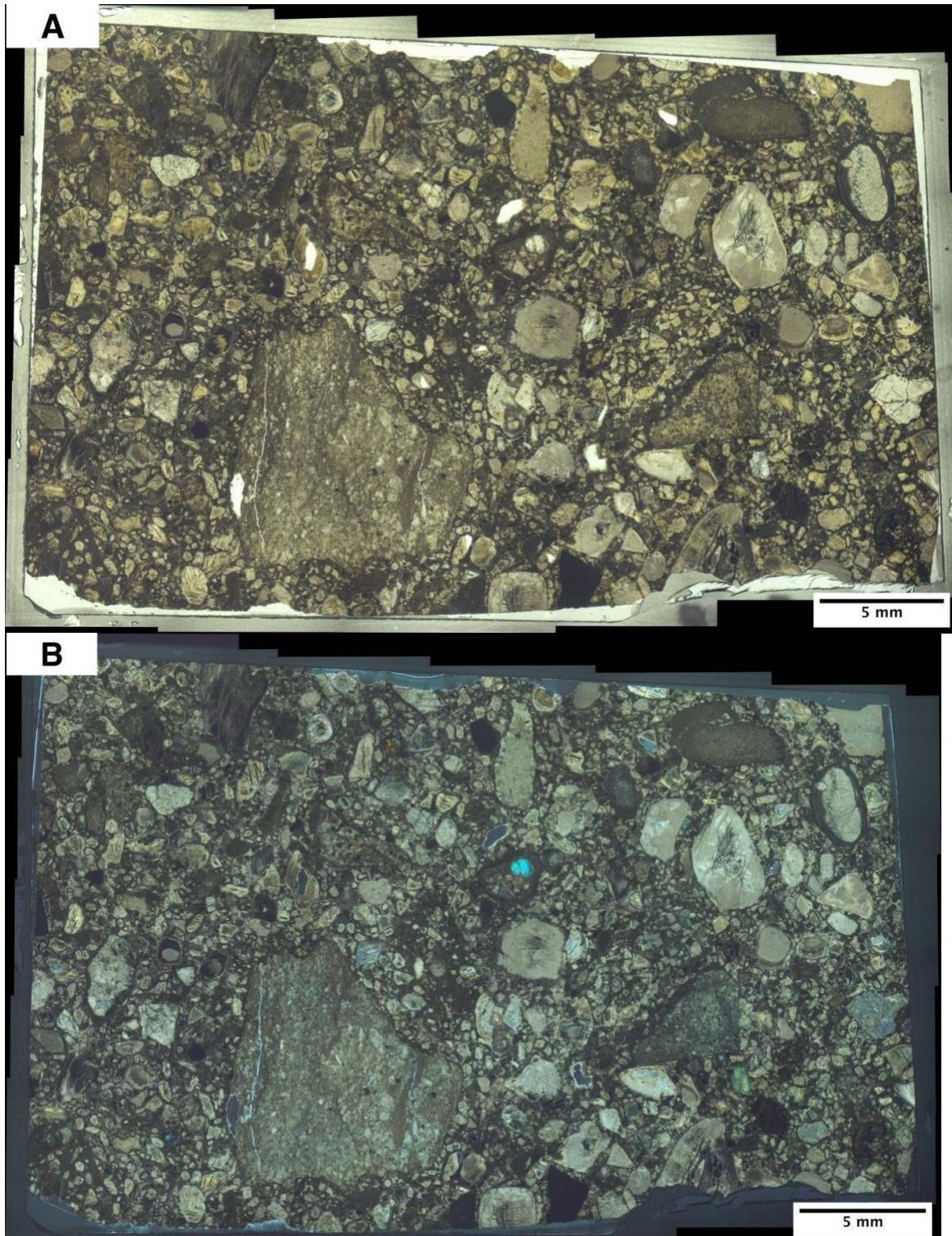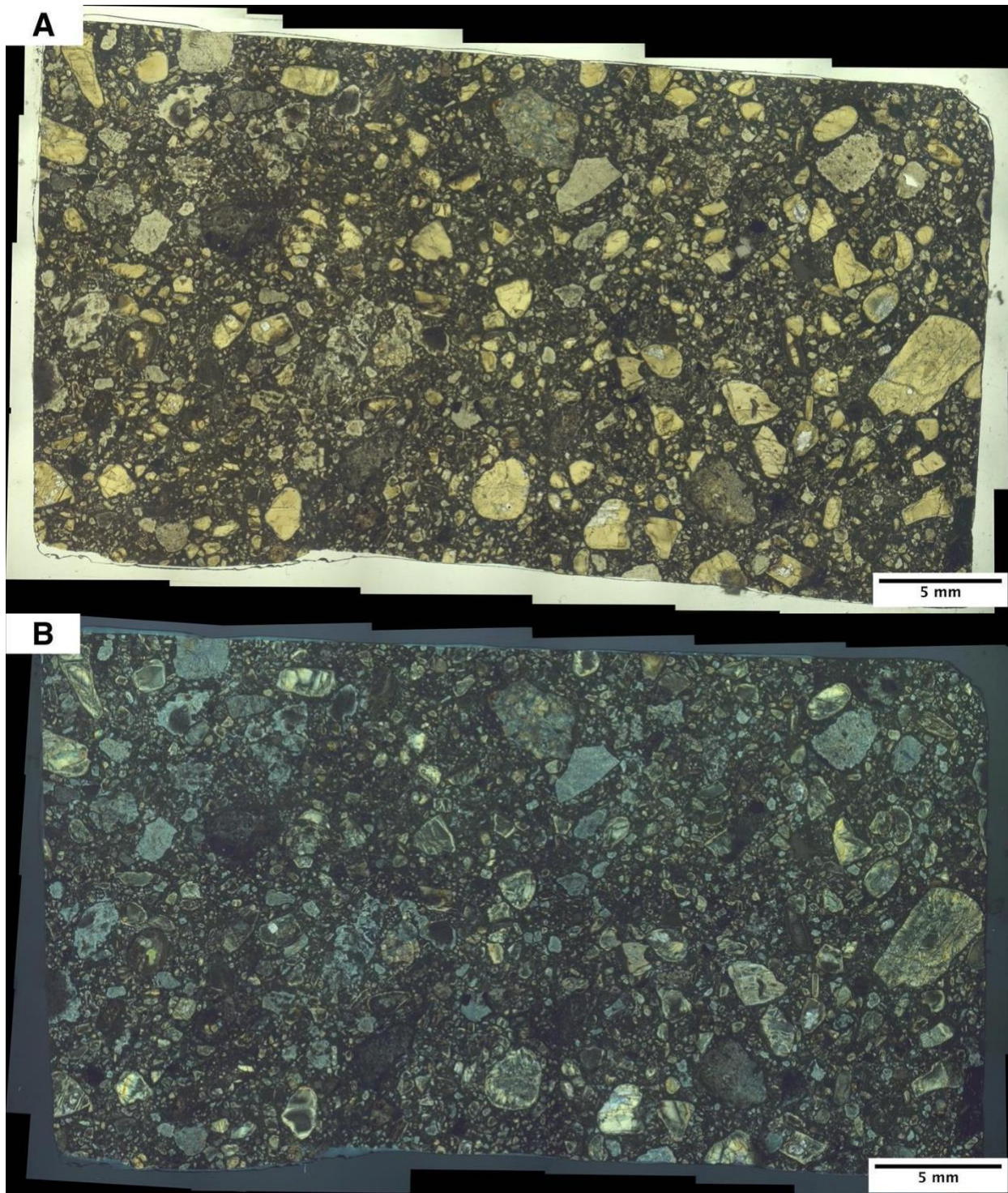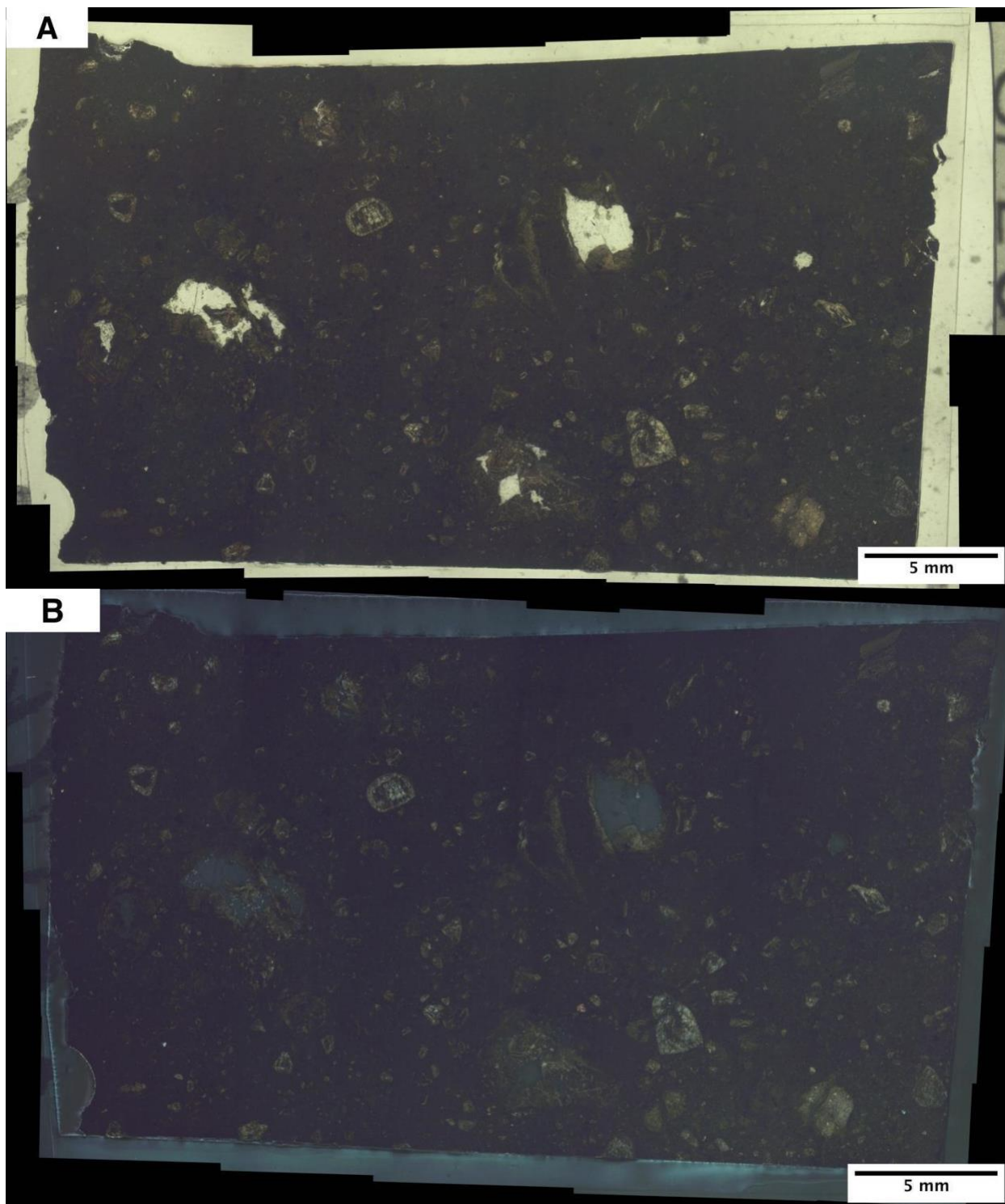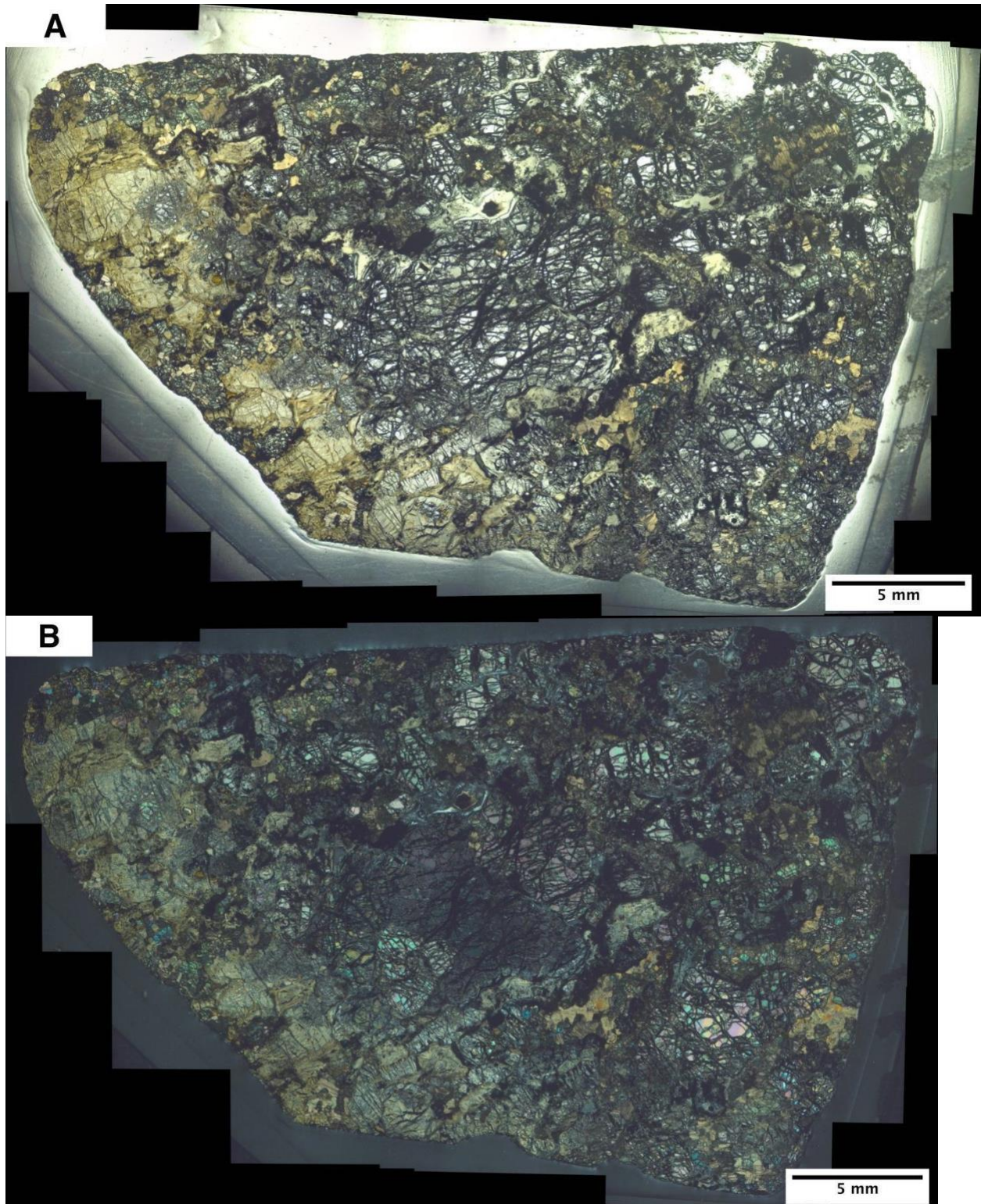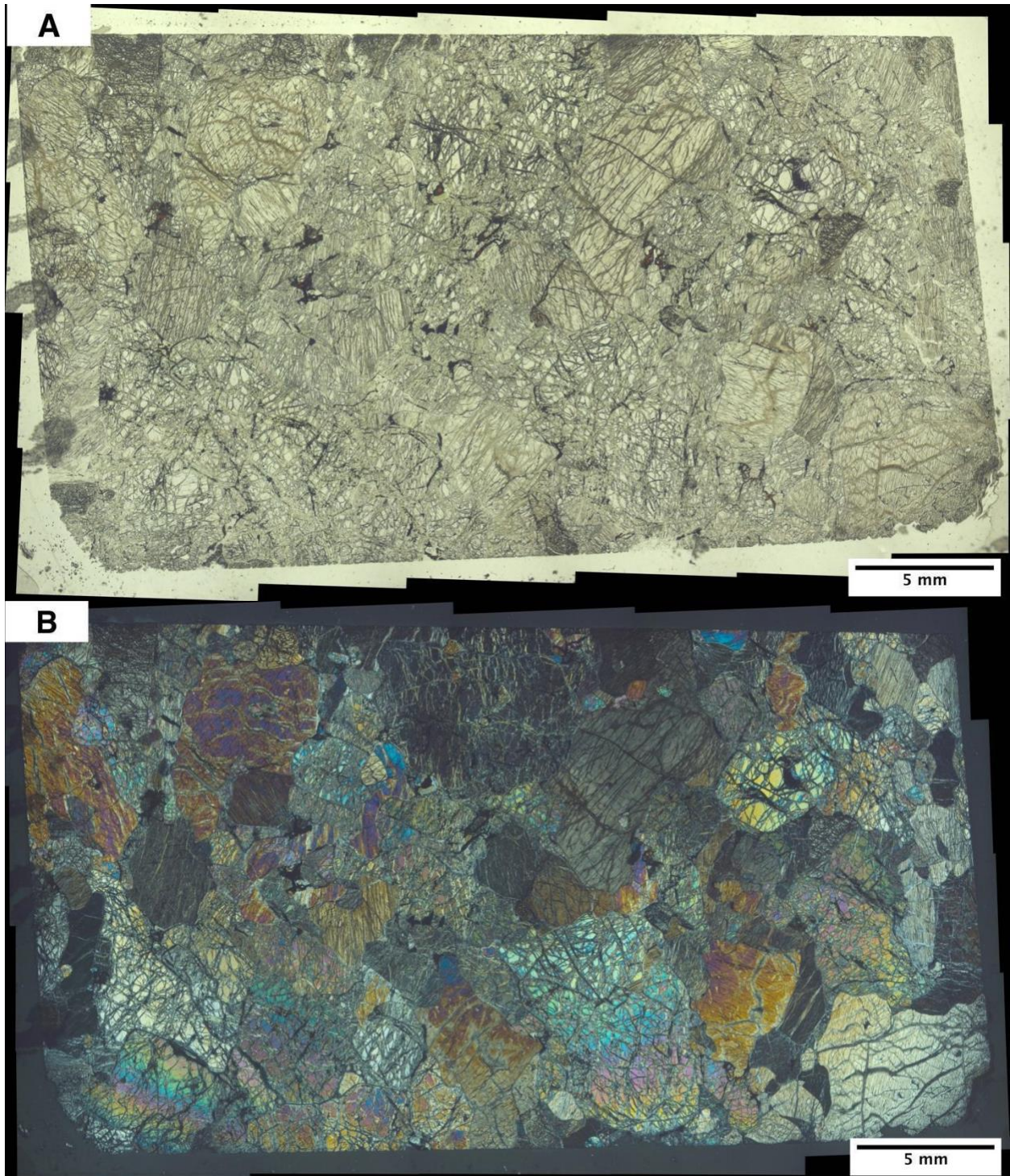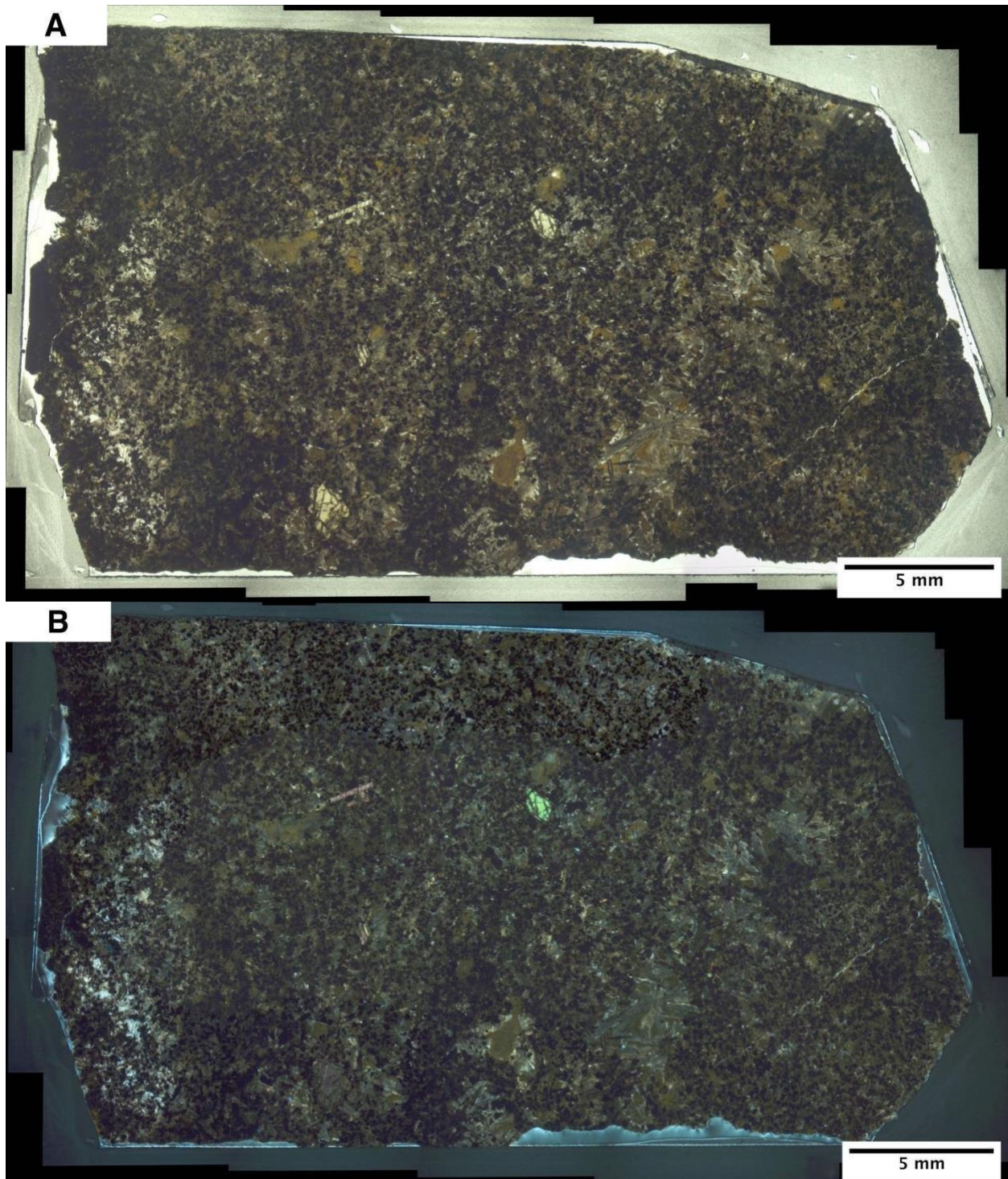
Figure S4: C2104 Pale Piebald Kimberlite imaged in a) plane polarized light and b) cross polarized light
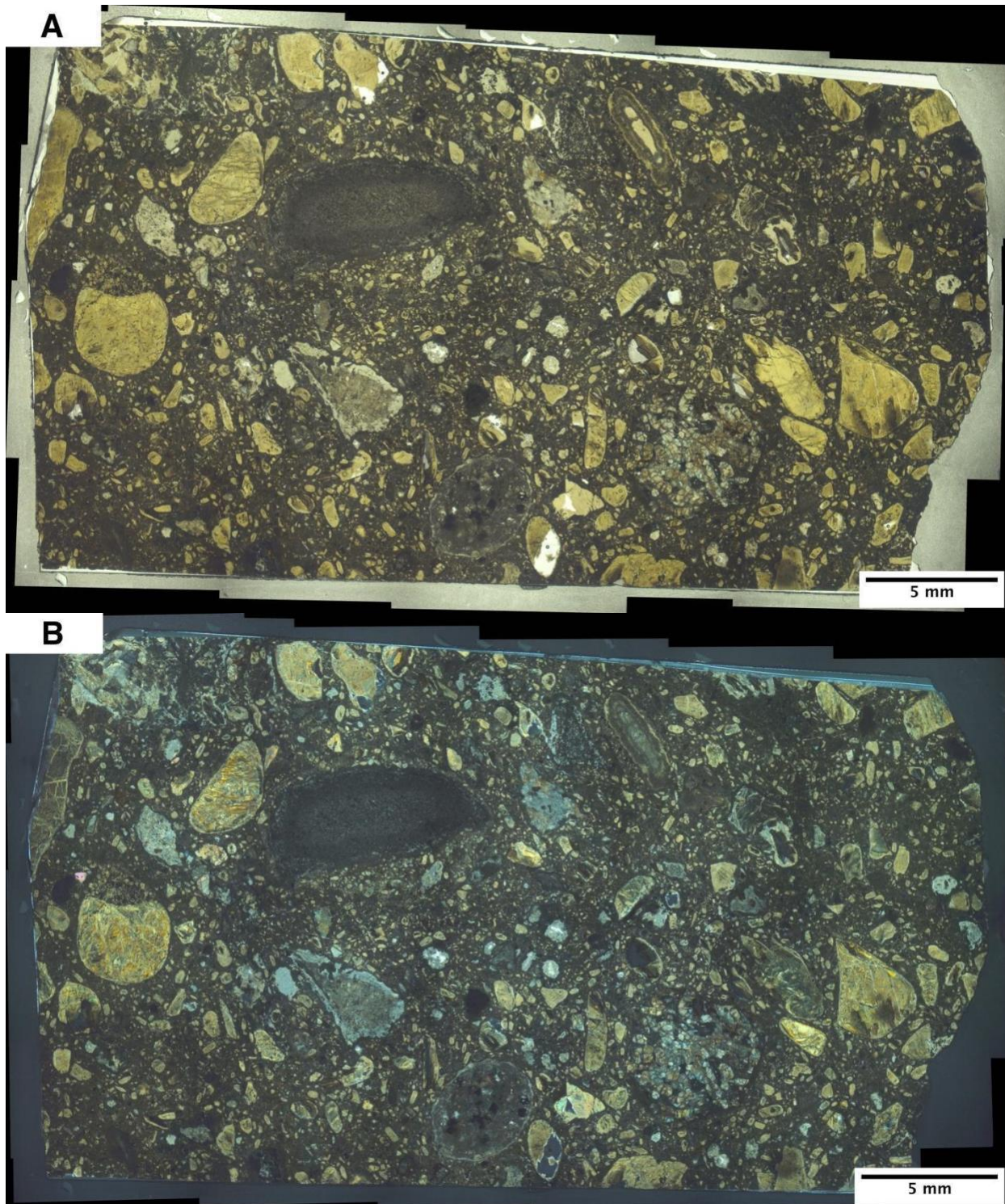
Figure S5: C2105 Blue/Brown Transitional Kimberlite imaged in a) plane polarized light and b) cross polarized light
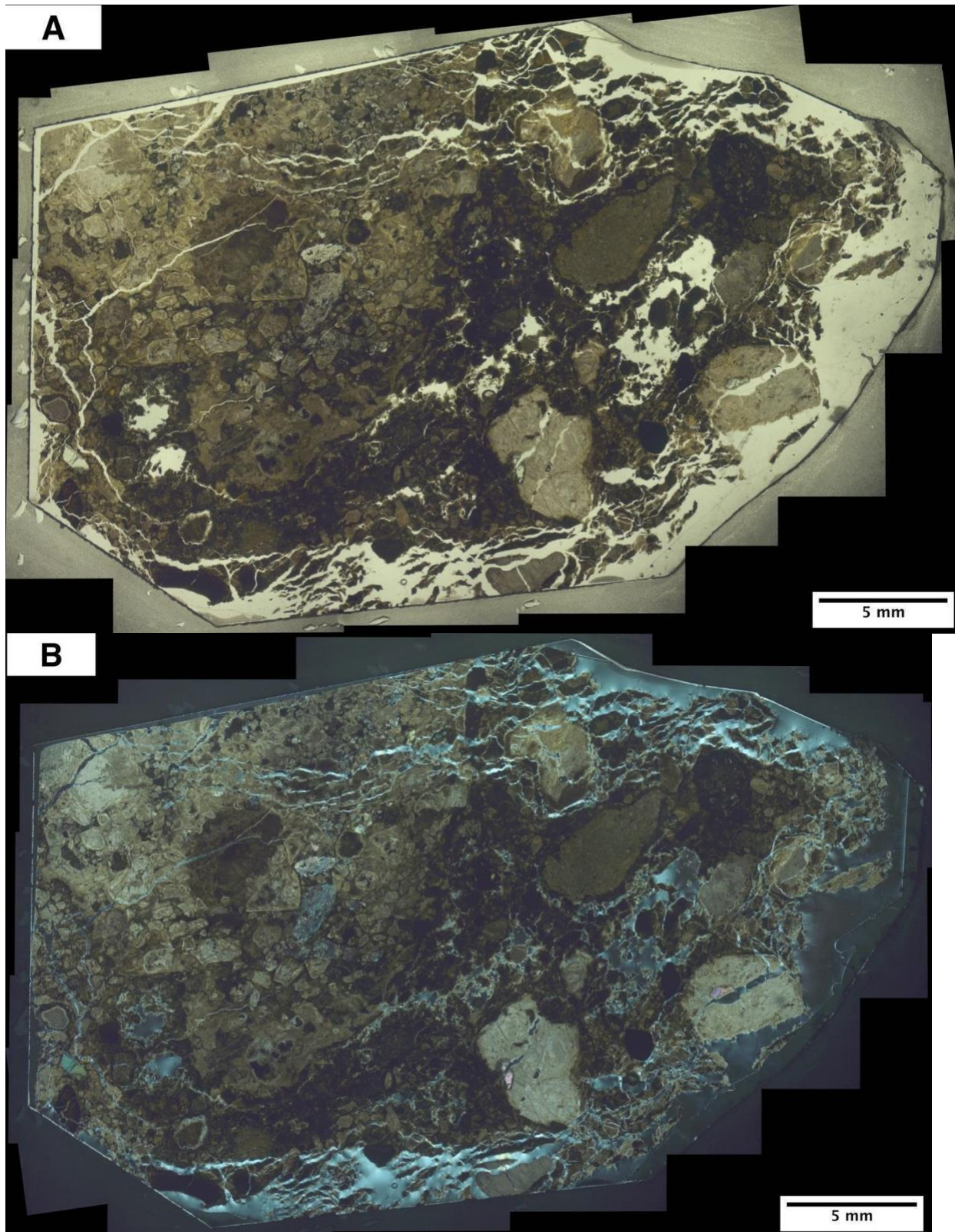
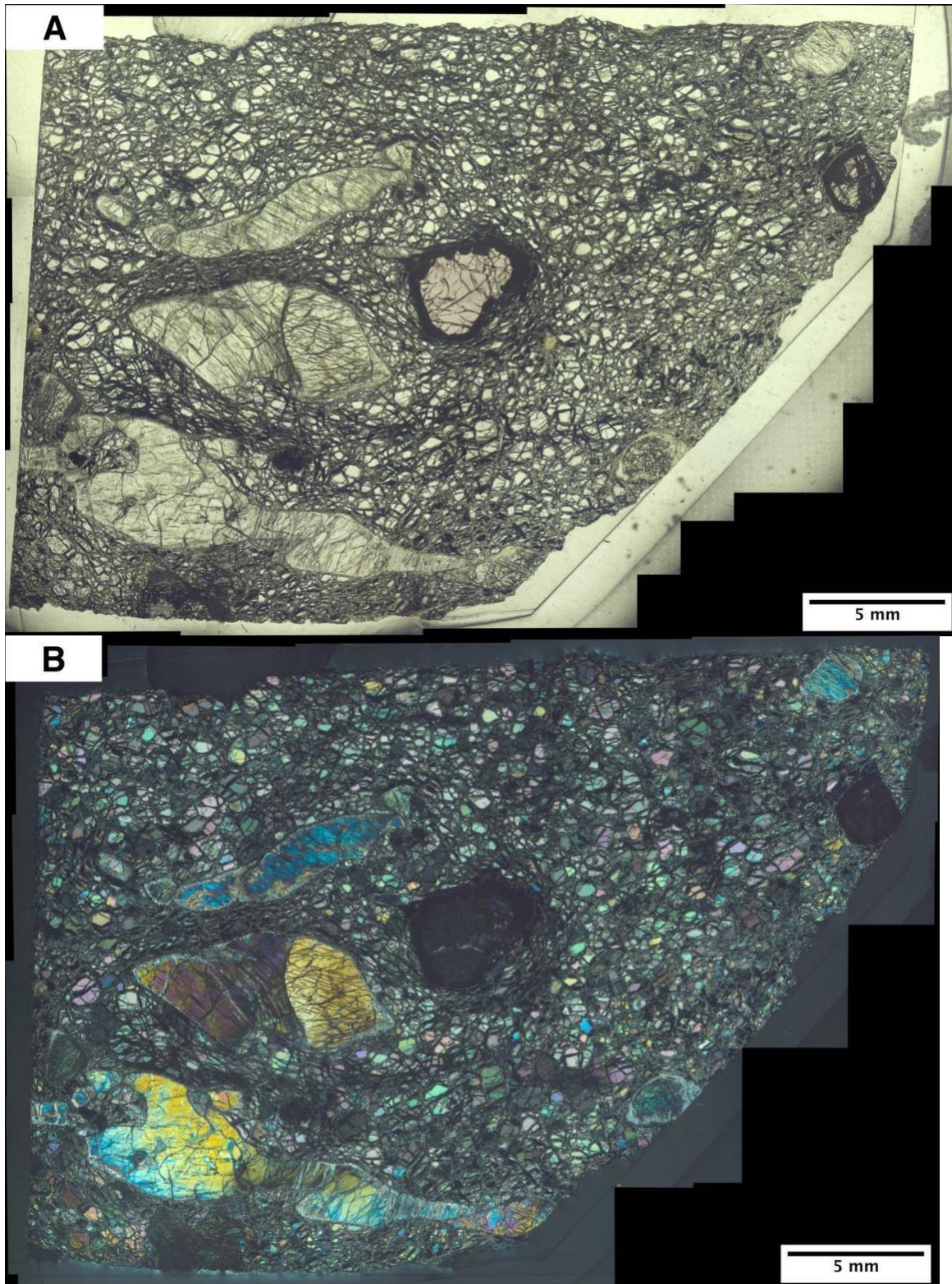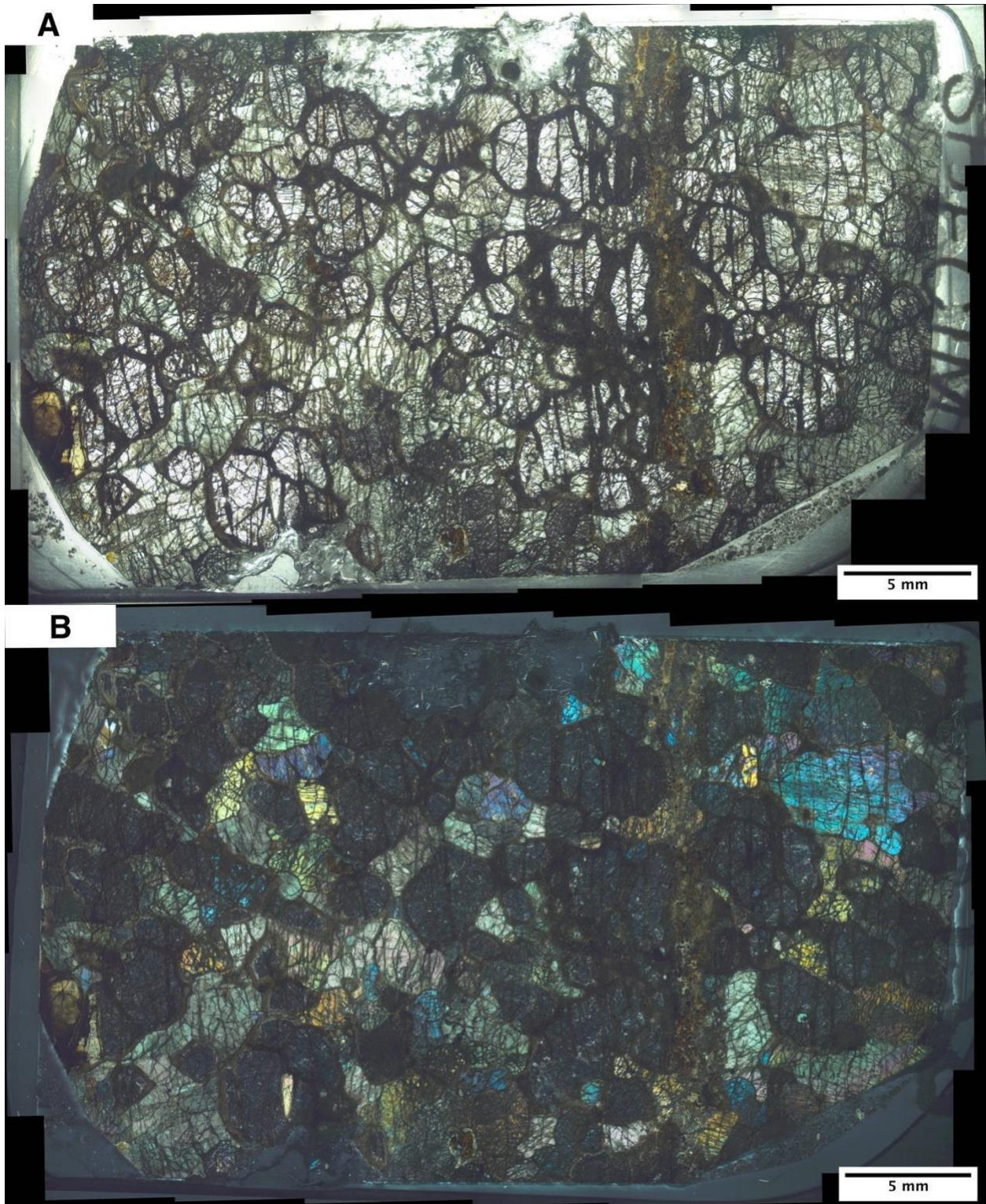**Figure S6:** C2106 Grey Kimberlite imaged in a) plane polarized light and b) cross polarized light
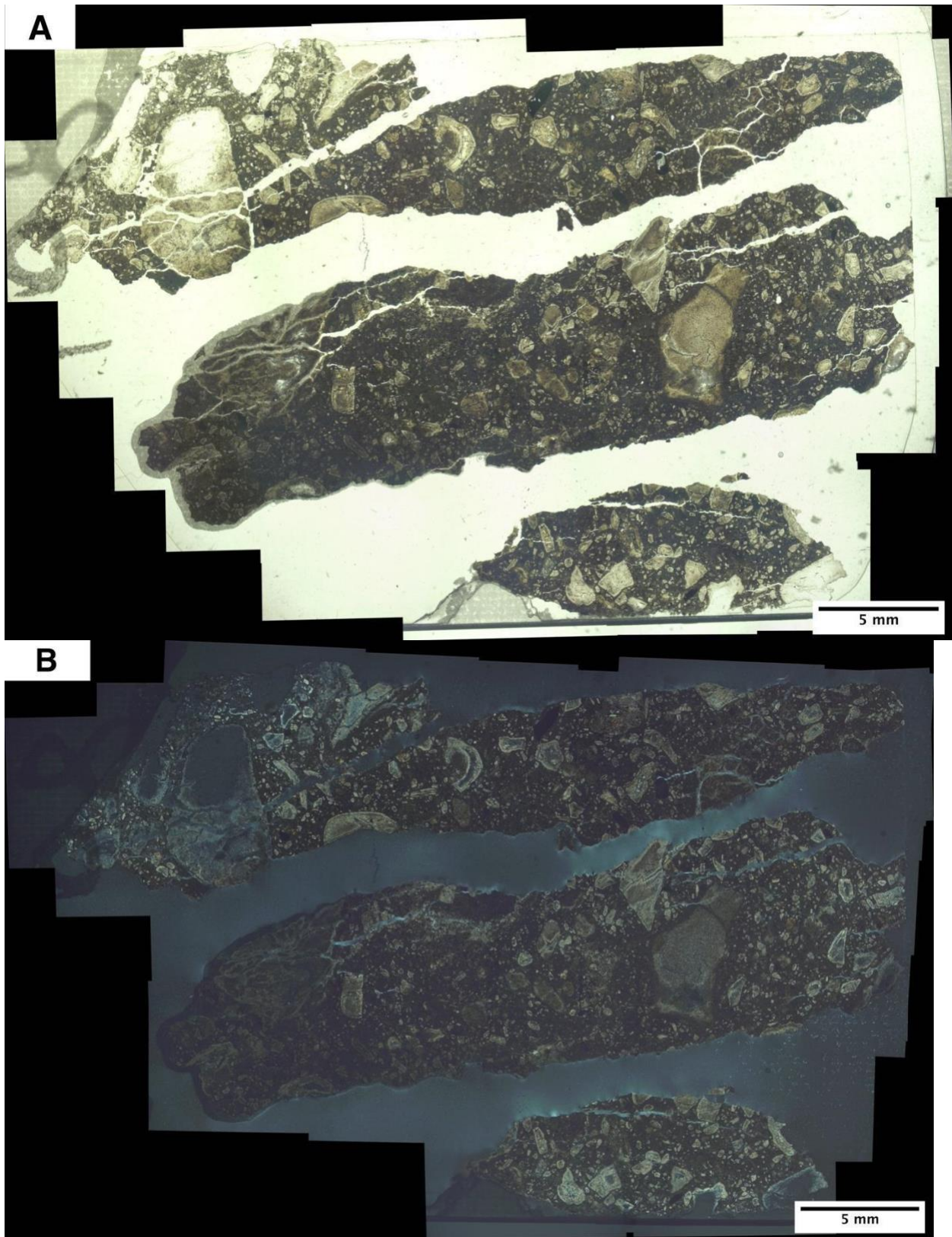
Figure S7: C2108 Grey Kimberlite imaged in a) plane polarized light and b) cross polarized light

Figure S8: C2111 Brown Kimberlite imaged in a) plane polarized light and b) cross polarized light

Figure S9: C2112 Grey Kimberlite imaged in a) plane polarized light and b) cross polarized light
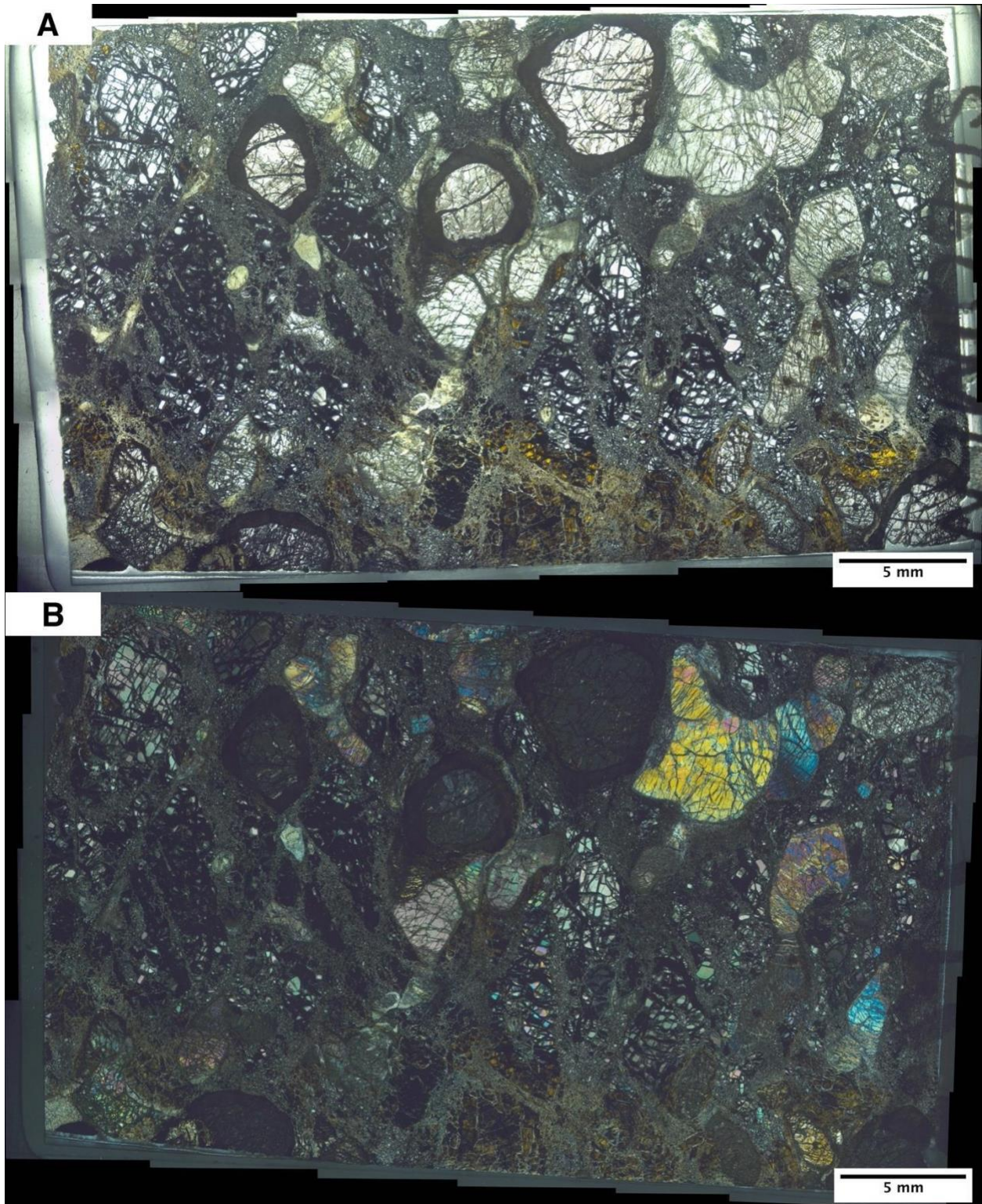
Figure S10: C2113 Fawn Kimberlite imaged in a) plane polarized light and b) cross polarized light

Figure S11: C2114 Grey Kimberlite imaged in a) plane polarized light and b) cross polarized light

Figure S12: C2117 Sheared Lherzolite imaged in a) plane polarized light and b) cross polarized light

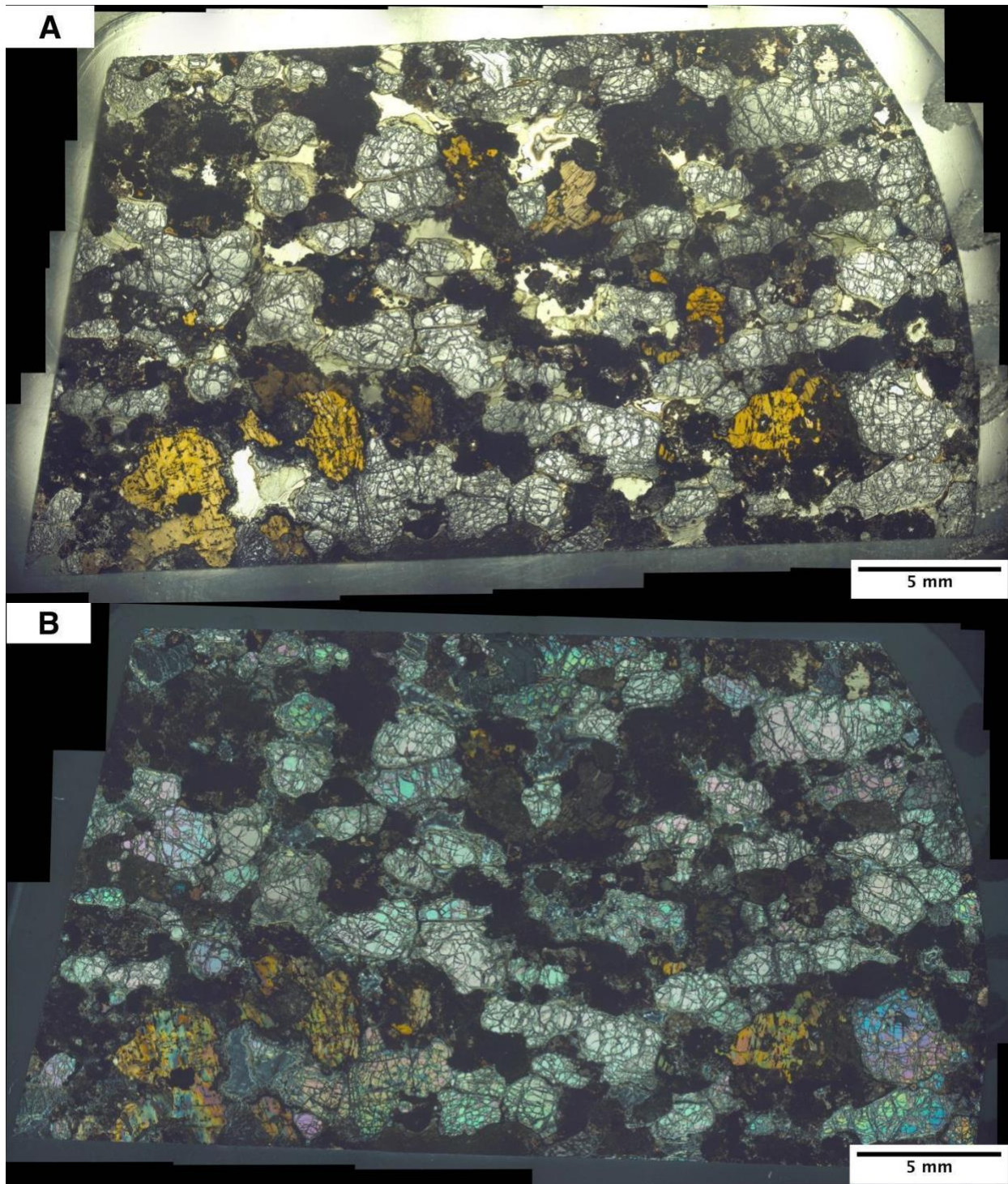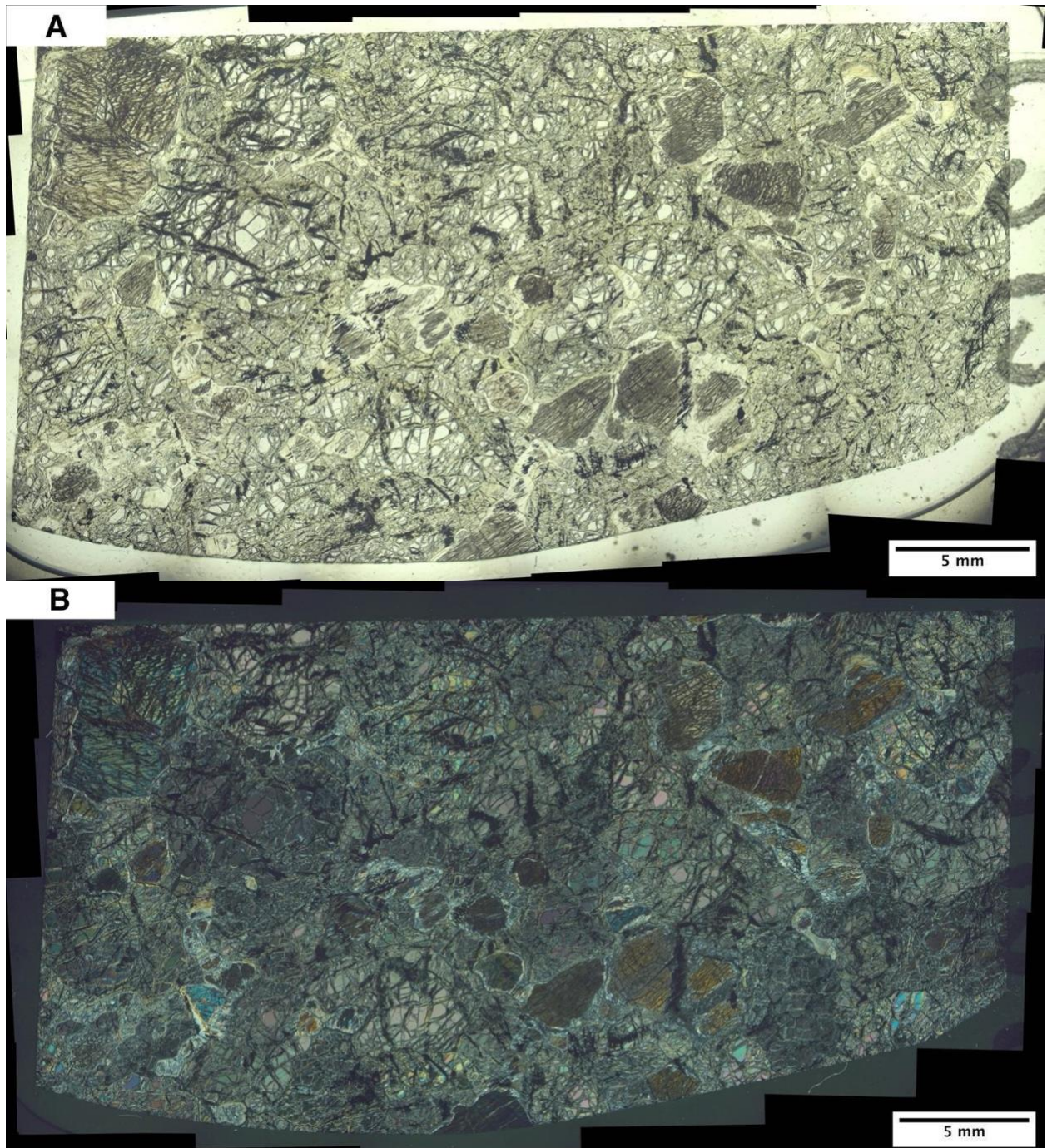**Figure S13:** C2118 Lherzolite imaged in a) plane polarized light and b) cross polarized light

Figure S14: 895RAW imaged in a) plane polarized light and b) cross polarized light
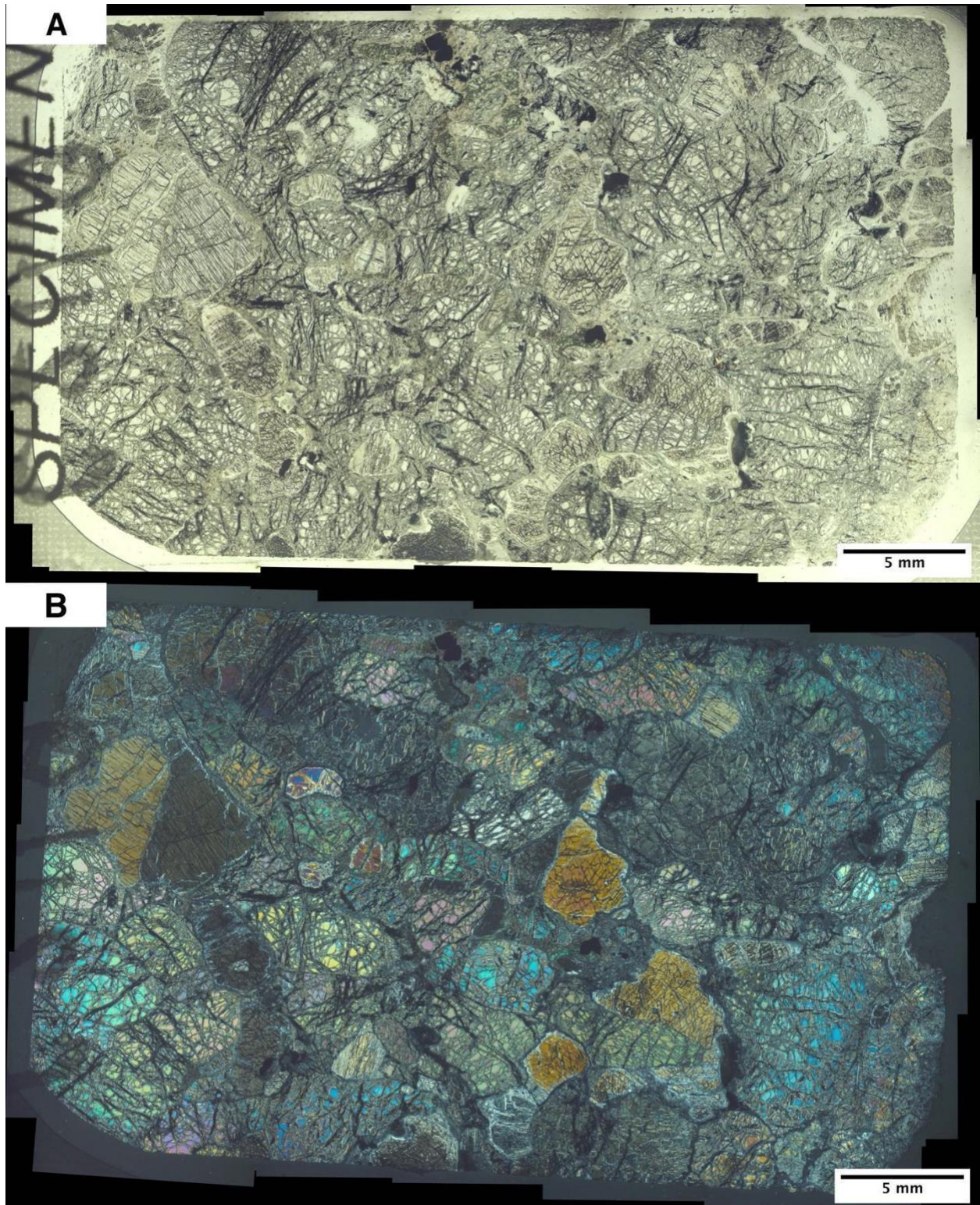
Figure S15: C2119 Lherzolite imaged in a) plane polarized light and b) cross polarized light
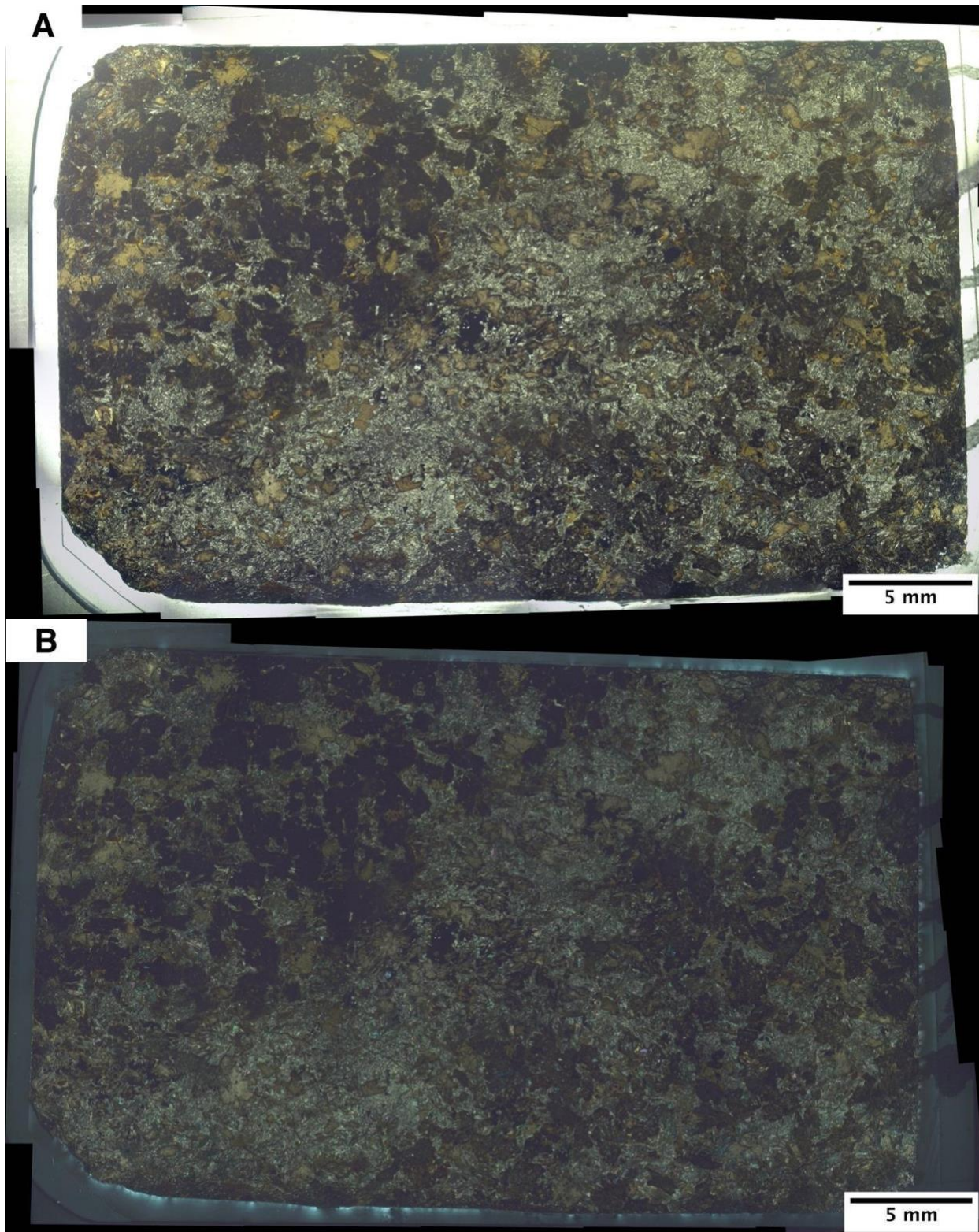
Figure S16: C2121 Garnet Lherzolite imaged in a) plane polarized light and b) cross polarized light

Figure S17: C2122 Pyroxenite imaged in a) plane polarized light and b) cross polarized light
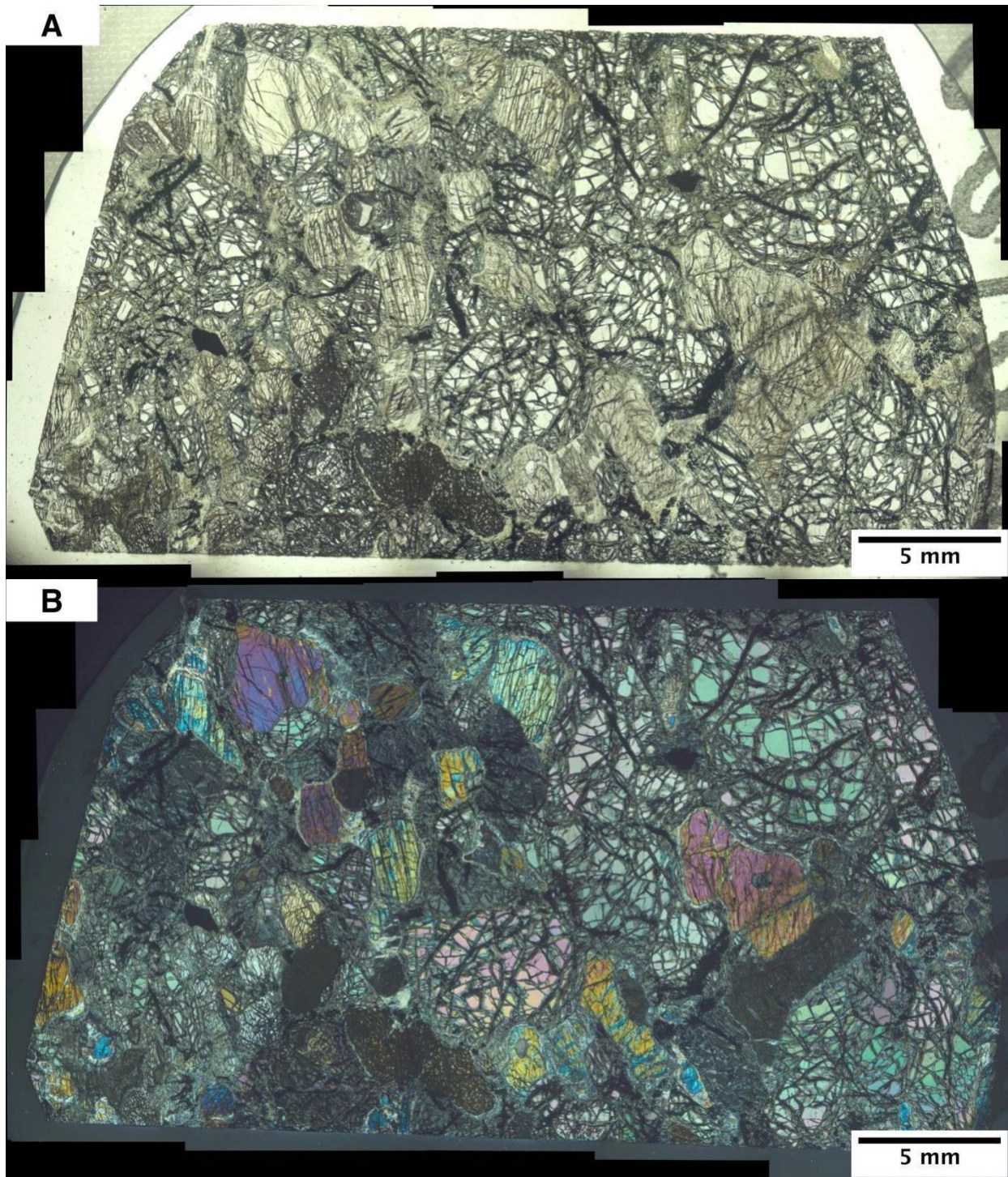
Figure S18: C2123 Garnet Lherzolite imaged in a) plane polarized light and b) cross polarized light

Figure S19: C2124 Garnet Lherzolite imaged in a) plane polarized light and b) cross polarized light

Figure S20: C2125 Harzburgite imaged in a) plane polarized light and b) cross polarized light

Figure S21: C2126 Pyroxenite imaged in a) plane polarized light and b) cross polarized light

Figure S22: C2127 Harzburgite imaged in a) plane polarized light and b) cross polarized light
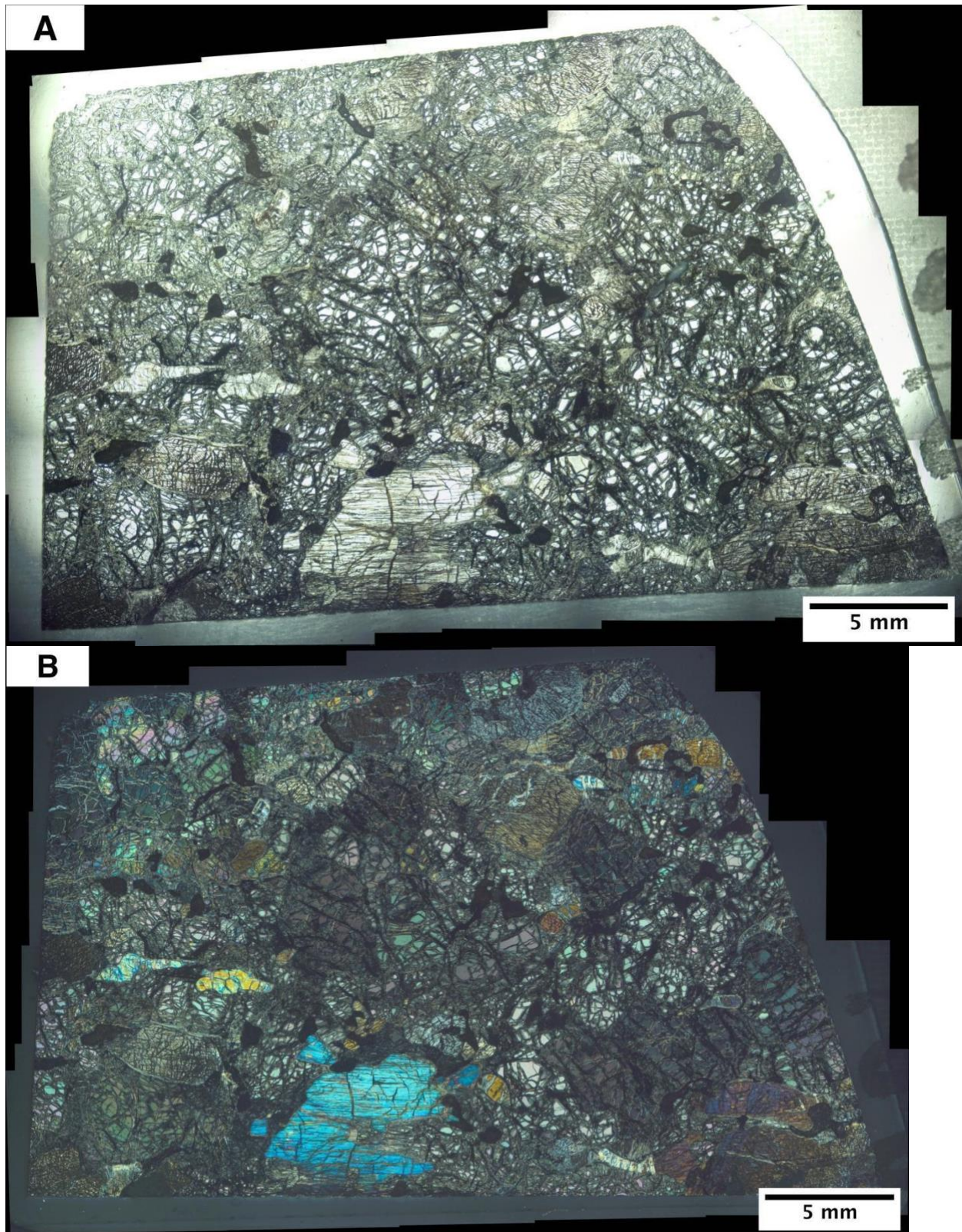
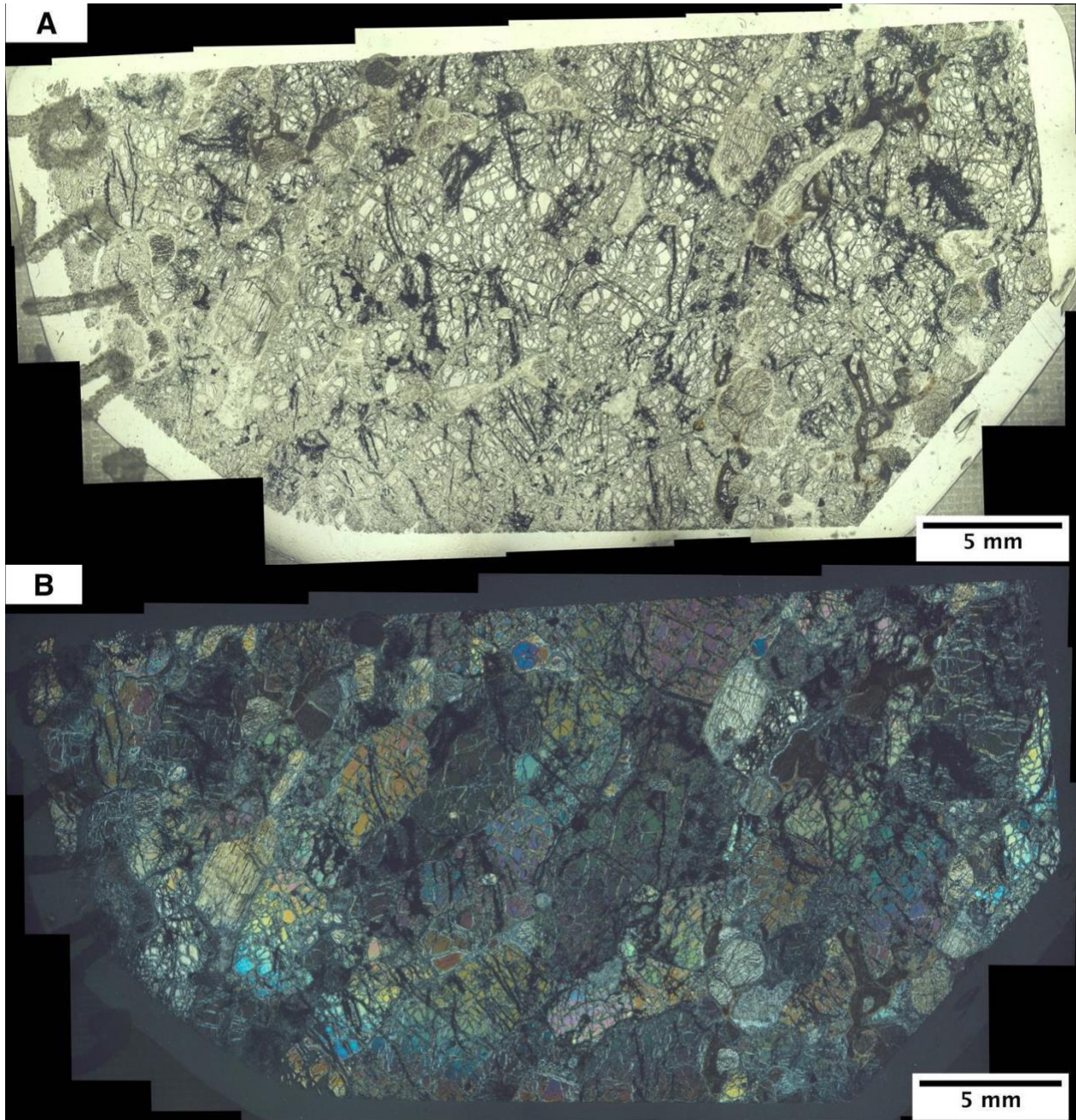**Figure S23:** C2128 Harzburgite imaged in a) plane polarized light and b) cross polarized light

Figure S24: C2129 Harzburgite imaged in a) plane polarized light and b) cross polarized light
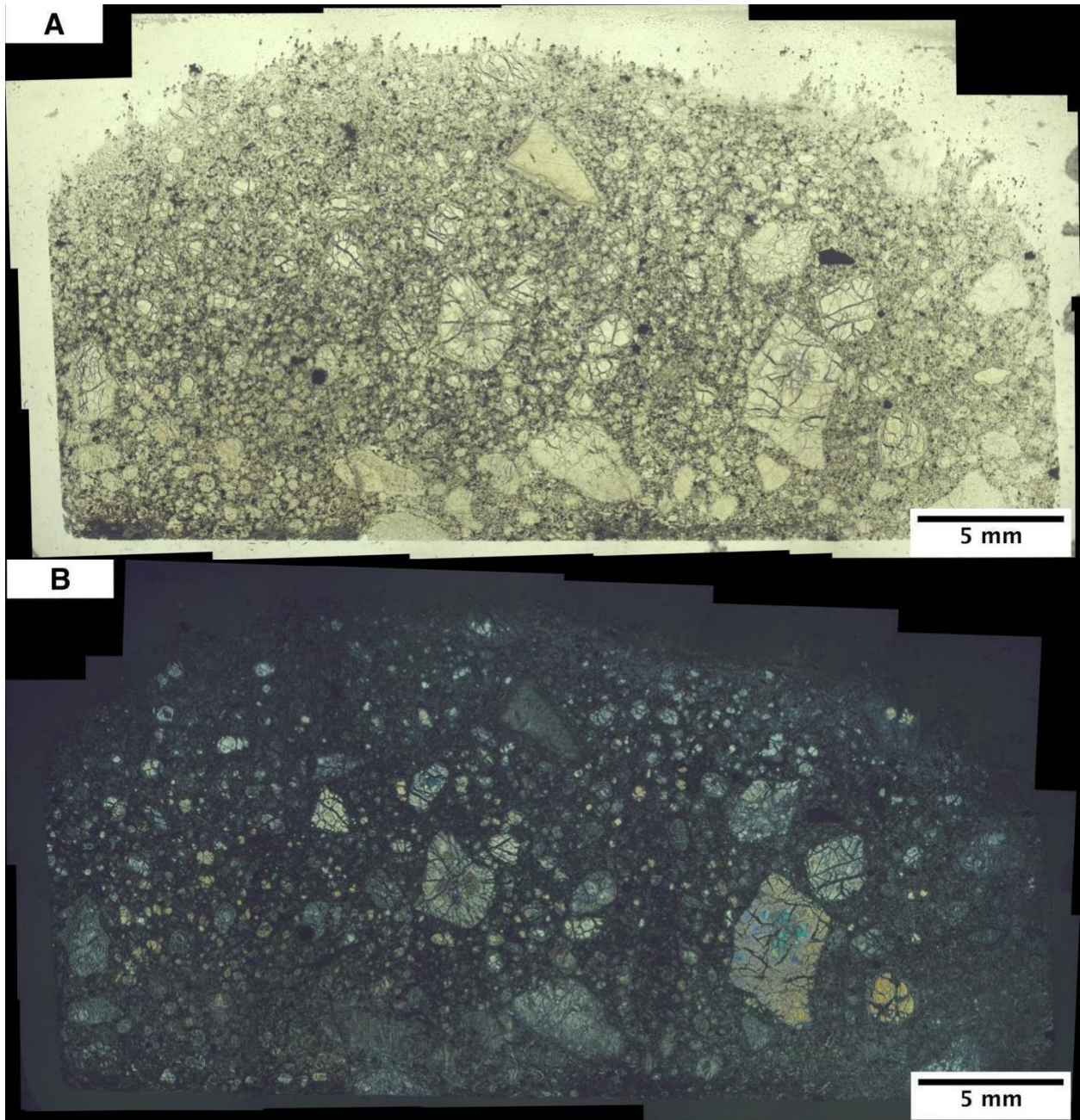
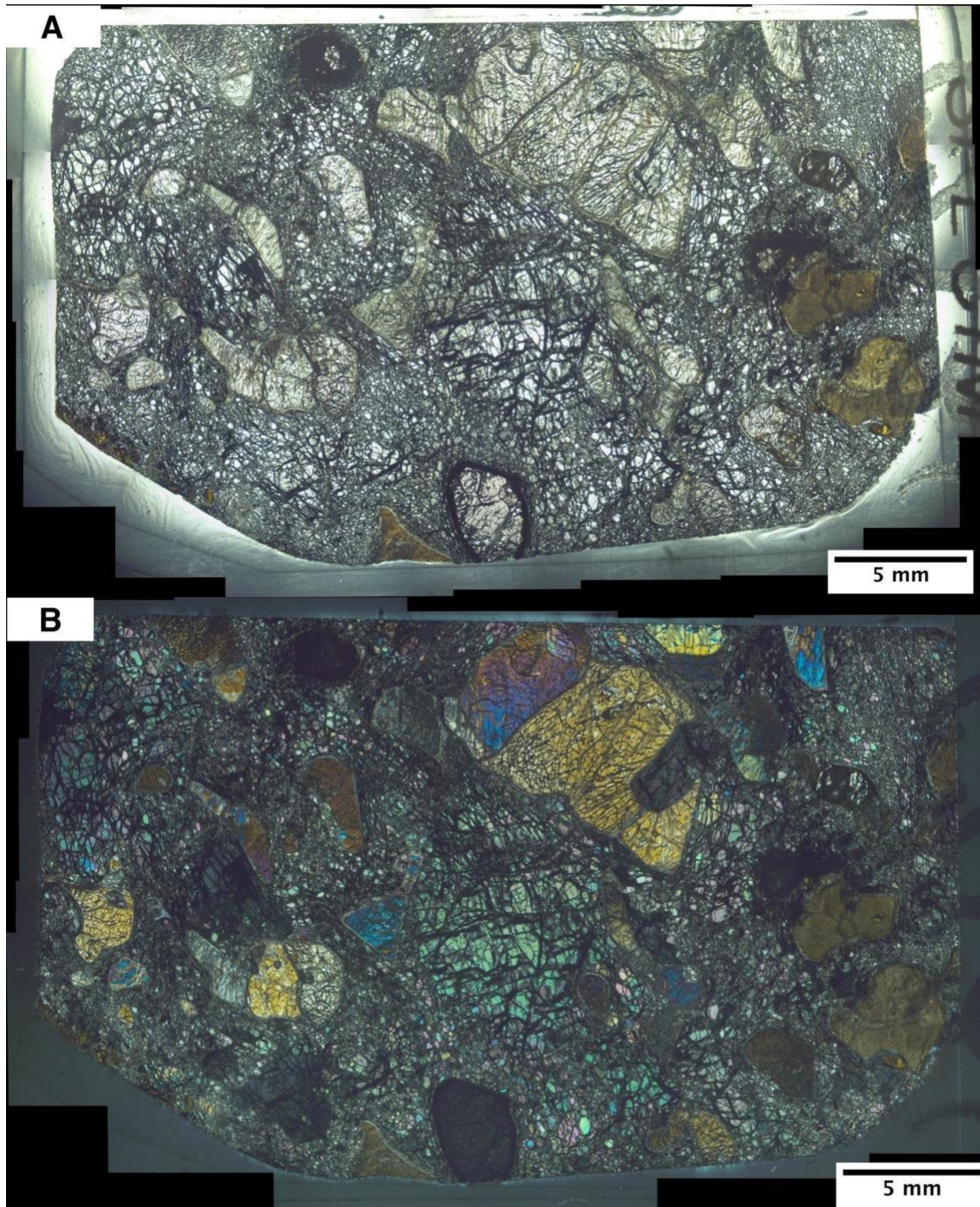**Figure S25:** C2130 imaged in a) plane polarized light and b) cross polarized light

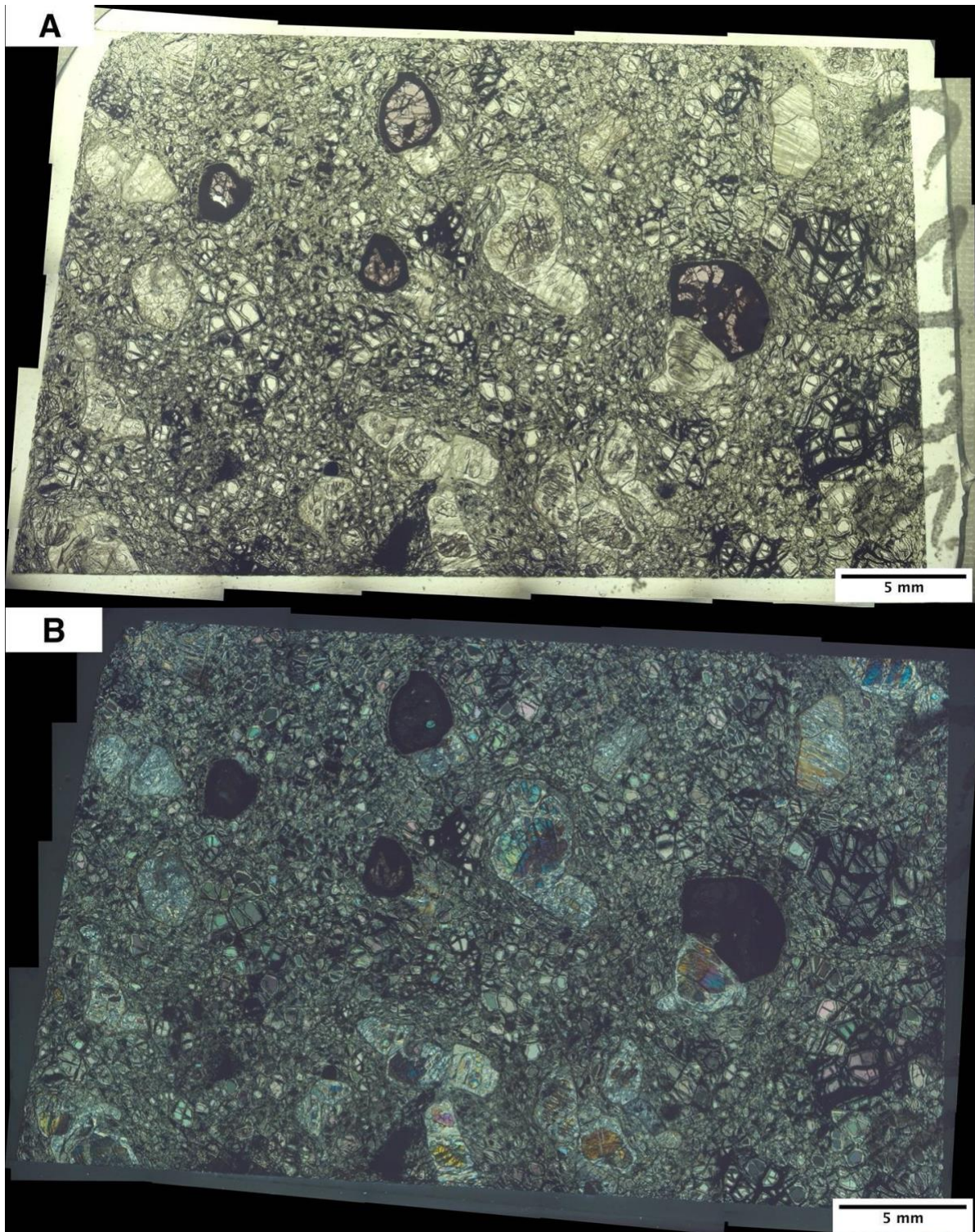**Figure S26:** C2131 Garnet Harzburgite imaged in a) plane polarized light and b) cross polarized light

Figure S27: C2132 Garnet Harzburgite imaged in a) plane polarized light and b) cross polarized light
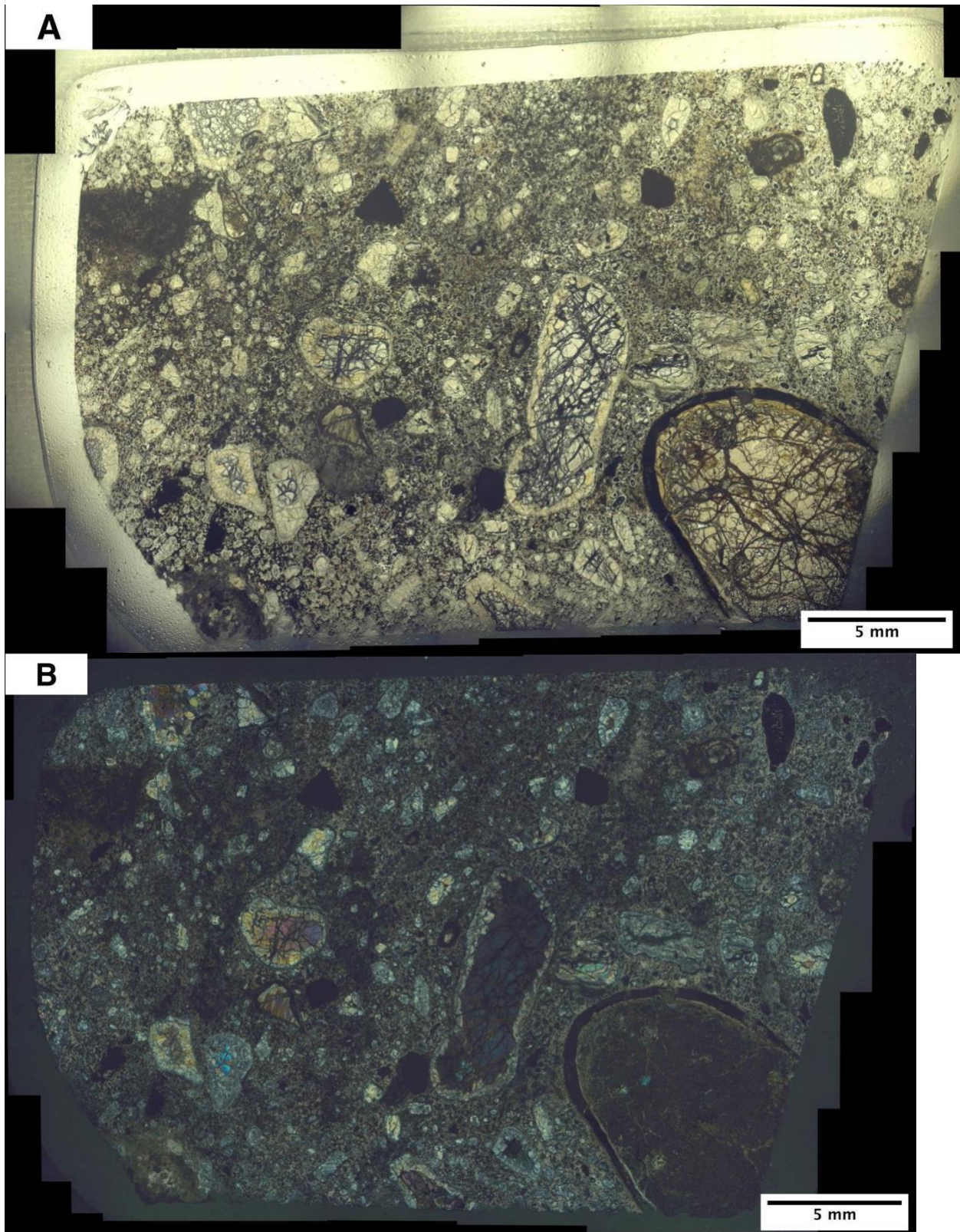
Figure S28: C2133 imaged in a) plane polarized light and b) cross polarized light

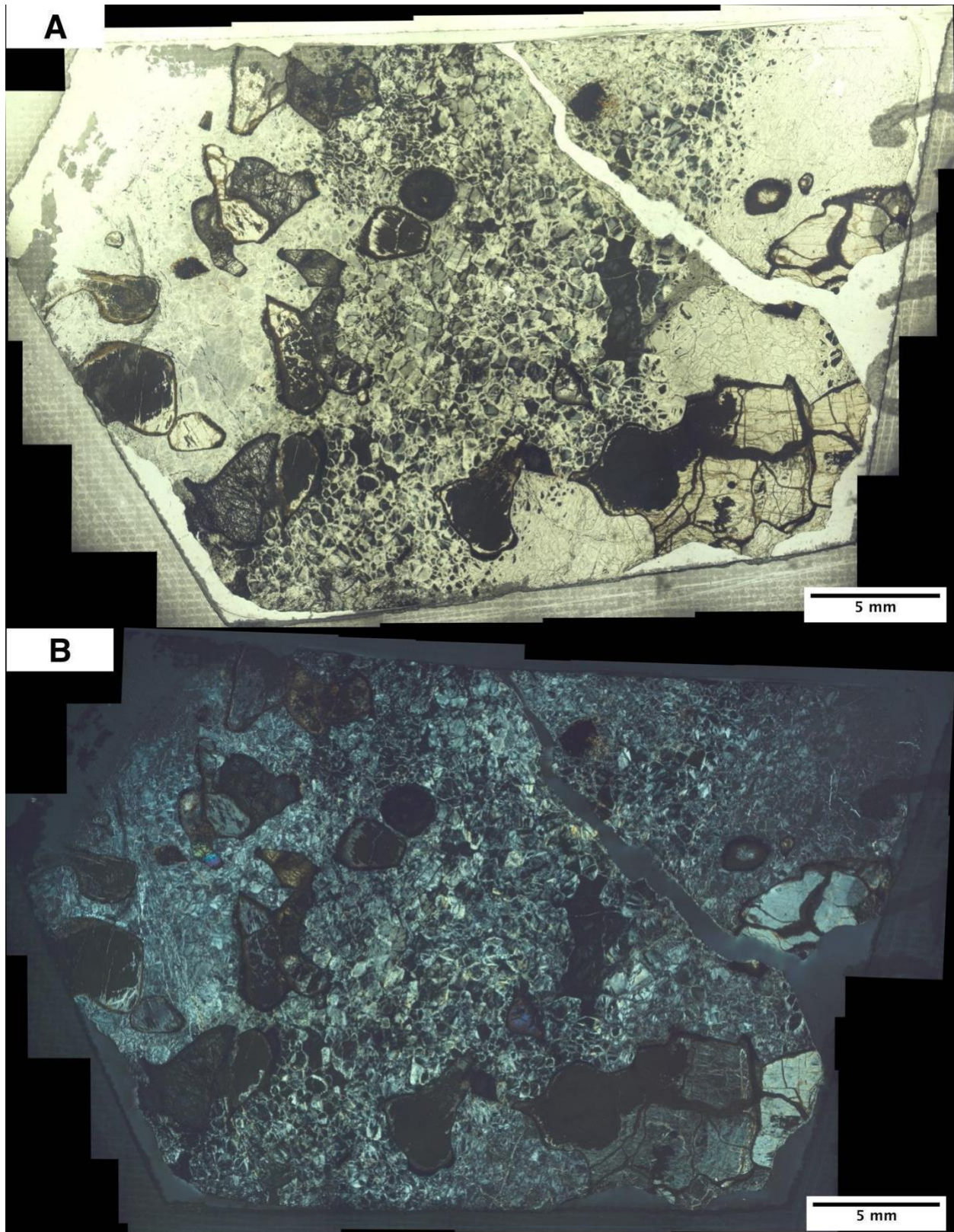**Figure S29:** C2134 Garnet Harzburgite imaged in a) plane polarized light and b) cross polarized light
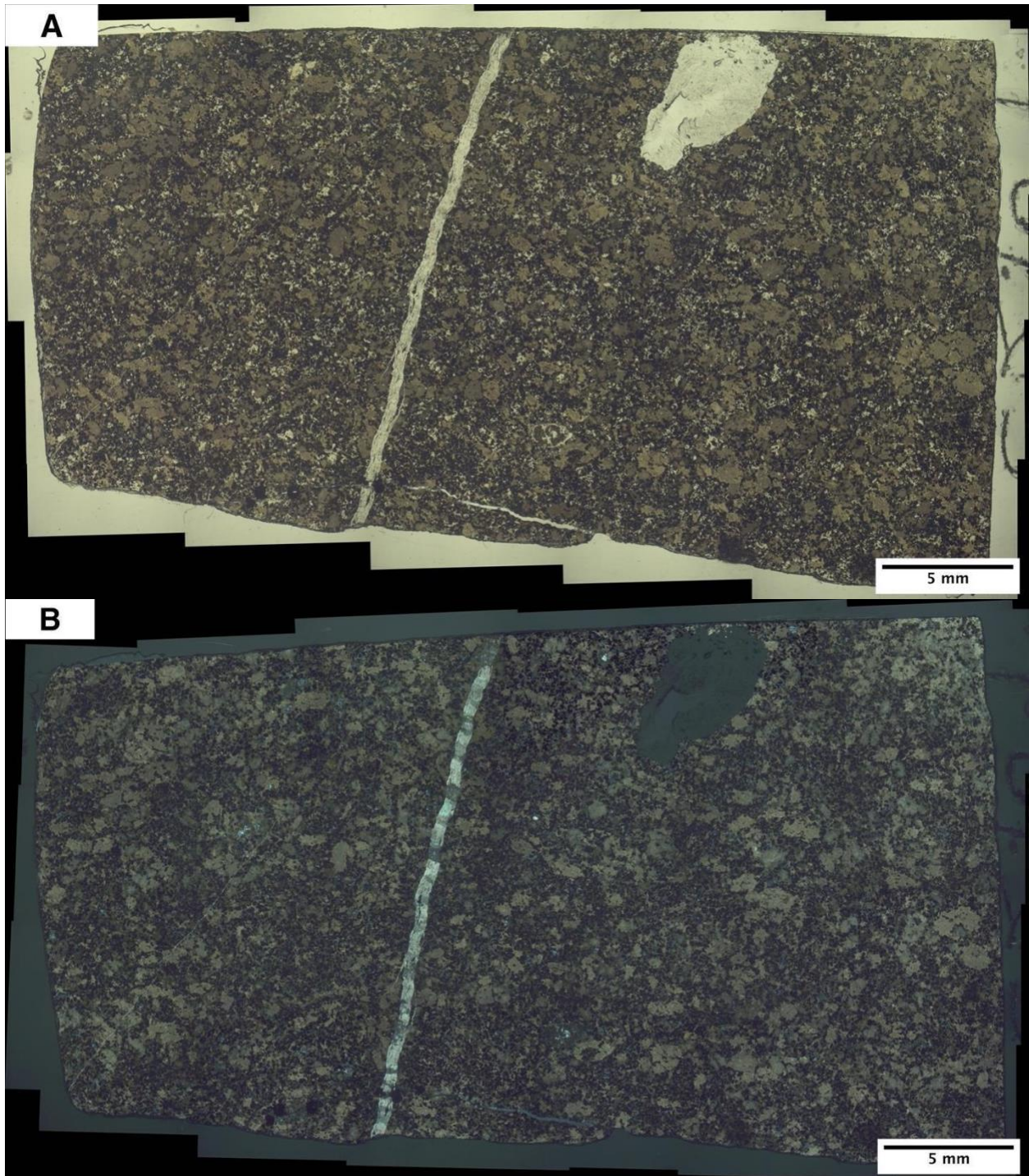
Figure S30: C2109 Calcite dike imaged in a) plane polarized light and b) cross polarized light
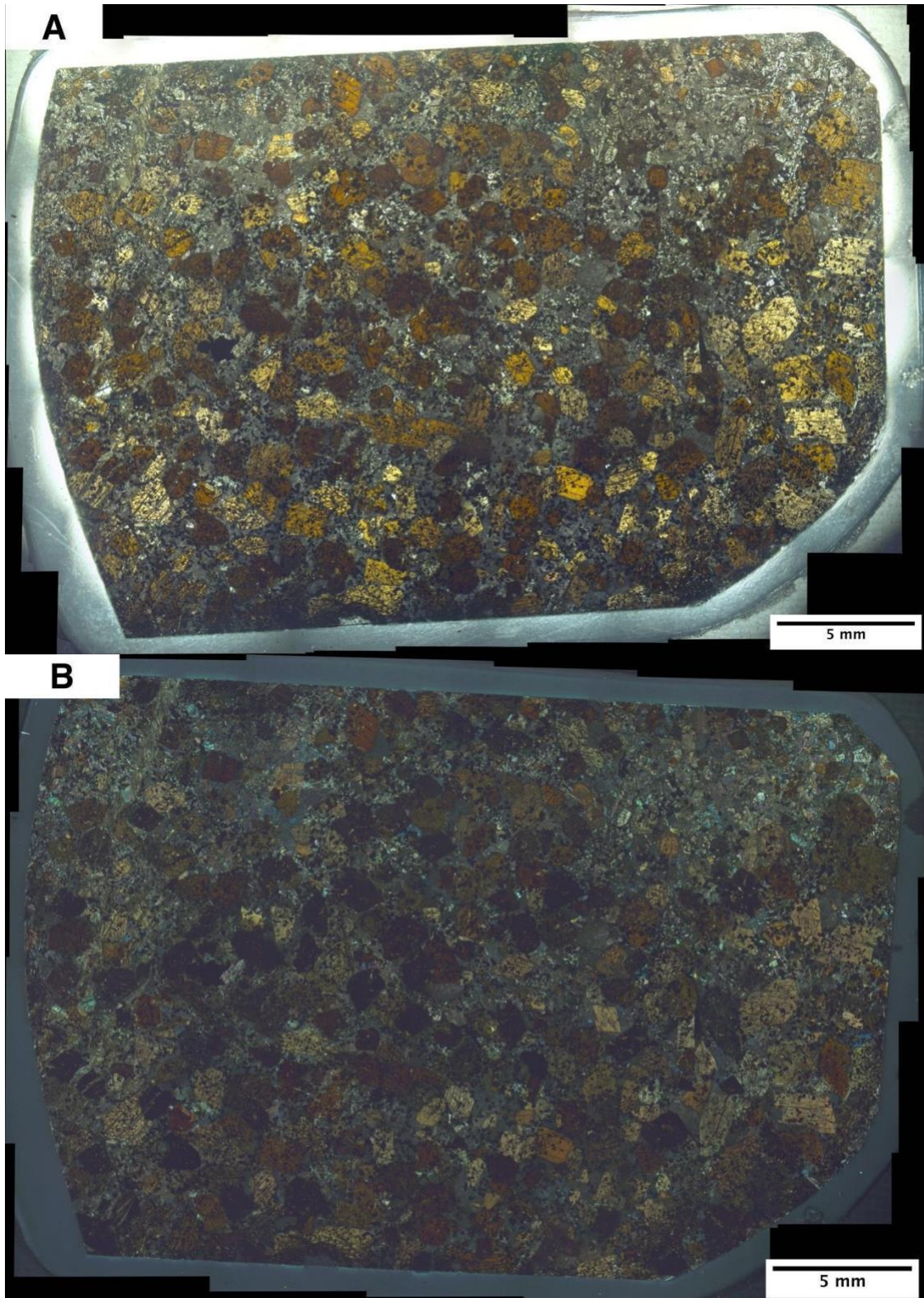
Figure S31: C2115 Amphibolite imaged in a) plane polarized light and b) cross polarized light
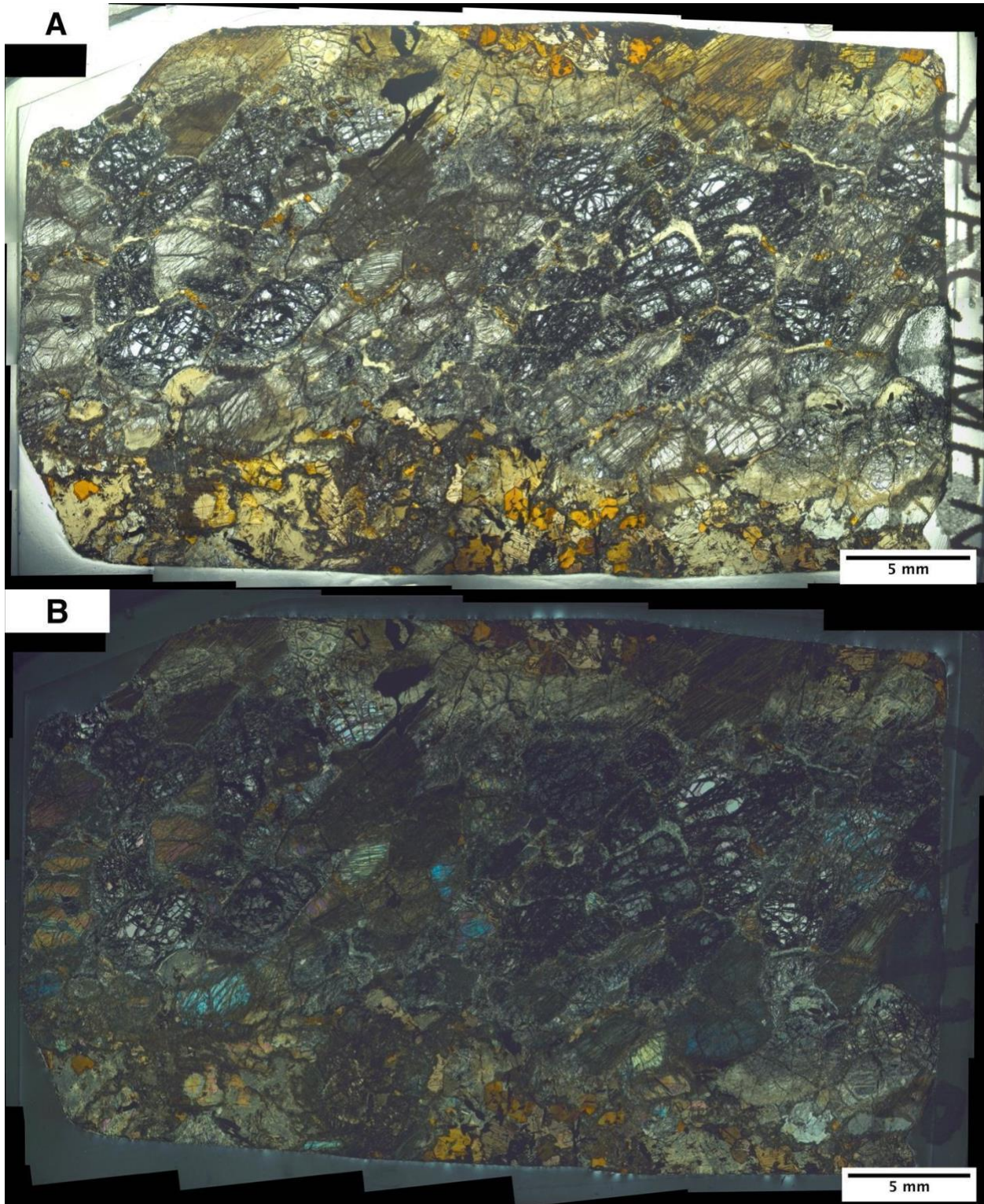
Figure S32: C2116 Harzburgite with phlogopite veins imaged in a) plane polarized light and b) cross polarized light

References

Allègre, C.J., and Luck, J.-M., 1980, Osmium isotopes as petrogenetic and geological tracers: Earth and Planetary Science Letters, v. 48, p. 148–154.

Bartlett, P.J., 1994, Geology of the Premier Diamond Pipe, *in* XVth CMMI Congress, Johannesburg, SAIMM

Birck, J.L., Barman, M.R., and Capmas, F., 1997, Re-Os isotopic measurements at the femtomole level in natural samples: Geostandards and Geoanalytical Research, v. 21, p. 19–27.

Boyd, F.R. and S.A. Mertzman, 1987, Composition and structure of the Kaapvaal lithosphere, southern Africa: Magmatic Processes: Physicochemical Principles: Geochemical Society Special Publication, v. 1, p. 13–24.

Carlson, R.W., Pearson, D.G.,Boyd, F.R.,Shirey, S.B., Irvine, G., Menzies, A.H., and Gurney, J.J., 1999, Re-Os Systematics of Lithospheric Peridotites: Implications for Lithosphere Formation and Preservation, *in* Proceedings of the 7th International Kimberlite Conference, Cape Town, Red Roof Design, p. 99–108.

Cawthorn, R.G., and Walraven, F., 1998, Emplacement and crystallization time for the bushveld complex: Journal of Petrology, v. 39, p. 1669–1687.

Cohen, A.S., and Waters, F.G., 1996, Separation of osmium from geological materials by solvent extraction for analysis by thermal ionisation mass spectrometry: Analytica Chimica Acta, v. 332, p. 269–275., v.3, p. 201–213.

Day, J.M.D., 2013, Hotspot volcanism and highly siderophile elements: Chemical Geology, v. 341, p. 50–74.

Day, J.M.D., and Brown, D.B., 2021, Ancient melt-depletion in fresh to strongly serpentinised Tonga Trench peridotites: Journal of Petrology, doi:10.1093/petrology/egab088.

Day, J.M.D., Harvey, R.P., and Hilton, D.R., 2019, Melt-modified lithosphere beneath Ross Island and its role in the tectono-magmatic evolution of the West Antarctic Rift System: Chemical geology, v. 518, p. 45–54.

Day, J.M.D., Walker, R.J., and Warren, J.M., 2017, 186Os-187Os and highly siderophile element abundance systematics of the mantle revealed by abyssal peridotites and Os-rich alloys: Geochimica et Cosmochimica Acta, v. 200, p. 232–254.

Day, J.M.D., Waters, C.L., Schaefer, B.F., Walker, R.J., and Turner, S., 2016, Use of hydrofluoric acid desilicification in the determination of highly siderophile element abundances and Re-Pt-Os isotope systematics in mafic-ultramafic rocks: Geostandards and Geoanalytical Research, v. 40, p. 49–65.

De Kock, M.O., Ernst, R., Soderlund, U., Jourdan, F., Hofmann, A., Le Gall, B., Bertrand, H., Chisonga, B.C., Beukes, N., Rajesh, H.M., Moseki, L.M., and Fuchs, R., 2014, Dykes of the 1.11 Ga Umkondo LIP, Southern Africa: Clues to a complex plumbing system: Precambrian Research, v. 249, p. 129–143.

Dongre, A., and Tappe, S., 2019, Kimberlite and carbonatite dykes within the Premier diatreme root (Cullinan Diamond Mine, South Africa): New insights to mineralogical-genetic classifications and magma CO2 degassing: Lithos, v. 338–339, p. 155–173.

Doyle, P.M., Bell, D.R., le Roex A.P. 2004, Fine-grained pyroxenites from the Gansfontein kimberlite, South Africa: Evidence for megacryst magma - mantle interaction: Suid-Afrikaanse tydskrif vir geologie [South African Journal of Geology], v. 107, p. 285–300.

Field, M., Stiefenhofer, J., Robey, J., and Kurszlaukis, S., 2008, Kimberlite-hosted diamond deposits of southern Africa: A review: Ore Geology Reviews, v. 34, p. 33–75.

Fouch, M.J., James, D.E., VanDecar, J.C., van der Lee S., 2004, Mantle seismic structure beneath the Kaapvaal and Zimbabwe Cratons: Suid-Afrikaanse tydskrif vir geologie [South African Journal of Geology], v. 107, p. 33–44.

Gaillou, E., Post, J.E., Rost, D., and Butler, J.E., 2012, Boron in natural type IIb blue diamonds: Chemical and spectroscopic measurements: The American Mineralogist, v. 97, p. 1–18.

Giuliani, A., and Pearson, D.G., 2019, Kimberlites: From deep earth to diamond mines: Elements (Quebec, Quebec), v. 15, p. 377–380.

Heaman, L.M., Phillips, D., and Pearson, G., 2019, Dating kimberlites: Methods and emplacement patterns through time: Elements (Quebec, Quebec), v. 15, p. 399–404.

Irvine, G.J., Pearson, D.G., and Carlson, R.W., 2001, Lithospheric mantle evolution of the Kaapvaal Craton: A Re-Os isotope study of peridotite xenoliths from Lesotho kimberlites: Geophysical Research Letters, v. 28, p. 2505–2508.

James, D.E., Fouch, M.J., Van Decar, J.C., van der Lee, S., and Kaapvaal Seismic Group, 2001, Tectospheric structure beneath southern Africa: Geophysical Research Letters, v. 28, p. 2485–2488.

Jelsma, H., Barnett, W., Richards, S., and Lister, G., 2009, Tectonic setting of kimberlites: Lithos, v. 112, p. 155–165.

Jones, A.P., Smith, J.V., and Dawson, J.B., 1982, Mantle metasomatism in 14 veined peridotites from Bultfontein mine, South Africa: The Journal of Geology, v. 90, p. 435–453.

Kjarsgaard, B.A., Januszczak, N., and Stiefenhofer, J., 2019, Diamond exploration and resource evaluation of kimberlites: Elements (Quebec, Quebec), v. 15, p. 411–416.

Korolev, N.M., Kopylova, M., Bussweiler, Y., Pearson, D.G., Gurney, J., and Davidson, J., 2018, The uniquely high-temperature character of Cullinan diamonds: A signature of the Bushveld mantle plume? Lithos, v. 304–307, p. 362–373.

Kramers, J.D., and Smith, C.B., 1983, A feasibility study of U−Pb and Pb−Pb dating of kimberlites using groundmass mineral fractions and whole-rock samples: Chemical Geology, v. 41, p. 23–38.

Liu, J., Pearson, D.G., Wang, L.H., Mather, K.A., Kjarsgaard, B.A., Schaeffer, A.J., Irvine, G.J., Kopylova, M.G., and Armstrong, J.P., 2021, Plume-driven recratonization of deep continental lithospheric mantle: Nature, v. 592, p. 732–736.

Luck, J.-M., and Allègre, C.J., 1984, 187Re-187Os investigation in sulfide from Cape Smith komatiite: Earth and Planetary Science Letters, v. 68, p. 205–20

Maier, W.D., Arndt, N.T., and Curl, E.A., 2000, Progressive crustal contamination of the Bushveld Complex: evidence from Nd isotopic analyses of the cumulate rocks: Contributions to Mineralogy and Petrology. Beitrage zur Mineralogie und Petrologie, v. 140, p. 316–327.

Maier, W.D., Peltonen, P., Juvonen, R., and Pienaar, C., 2005, Platinum-group elements in peridotite xenoliths and kimberlite from the Premier kimberlite pipe, South Africa: Suid-Afrikaanse tydskrif vir geologie [South African Journal of Geology], v. 108, p. 413–428.

McDonough, W.F., and Sun, S.-S., 1995, The composition of the earth: Chemical Geology, v. 120, p. 223–253.

Mitchell, R.H., 1986, Kimberlites: Mineralogy, geochemistry, and petrology: New York, NY, Kluwer Academic/Plenum.

Muller, M.R., Jones, A.G., Evans, R.L., Grutter, H.S., Hatton, C., Garcia, X., Hamilton, M.P., Miensopust, M.P., Cole, P., Ngwisanyi, T., Hutchins, D., Fourie, C.J., Jelsma, H.A., Evans, S.F., Aravanis, T., Pettit, W., Webb, S.J., Wasborg, J., and The SAMTEX Team, 2009, Lithospheric structure, evolution and diamond prospectivity of the Rehoboth Terrane and western Kaapvaal Craton, southern Africa: Constraints from broadband magnetotellurics: Lithos, v. 112, p. 93–105.

Pearson, D.G., Boyd, F.R., Haggerty, S.E., Pasteris, J.D., Field, S.W., Nixon, P.H., and Pokhilenko, N.P., 1994, The characterisation and origin of graphite in cratonic lithospheric mantle: a petrological carbon isotope and Raman spectroscopic study: Contributions to Mineralogy and Petrology. Beitrage zur Mineralogie und Petrologie, v. 115, p. 449–466

Pearson, D.G., Carlson, R.W., Shirey, S.B., Boyd, F.R., and Nixon, P.H., 1995, Stabilisation of Archaean lithospheric mantle: A Re-Os isotope study of peridotite xenoliths from the Kaapvaal craton: Earth and Planetary Science Letters, v. 134, p. 341–357.

Pearson, D.G., Irvine, G.J., Carlson, R.W., Kopylova, M.G., and Ionov, D.A., 2002, The development of lithospheric keels beneath the earliest continents: time constraints using PGE and Re-Os isotope systematics: Geological Society Special Publication, v. 199, p. 65–90.

Pearson, D.G., Irvine, G.J., Ionov, D.A., Boyd, F.R., and Dreibus, G.E., 2004, Re–Os isotope systematics and platinum group element fractionation during mantle melt extraction: a study of massif and xenolith peridotite suites: Chemical Geology, v. 208, p. 29–59.

Pearson, D.G., and Nowell, G.M., 2002, The continental lithospheric mantle: characteristics and significance as a mantle reservoir: Philosophical Transactions of the Royal Society. Series A, Mathematical, Physical, and Engineering Sciences, v. 360, p. 2383–2410.

Robinson, D.N., 1975, Magnetite-serpentine-calcite dykes at Premier Mine and aspects of their relationship to kimberlite and to carbonatite of alkalic carbonatite complexes: Physics and Chemistry of the Earth, v. 9, p. 61–70.

Rudnick, R.L., and Walker, R.J., 2009, Interpreting ages from Re–Os isotopes in peridotites: Lithos, v. 112, p. 1083–1095.

Scoates, J.S., and Friedman, R.M., 2008, Precise age of the plantiniferous Merensky Reef, Bushveld Complex, South Africa, by the U-Pb zircon chemical abrasion ID-TIMS technique: Economic Geology and the Bulletin of the Society of Economic Geologists, v. 103, p. 465–471.

Shirey, S.B., Harris, J.W., Richardson, S.H., Fouch, M.J., James, D.E., Cartigny, P., Deines, P., and Viljoen, F., 2002, Diamond genesis, seismic structure, and evolution of the Kaapvaal-Zimbabwe craton: Science (New York, N.Y.), v. 297, p. 1683–1686.

Smoliar, M.I., Walker, R.J., and Morgan, J.W., 1996, Re-Os ages of group IIA, IIIA, IVA, and IVB iron meteorites: Science (New York, N.Y.), v. 271, p. 1099–1102.

Sparks, R.S.J., Baker, L., Brown, R.J., Field, M., Schumacher, J., Stripp, G., and Walters, A., 2006, Dynamical constraints on kimberlite volcanism: Journal of Volcanology and Geothermal Research, v. 155, p. 18–48.

Sun, S.-S., and McDonough, W.F., 1989, Chemical and isotopic systematics of oceanic basalts: implications for mantle composition and processes: Geological Society Special Publication, v. 42, p. 313–345.

Tappe, S., Dongre, A., Liu, C.-Z., and Wu, F.-Y., 2018b, 'Premier' evidence for prolonged kimberlite pipe formation and its influence on diamond transport from deep Earth: Geology, v. 46, p. 843–846.

Tappe, S., Smart, K., Torsvik, T., Massuyeau, M., and de Wit, M., 2018, Geodynamics of kimberlites on a cooling Earth: Clues to plate tectonic evolution and deep volatile cycles: Earth and Planetary Science Letters, v. 484, p. 1–14.

Tappe, S., Stracke, A., van Acken, D., Strauss, H., and Luguet, A., 2020, Origins of kimberlites and carbonatites during continental collision – Insights beyond decoupled Nd-Hf isotopes: Earth-Science Reviews, v. 208, p. 103287.

Walker, R.J., Carlson, R.W., Shirey, S.B., and Boyd, 1989, Os, Sr, Nd, and Pb isotope systematics of southern African peridotite xenoliths: Implications for the chemical evolution of subcontinental mantle: Geochimica et Cosmochimica Acta, v. 53, p. 1583–1595.

Walter, M.J., 1999, Melting residues of fertile peridotite and the origin of cratonic lithosphere: Mantle Petrology: Field Observation and High Pressure Experimentation Spec Publ Geochem Soc, v. 6, p. 225–239.

Wu, F.-Y., Mitchell, R.H., Li, Q.-L., Sun, J., Liu, C.-Z., and Yang, Y.-H., 2013, In situ U-Pb age determination and Sr-Nd isotopic analysis of perovskite from the Premier (Cullinan) kimberlite, South Africa: Chemical Geology, v. 353, p. 83–95.